Aalto University
School of Engineering

Moffi Ebite Lady Henriette

Modelling of the Structural Performance of Arctic Offshore Wind Turbines

Master's Thesis
Espoo, November 24, 2016

Supervisor: Professor. Arttu Polojärvi
Advisor: Jaakko Heinonen

“The Offshore Wind Energy Act could be not only a jobs creator, but also a history maker.”

— Martin O'Malley

Aalto University
School of Engineering

Aalto University, P.O. BOX 11000, 00076 AALTO
www.aalto.fi

Abstract of master's thesis

Author: Moffi Ebite Lady Henriette

Title of thesis: Modelling of Structural Performance of Arctic Offshore Wind Turbines

Degree programme: Mechanical Engineering

Major: Mechanical Engineering **Code: IA3027**

Thesis supervisor Professor. Arttu Polojärvi

Thesis advisor(s): Jaakko Heinonen

Date November 24, 2016 **Number of pages:** 73 + 12 **Language** English

Offshore wind energy considered as the future of green energy, has known a consistent growth globally over the past decades with Europe being a major player followed by the US and Canada. The first large scale offshore wind farm of 160 MW (Horns Rev) was built at 14 m from the west coast of the Danish North sea site in 2002. This market of sustainable energy has also extended to other regions in the world most especially in Asia.[17]

There is a large potential market for offshore wind turbines in northern regions with extreme cold climate such as Northern Asia, North America and Northern Europe. According to the European Wind Energy Association (EWEA), approximately 20% of the European offshore wind turbines producing in total 10 GW will be installed in the Baltic Sea by 2020. Offshore wind turbines in Northern regions with extreme cold conditions will experience additional ice loads apart from aerodynamic and hydrodynamic loads.[30]

The main purpose of this research was to aid in the development of a tool, for structural design purposes of offshore wind turbines, that describes different environmental load conditions and site specific soil properties. This tool was to enable the user to easily select site specific environmental and soil properties, run a simulation and possibly generate an optimized wind turbine substructure. This thesis consisted of research on wind energy and finite element numerical simulations using the engineering software Abaqus.

This study focused on the modelling of the structural response of monopile offshore wind turbines under aerodynamic, hydrodynamic and ice loads taking into consideration the soil-structure interaction. A specific site at the Gulf of Bothnia (Tahkoluoto) made of glacial till seabed type was used as a case study. To arrive at a conclusion, the lateral response and Eigenfrequency of a 5 MW baseline offshore wind turbine under dynamic ice, wind and wave loads was evaluated considering the soil-monopile interaction idealized using the coupled spring foundation model. The results were validated using similar results from a previous simulation done by VTT.

The result of this experiment suggests that in the case of lack of in-situ site specific data, adequate selection and evaluation of the soil properties and soil models should be done as the soil-structure interaction can significantly affect the structural response.

Keywords Offshore wind turbine, wind load, ice load, wave load, foundation models, monopile, soil-structure interaction, finite element modelling.

Acknowledgment

Working on this thesis has offered me immense knowledge-wise and professional growth in the field of mechanical engineering. In addition, it has groomed me for my future career in engineering. The challenges and successes during this project have helped to activate my view towards the bigger picture of things.

I will like to extend my gratitude to my advisor Jaakko Heinonen who worked fervently and contributed immensely to the success of this project. Firstly, I will like to thank him for offering me the opportunity to be part of this challenging but growth activating project offered by VTT. In addition, I will like to thank him for mentoring me throughout the project and providing suggestions when the need arose. Furthermore, I will like to thank my supervisor Arttu Polojärvi who also guided me throughout the project.

The success of this thesis wouldn't have been possible without the Arctic team in VTT Technical Research Centre who were so welcoming and ready to help when needed. I will like to particularly thank Toni Hekkala for helping me with site specific data from the Gulf of Bothnia, Anna Maria Tikanmäki for helping me with Matlab and Juvankoski Markku for helping with soil mechanics.

Finally, I am immensely grateful to all my friends and family who indirectly or directly contributed to the success of this thesis and my education as a whole. My joy knows no bounds.

Espoo, November 24, 2016

Moffi Ebite Lady Henriette

Contents

1 Introduction

In the past decades, fossil fuels such as oil, coal and natural gas have been the main source of the world's energy. However, the use of fossil fuel as main source of energy has several limitations. Fossil fuels are not renewable at human time scale and release CO_2 gas which leads to the increase of the greenhouse effect. In addition, they are not spread evenly throughout the world which implies that countries with small or no fossil resource should minimize their dependency. Given the above mentioned limitations of fossil fuels, the search for alternative means of green energy led to the development of wind energy. [33]

In the last few years, wind energy also known as wind power has been the fastest growing form of sustainable energy given its environmental benefits. Wind energy is predicted, by the Intergovernmental Panel on Climate Change (IPCC), to play a major role in electricity generation by 2050. A total of about 2844 turbines in 74 wind farms were installed in 11 European countries by the end of the year 2014 producing a total power of 8GW. [3, 4]

There are severe limitations on the size of land-based or onshore wind turbines due to strict road transportation regulations. Given the considerable increase in wind energy demands and limited available onshore spaces, offshore wind farms seem to be a more attractive solution for renewable energy. [3, 4, 9] The northern European seas offer a huge market potential for offshore wind farms because of their good wind resource and seabed with relatively low water depth. Offshore wind turbines in extremely cold areas will experience aerodynamic and hydrodynamic loads such as wind, wave, current and ice loads which leads to a large extension on the number of load cases in the evaluation of offshore wind turbines. Given the challenging offshore environmental conditions especially in Artic region, numerical modeling of offshore wind turbines are currently being investigated. [17, 30]

This thesis introduces the technology and importance of offshore wind energy. In addition, it highlights the effect of load parameters (ice thickness, wind speed and wave height), soil conditions and foundation type on the structural response of offshore wind turbines. Furthermore in this thesis, numerical simulations are performed to explore the possibilities of idealizing soil-monopile interaction as coupled spring foundation model.

1.1 Background

The first practical wind energy machines were built in the form of windmills and made their first appearance as early as 200 BC (which is around the tenth century) in Persian Afghan. These windmills were based on rectangular sails rotating about vertical axes (vertical axle windmills). They were used to grind grain or draw up water, and were used in the grist-milling and sugarcane industries. By late twelfth-century, windmill technology had evolved and spread through the Middle East into Europe and the horizontal axle windmills were built in England, Netherlands and Germany. [5, 6]

Windmills were a major source of energy for performing various mechanical tasks in Europe before the industrial revolution. By supplementing the human and animal strength, windmills

played an important role in the economic, social and cultural landscape. They were used for example to reclaim large areas of land from the North Sea by Dutch and to drain land in East Anglia by English farmers. At the start of the twentieth century, about a quarter of a million wind turbines were already installed in Western Europe while tens of thousands were still in operation. In addition, European windmills had evolved and achieved a high level of technical specification, containing more sophisticated features such as: secondary rotors or fantails that turn automatically the cap into the wind; sails or blades with a degree of twist for improving efficiency; and speed governors in more advanced designs. Furthermore, over six million smaller windmills were developed in the USA (1850-1970) and used for pumping water, irrigating land and supplying water for steam engines on the American railroads. [5, 6]

By mid-twentieth century, traditional tower windmills had disappear due to the industrial revolution which brought about new technologies that could supply convenient and concentrated power needed at any time of the day and unaffected by the vagaries of the wind such as electric motors. However, the developments in electrical technology stared-up the need to develop new ways of producing electricity using wind. The first wind machine to generate electricity was built and installed in Cleveland, Ohio in 1888 by Charles Brush. This low speed and high solidity wind machine was the first wind machine that could be described as a wind turbine. It consisted of multi-bladed rotor (17m in diameter) that was kept facing the wind by a large tail vane and had a power capacity of 12KW. The followings years, many smaller wind turbines were used to charge batteries and provide modest amount for electricity for farmsteads and other remote locations. As the twentieth century progressed, further development of wind turbines was inspired by the design of airplane propellers and monoplane wings. In 1957, the Gedser 200KW wind turbine was built in Gedser, Denmark by Johannes Juul (Figure 1). It was considered to be one of the most influential machines in the history of modern wind power and was in use for eleven years given its inbuilt safety features. The Gedser wind turbine consisted of three blades; an automatic stall control to limit rotor power and speed in high winds; and an incorporated emergency aerodynamic tip brakes. [5, 6]

Figure 1: The 200KW Gedser wind turbine [1, 6]

After World War II, the idea of generating electricity from cheap fossil fuels became dominant. It was until after the emerging environmental movement in the mid-70s and the first oil crisis in 1973 that the search for renewable energy technologies began. After the "oil shock", the USA government invested in the wind energy research and development and financed many large turbine projects. In addition, a new legal frame work enabling turbine connection to electrical grid was introduced. This led to the development of the commercial wind turbine market from domestic and agricultural (1-25 KW) to utility interconnected wind farm applications (50-600 KW). Between the years 1981 to 1990, over 16,000 wind turbines with a combined power capacity of over a gigawatt were installed in California thanks to the financial support offered by the USA government. This was the first large-scale wind energy penetration outbreak. As at that time in Northern Europe, wind farm installation increased steadily and had a small but stable market. After 1990, the USA government withdrew its support due to unreliability of the machines which led to wind energy market activities been shifted to Europe. In Figure 2, the shift of the energy market from America to Europe after 1990 can clearly be seen. [5, 6, 11]

The first offshore wind turbine (named Wind World W2500/220) was installed close to Norgersund in southern Sweden in 1990. This turbine consisted of a steel tripod foundation and was installed approximately 300 m from the coast in a 7 m water depth. In 1991, the first offshore wind farm called Vindeby was built (in the Great Belt) at the west coast of the Danish North sea site. This wind farm consisted of eleven wind turbines of 450 KW capacity each installed in waters with depth of about 4 m and located 2 km from the shore. [33]

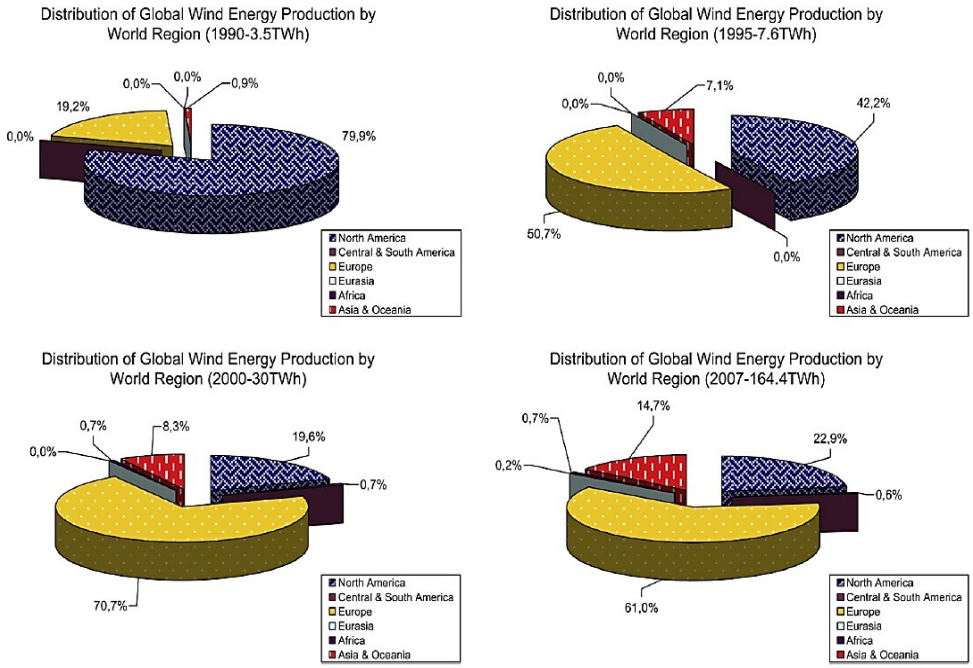

Figure 2: The gradual shift in energy generation between the world regions [5]

1.2 Objectives and Scope

In wind energy technology, offshore wind turbines offer more attractive solutions and greater advantages when compared to onshore wind turbines given their ability to produce higher

supply of electricity due to the presence of higher wind speed offshore. However, the installation, maintenance and repair costs of offshore wind turbines are relatively higher. In addition, modelling the structural performance of offshore wind turbines is quite complex given the complexity of the offshore environment especially in Artic offshore environments.

The main objective of this thesis was therefore to model the structural response of monopile offshore wind turbines under aerodynamic, hydrodynamic and ice loads taking into account the soil-monopile interaction. This thesis focused on the modelling of the lateral response of a 5-MW baseline monopile offshore wind turbine using finite element modelling. Another objective consisted of validating the results found by comparing the result of the lateral response of the baseline turbine modelled using Abaqus (in this thesis) against the result that was obtained for the same turbine using the FAST software in a previous simulation done by VTT. The soil-monopile interaction is studied in this thesis in order to understand the effect of foundation stiffness on the structural performance of offshore wind turbines. Furthermore, this work consisted of reviewing and selecting wind, wave and ice load models which were used in subsequent finite element modelling.

Considering the scope and time frame for completing this thesis work, this study was confined to using solely the selected soil model (coupled spring foundation model). In addition only wind, wave and ice loads were considered and used as input loads for the finite element modelling in this thesis. Some areas while relevant to this study such as other types of environmental loads e.g. current, tides, earthquake or seismic loads were not covered in this work. This thesis focuses solely on the modelling of the lateral response of horizontal axis offshore wind turbines.

1.3 Thesis Structure

The preliminary requirement for tackling the research objectives of this study consisted of understanding the basic principle behind offshore wind energy technology and the basics of soil mechanics. The work break down structure of this thesis consists of initially introducing offshore wind energy technology and discussing current trends in offshore wind energy projects in chapter 2. In addition, the foundations and environmental impact of offshore wind turbines are discussed chapter 2. In chapter 3, three foundation models are introduced. Furthermore, details on how to compute foundation stiffness theoretically using the coupled-spring foundation model are presented. Wave, wind and ice load models are reviewed in chapter 4. In chapter 5, the foundation stiffness for a specific area in Tahkoluoto (Gulf of Bothnia) is calculated theoretically according to the principles presented in chapter 3 and site specific data from Tahkoluoto. In addition wind, wave and ice loads are calculated using the models presented in chapter 4 and site specific data from Tahkoluoto used in the reference simulation. The loads calculated in chapter 5 are used in chapter 6 as input loads for dynamic analysis using finite element modelling. The foundation stiffness calculated in chapter 5 are used as boundary condition for the dynamic analysis in chapter 6. Furthermore, the result of the lateral response of a 5-MW baseline monopile offshore wind turbine (used as case study) under individual and combined wave, wind and ice load taking into account the soil-monopile interaction is discussed in chapter 6. Finally some conclusions are given in chapter 7.

2 Offshore Wind Technology

This chapter illustrates how electricity is produced using offshore wind turbines in section 2.1 and presents the factors that can greatly affect the power output in section 2.3. Foundation types used for offshore wind turbines are also presented in this chapter with emphasis made on monopile foundation which is used for subsequent analysis in this thesis. In addition, this chapter presents the environmental impacts of the installation and operation of offshore wind turbines. Furthermore trends in offshore wind projects are discussed.

2.1 Wind Energy Production

Wind power or wind energy technology refers to a process by which wind is converted into mechanical power or electricity. In wind turbine technology, the kinetic energy of the wind is converted into mechanical power which can be used for specific tasks or converted into electricity by a generator. Basically, the movement of wind causes the turbine blades to turn. The turbine blades are connected to a shaft which also rotates as the blades move due to the effect of the wind. In direct drive wind turbines, the shaft is directly connected to generator rotor that converts the rotary motion of the shaft into electrical power. In doubly-fed induction wind turbines (Figure 3), the shaft is connected to a gearbox which converts the low speed incoming rotation to high speed rotation suitable for generating electricity [1, 7]. The gearbox is in turn, connected to a generator that converts the amplified rotation energy into electrical energy. Wind farms produce bulk electrical power which is fed into a utility grid and distributed to customers. [2, 6]

The electricity produced by a wind turbine depends on the turbine size and wind speed through the rotor (blades' aerodynamics). It is measured in kilowatt-hours (kWh). Modern offshore wind turbines generally have power ratings ranging from 250 watts to 8 megawatts**.** However higher power rating offshore wind turbines are currently under investigation as mentioned in section 2.2. Taking into account the lower wind speeds and downtimes, the total annual production can be estimated to be 1/3 the rated turbine output which means for example that a 160 MW rated output offshore wind farm (consisting of 8760 turbines) will produce about 467 200 MWh / yearly. The offshore wind farm stated in the example above can supply electricity to about 150000 European average homes throughout the year given that an average European household uses about 4000 kWh yearly. [8, 10, 19, 34]

2.2 Offshore Wind Turbine Types and Sizes

Offshore wind turbines are generally horizontal axis wind turbines with a three-bladed rotor upwind of the tower which is supported by a housing called nacelle containing generally a gear box and an electrical generator as shown in Figure 3. This turbine configuration is the most common because it offers the best compromise between cost, technical performance and long-term reliability. [6, 8, 35]

The main subsystems of a turbine consist of blades or rotor, drive train, nacelle, tower and other equipment such as electrical cable, ground support equipment, controls and interconnection equipment. The yaw motor (Figure 3) keeps the rotor facing the wind while the brake

is used to stop the rotation during maintenance. The blades convert the wind energy into rotational shaft energy, the tower supports the rotor and the drive chain, the anemometer is used to measure the wind speed and direction. Generally, the towers are tubular and made of steel while the blades are made of fiberglass reinforced polyester or wood epoxy. [2, 6, 8]

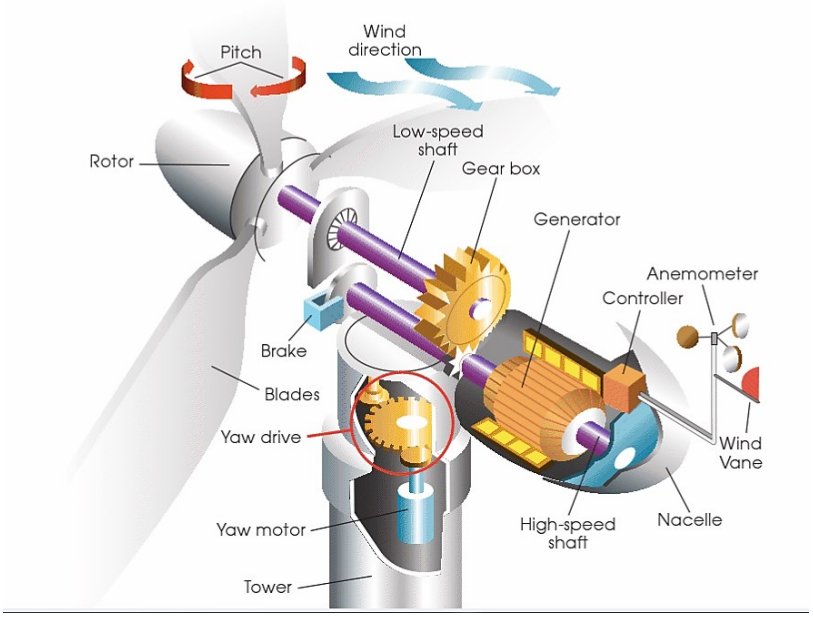

Figure 3: Main components of a typical modern high-power wind turbine [6]

Nowadays, more powerful large-scale turbines are developed in order to increase power output and decrease the cost of renewable energy production. Because the support structure of offshore wind turbines is costly, larger turbines are installed offshore in other to reduce production, maintenance and installation cost. Greater wind resource offshore implies that larger turbines offshore would produce higher output than they would onshore. Offshore wind turbine sizes are becoming larger and larger as shown in Figure 4. The average size of offshore wind turbines in 2014 was 4 MW which is significantly larger than the average onshore. In 2015, the average size of commercial offshore wind turbines was about 5 MW. 7 to 8 MW commercial wind turbines are already available. Larger turbines of 10 to 15 MW capacity are currently under investigation. [11, 34]

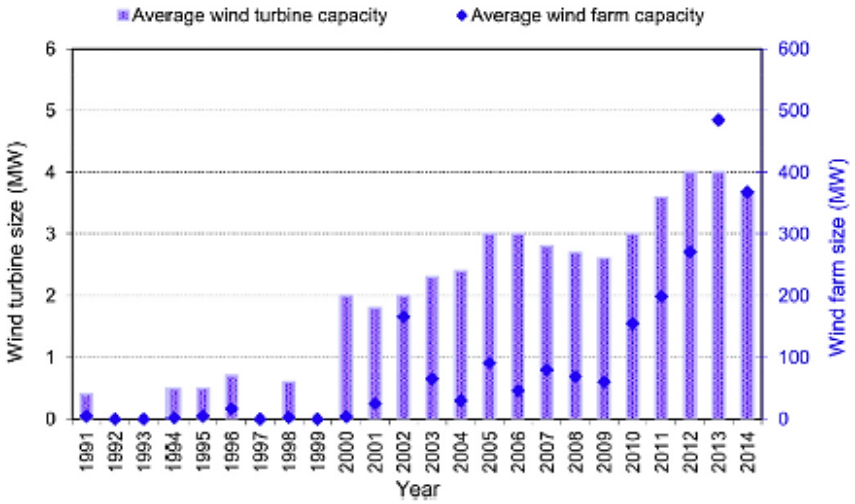

Figure 4: Average size evolution of existing offshore wind farms and wind turbines in Europe [8]

Figure 5 illustrates the power output of different sizes of horizontal axis turbines. As already explained above, the size of wind turbines affects its output. The green color in Figure 5 refers to onshore turbines which usually have the power ratings 2 and 3 MW while the blue color denotes the fact that turbines with power ratings as high as 5 MW or even higher may generally be installed offshore. [6]

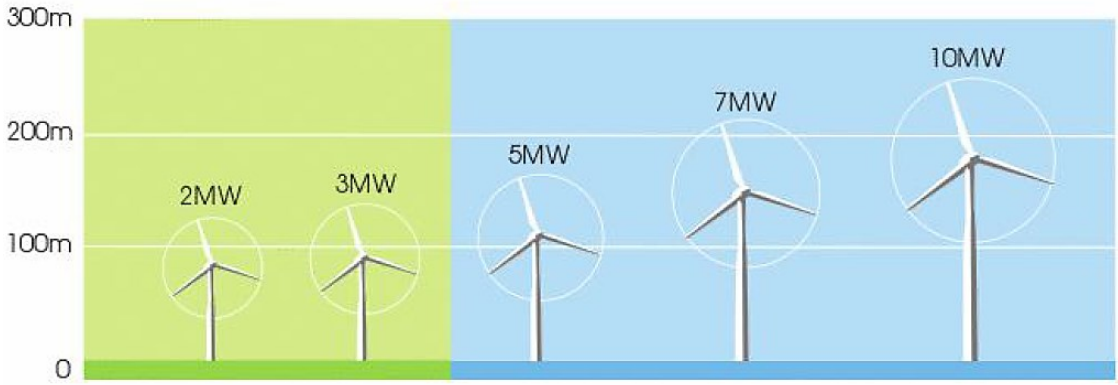

Figure 5: Typical power rating for large horizontal-axis wind turbines of various tower height [6]

2.3 Performance

The performance of a wind turbine can be affected by the site environmental conditions such as the average speed of the wind, the variability of wind and the occurrence of extreme events. Performance is evaluated by how much wind power the wind turbine is able to capture, how efficiently the turbine is able to convert the captured wind power into electricity and how well it is able to protect itself from violent weather. The actual power in the wind referred here as power intercepted is different from the power captured by the rotor due to certain limitations to the rotor efficiency. Large turbines are generally able to capture up to about 50% of the wind power. [6, 8]

The power intercepted described above can be computed using Equation (1) from fluid mechanics. Because wind power is proportional to the cube of its speed, a small difference in the wind speed can result in a large difference in available energy and electricity produced and therefore a large difference in the cost of the electricity produced. [6, 8]

$$P = 0.5\rho A U^3 \tag{1}$$

Where, P is the power intercepted; ρ is the density of the air; A is the area of the air of the intercepted airstream which is generally equal to the area swept by the rotor (area swept by the blades) and U is the speed of the wind.

Figure 6 illustrates the cubic relationship between the wind speed and power with the power given in kilowatts per square metre of intercepted area (kW/m^2) while wind speed is expressed in metre per second (m/s). The minimum speed at which a wind turbine begins to rotate and generate power is called the cut-in speed while the maximum speed (speed that

may lead to damage of the rotor) at which its breaking system is employed to bring the rotor to a standstill is referred to as cut-out speed. In other words, the cut-in and cut-out speeds represents the operating limits of the turbine. For large wind turbines the typical cut-in speed (minimum speed) range is between 4 to14 m/s while the typical cut-out speed (maximum speed) range is between 14 to 24 m/s as illustrated by the horizontal bar at the top of Figure 6. In addition, Figure 6 shows the speed at which the peak or rated power output is reached.[6]

Figure 6: Power in the wind in kW/m^2 as a function of wind speed in m/s; typical cut-in and cut-out speed range for wind turbines [6]

The power intercept can also be affected by the density of air. The density of air can cause a power difference of about 10% of different sites having the same wind speed or the same site between summer and winter due to the fact that the density of air varies with altitude and temperature. The density of cold air at sea level is considerably higher than warm air at a high altitude on land, thus it produces higher wind power. This basically means that an offshore wind turbine will produce more power than an onshore wind turbine under the same wind speed. In addition, the power produced by a wind turbine towards the end of winter for example is higher than that produced in mid-summer by the same turbine under the same wind speed. It should be noted however that winter in some continental areas may be much colder compared to some sea areas. [6, 8]

Figure 7 illustrates a typical power curve of a two megawatts wind turbine. It can be seen from the curve that the power generated between the cut-in and rated speeds follows an approximately cubic curve while that which is produced between the rated and the cut-out speeds stays constant and close to the rated value. This curve depends on the machine's efficiency at capturing wind at different speeds, the system's aerodynamics and electrical design to protect it from violent winds. [6]

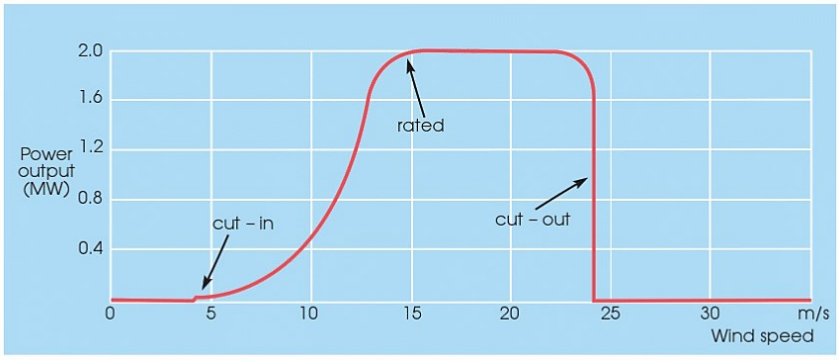

Figure 7: Typical power curve of a 2MW wind turbine; cut-in and cut-out speed [6]

2.4 Offshore Versus Onshore Wind Technology

Offshore wind turbines consist of wind turbines installed in a body of water to generate electricity. They are quite similar to onshore or land-based wind turbines and use substantially the same technology. In other words, the principle of producing electricity through wind explained in section 2.1 is the same for both offshore and onshore wind turbines. As far as energy capture is concerned, the size of offshore wind turbines represents the only significant difference between offshore and onshore wind turbines. Offshore wind turbines are generally larger than those onshore. However, offshore wind turbine foundations are considerably different from those used onshore. The drive trains for offshore and onshore wind turbines are identical. Some offshore wind turbines use direct drive while others use gearboxes and relatively high speed generators. In addition, offshore and onshore wind turbines towers have similar construction. Furthermore onshore and offshore wind turbines are generally three-bladed horizontal axis wind turbines. [34, 35]

Even though the tower, turbine and blades of offshore wind turbines are generally similar to those onshore, the engineering and design of offshore wind turbines depends on site specific conditions such as water depth, geology of seabed, wave and ice loading. Offshore wind turbines have technical modifications and substantial system upgrades for adaptation to the marine environment. For example, offshore wind turbine towers are built stronger to cope with wave loads and ice flows, nacelles are pressurized in order to keep corrosive sea spray from critical electrical components, brightly-colored access platforms are added for navigation safety and maintenance access. In addition, in order to minimize the cost of every day servicing, offshore wind turbines may have automatic greasing systems to lubricate bearings and blades as well as cooling systems to maintain gear oil temperature within a specified range. [35]

Offshore wind turbines are steadier when compared to onshore wind turbines due to the presence of denser and higher wind speed offshore. One of the reasons why the wind regime is better offshore is because there are no hills or mountains to interrupt its flow. Furthermore, due to limited available space onshore, offshore wind turbines offer a better solution. Larger and larger wind turbines can be installed offshore which implies higher power output. It is also much easier to obtain planning permission for an offshore wind farm compared to onshore given the strict road transportation regulations. However, the construction and maintenance cost of offshore wind turbines is considerably higher than that of onshore wind turbines. The maintenance of offshore wind turbines is performed using special vessels or helicopters. Offshore wind turbines are greatly influence by their surrounding environment. The construction of offshore wind turbines require higher accuracy and use of materials that resist the corrosive marine environment. [8, 9, 34]

2.5 Environmental Impact

Using wind energy for electrical or mechanical power production is far much safer than using fossil fuels or nuclear power. Contrary to these two, wind turbines do not pollute the atmosphere with greenhouse emission neither do they cause any problems for future generations with radioactive waste. However, it still poses a potential long term effect on the human life though minor but not negligible. Since wind energy is gradually becoming one of

the main energy sources, its environment impact that seems minor now might have disastrous effects in the near future thus, it is important to evaluate its environmental impacts. [11]

The environmental impacts of offshore wind turbines are quite similar to those onshore but also have significant differences that need to be accounted for. Wind turbines emit noise, shadow effect and have a visual significance that can be quite annoying to people when installed onshore. In addition, they might interfere with radio and television signals. Mechanical and aerodynamic noise are the two main kind of noise produced by a wind turbine. These noise can give a hard time to people living close to wind farms. Several research and surveys have been carried out in order to ascertain the effect of the noise produced by wind turbines on the well-being of people living close to wind farms. According to these research, those annoyed by the presence of wind turbines usually experience stress symptoms such as headache. In addition, it was realized that the low-frequency aerodynamic noise of wind turbines can cause sleep disturbance, hearing lost and affect the vestibular system of those living close to wind farms. Onshore wind turbines have an impact on animals such as birds as they pose as obstacle and might lead to the death of many local birds. [11, 12]

Another important aspect of the impact of wind turbines on its surroundings is the issue of safety hazards. Damaged rotor blades breaking off due to severe environmental conditions might pose a threat to the surroundings. This depends on how far the damaged rotor blades can fly which is usually not easy to predict. Another safety hazard consists of the problem of ice accretion at the rotor blade whereby significantly large chunk of ice are flung off over considerable distance. [12]

Even though offshore wind turbines installed far away from the shore may provide less visual impact and may solve the problem of the emitted noise affecting the human life, the noise, toxic effects from spills and electromagnetic fields from cables during the construction and operation of offshore wind turbines may affect the marine species negatively (Figure 8). Offshore wind turbines might pose a threat to sensitive marine species such as dab and salmon that can perceive pile-driving pulses at a considerable distance during the construction and operation of wind turbines offshore. Marine mammals depends on their hearing system for communication, orientation and finding their way. Therefore, the response of Marine mammals to noise may lead to behavioral change, temporal reduction of habitat size and displacement due to construction and maintenance activities of offshore wind turbines. [8, 11, 12]

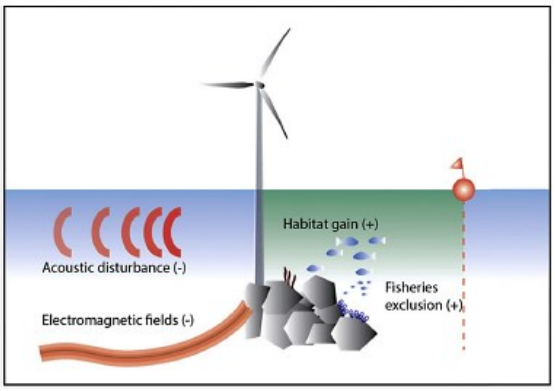

Figure 8: Offshore wind installation effect on the marine environment [8]

2.6 Trends in Offshore Wind Projects

The modern offshore wind movement can be traced to early 1990s as illustrated in section 1.1. By late 1980s to early 1990s, a number of small European pilot projects had begun however, the development was slow. By the year 2000 there were only about 45MW of offshore generating capacity globally and all in European waters. The first large scale offshore wind farm of total capacity 160 MW (Horns Rev) was built at 14 m from the west coast of the Danish North sea site in 2002. This wind farm consisted of 80 turbines with a capacity of 2 MW each. The installed capacity has accelerated since the year 2000 with a cumulative capacity of about 3087 MW by the year 2010 and 8759 MW of wind generating capacity at offshore sites by the year 2014. This represented about 2% of the total global installed capacity which is projected to increase to 10% by the end of the twenty-first century by the Global Wind Energy Council. [17, 34]

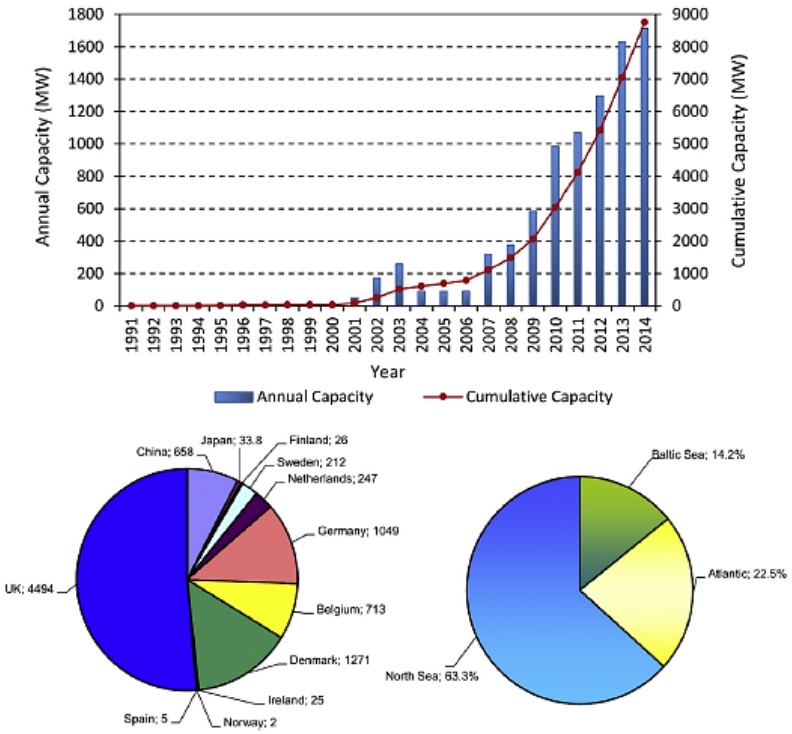

Figure 9: Worldwide offshore capacity evolution and cumulative share by country in MW and European cumulative share by sea basin in 2014 [8]

Europe is leading globally in the offshore wind power market with installed capacity of about 8.1 GW which correspond to approximately 29.6TWh annual electricity in a normal wind speed year. There are fourteen countries with offshore wind power capacity. Most of the offshore capacity is located in the North Sea, Irish Sea, the Baltic Sea and the English Channel. By the end of the year 2014 as illustrated in Figure 9, the United Kingdom was leading globally in offshore wind capacity with total capacity of about 4.49 GW followed by Denmark (1.27 GW), Germany (1.05 GW) and Belgium (0.71 GW). In other parts of the world, the development of offshore wind capacity has been slow primarily due to the cost of building offshore. Despite having considerable offshore potential along its Eastern and Western Seaboards, the United States have been notably reluctant to build. There was just a single 20 kW offshore wind turbine in waters off Maine at the end of 2014. [8, 34] Figure 10 shows a map of the operating and planned offshore wind farms in Europe in the year 2005 while Figure 11 illustrates a map of the operational wind farms in North West Europe. The world's

first offshore wind farm designed for demanding ice conditions in (Tahkoluoto) Pori in Finland is currently under construction by Suomen Hyötytuuli Oy. This wind farm is estimated to produce energy by autumn 2017. [50]

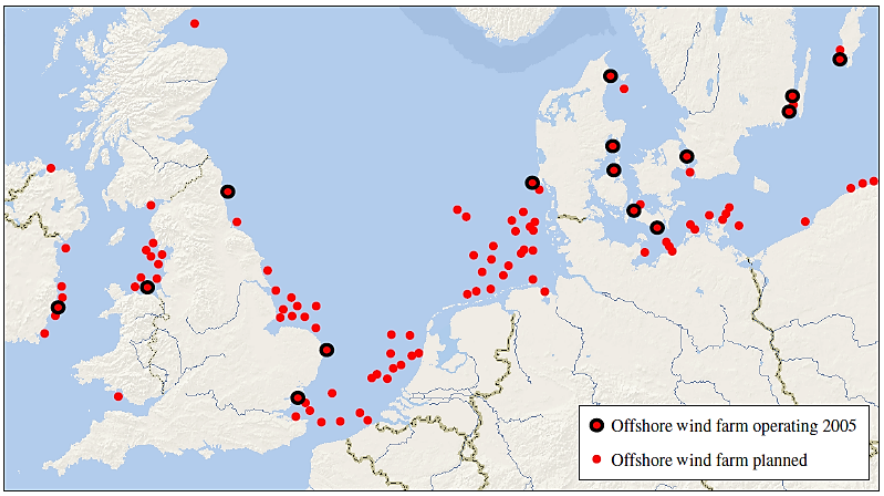

Figure 10: Overview of existing and planned offshore wind farms in Europe [19]

Figure 11: Operational offshore wind farms in North West Europe [46]

Offshore wind energy is expected to drastically increase by 2020 given that 38 GW of additional capacity is expected to be installed by then. This implies that the cumulative installations will increase to approximately 47 GW from which about 4.4 GW are already under construction and about 34 GW have been contracted or approved. Offshore wind technology are expected to evolve rapidly in other to be able to support offshore wind projects located farther from the shore and in deeper waters where some of the environmental impacts are reduced. In other words, offshore wind turbine substructure technologies must be developed to support deeper waters and larger turbines. The design and material innovations of the substructures of offshore wind turbines aim at adopting new geometries that minimise material intensity and simplify manufacturing and installations operations. A success of these innovations will decrease the impacts of future offshore wind projects on the marine life, the seabed and the zoobenthos due to the reduced construction period and the footprint of the installations. [8]

2.7 Foundations for Offshore Wind Turbines

The foundation for offshore wind turbines is relatively high cost and accounts for up to about 35% of the installed cost [16]. The type of foundation used, as illustrated in Figure 12, depends on the offshore location, the water depth and the seabed geology. Foundation can be classified as fixed-base or floating substructure. The most common offshore turbine foundations are monopiles and gravity-based foundations installed at shallow water depth (below 50m in water depth). By the end of 2014 as shown in Figure 13, 2920 substructures have been installed in Europe with monopile foundations comprising of 78.8% of all installed foundations. 10.4% of the installed foundations are gravity based foundation, 4.7% for jacket foundations, 4.1% for tripods, 1.9% for tripiles and 0.1% for floating substructures. [8, 34]

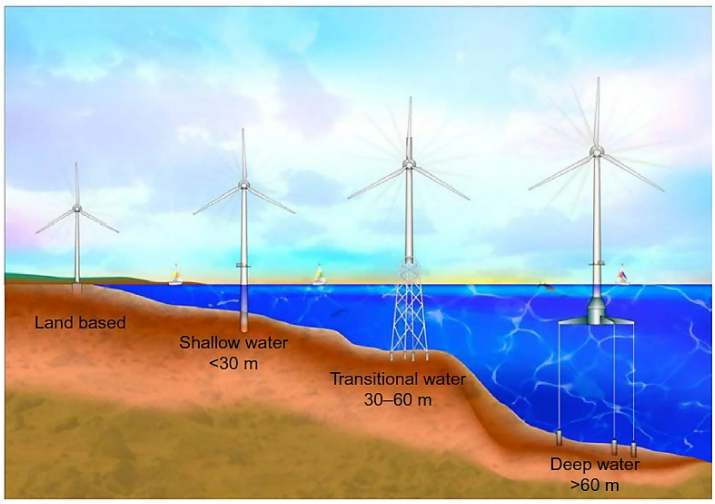

Figure 12: Foundations for offshore wind turbines depending on the water depth [34]

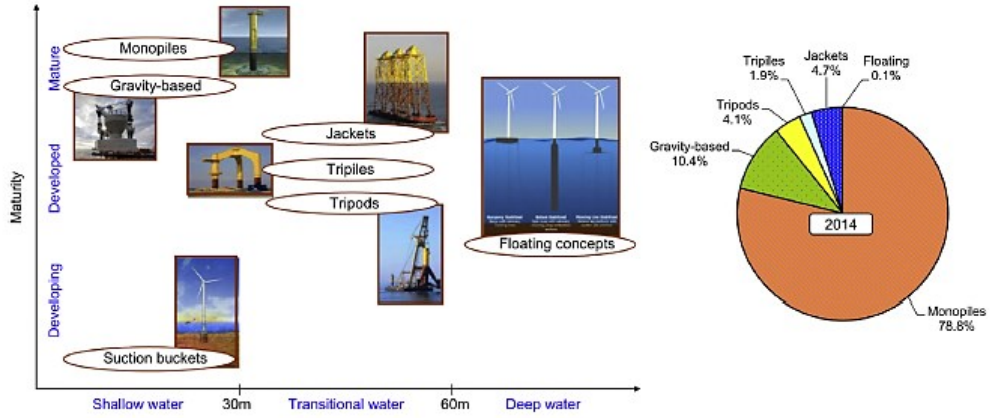

Figure 13: Support structures for offshore wind farms and their share in European installation [8]

2.7.1 Fixed Offshore Wind Turbine Foundations

There are five main types of fixed substructures used in shallow water below 50m water depth as shown in Figure 14. These main types of fixed substructures shown in Figure 14 are monopile (a), gravity-based (b), jacket (c), tripod (d) and tripile (e). [10]

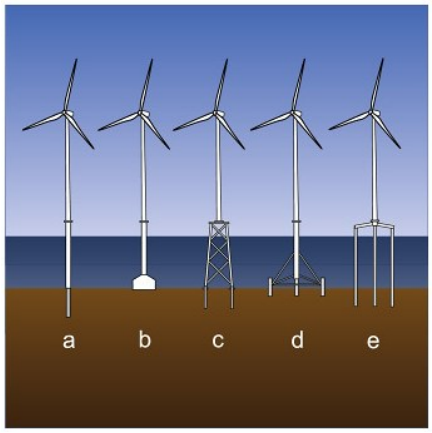

Figure 14: Fixed substructures for offshore wind turbines: Monopile (a), gravity-based (b), jacket (c), tripod (d) and tripile (e) [10]

Monopile refers to a single pile (Figure 15) driven into the seabed on to which the turbine tower is bolted through a transitional piece. In other words, there is a transitional piece between the monopile and the tower. Monopile foundations are used for water depth below 30 m. The depth of the pile below the seabed depends on the geology of the area. Basically, the pile must reach through any silt on the seabed to a stable stratum below. Special vessels are used for creating the pile foundation. The length of the monopile above the seabed is generally 30-50 m. Monopile foundations are limited to shallow water because longer monopile length will increase the total length of the single support which may aggravate the problem of tower resonant frequencies. Furthermore, it may be very difficult and costly in materials to build adequate stiffness into a monopile/tower combination in deep waters. In addition, long monopoles are difficult to handle during transportation and installation. Figure 15 illustrates a monopile foundation in details. Monopiles are the most commonly used offshore wind turbine foundation type because of their simple design which makes it quite easy to standardize the manufacturing process of monopile foundations. In addition, the installation of monopile foundations is quite easy and cheaper than other foundation types used for offshore wind turbines. Monopile foundation was considered in this thesis for subsequent analysis given its advantages in shallow waters as explained above. Pile foundations generally consist of steel cylindrical pipe and are designed to be able to carry static, cyclic and transient loads without deforming or vibrating excessively. [10, 24, 34, 39]

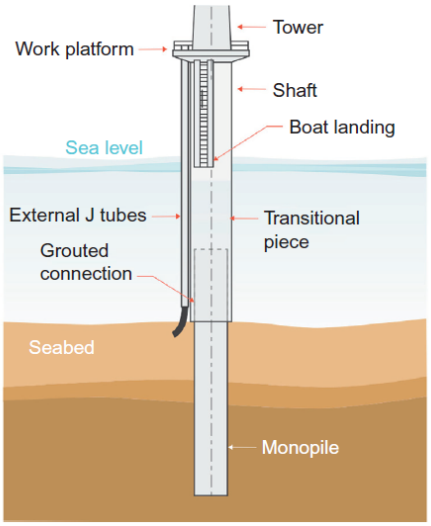

Figure 15: A monopile foundation for an offshore wind turbine [34]

Gravity-based foundations (Figure 14b) are generally fabricated in reinforced concrete with ballast (or steel) and it uses its own weight to anchor to the seabed at water depth between 0-25 m. The gravity foundation must be massive enough to withstand the bending and translation loads transferred to it by the tower. The seabed must be dredged and leveled. A large base area with scour is generally used to counteract the moment produced by the system. [10, 34] Jacket foundations (Figure 14c) consist of a three or four-legged lattice structure made of tubular steel and are generally used in water depths of about 20-50m. They experience low wave forces. Jacket foundations are similar to those used in offshore oil and gas industries. [10] Tripod foundations (Figure 14d) are relatively lightweight three-legged steel structures in which the frame is submerged in the water. They are used for water depth between 20m and 50m. This type of support structure provides good stability and stiffness to the entire system. [10] Tripile foundations are suitable for water depth between 30 to 50m. Tripile consists (Figure 14e) of a three-legged steel support frame that extend from the foundation to above the water level before being connected to the tower. [10]

2.7.2 Floating Wind Offshore Turbine Foundations

Floating offshore support structures are used for water depth above 50m. The cost of fixed foundations becomes quite expensive for water depth above the water depth 50m thus the need for floating foundations. Floating support structures are still currently under research and development stage. Figure 16 shows floating structures that have been used in prototype and full scale testing. [10]

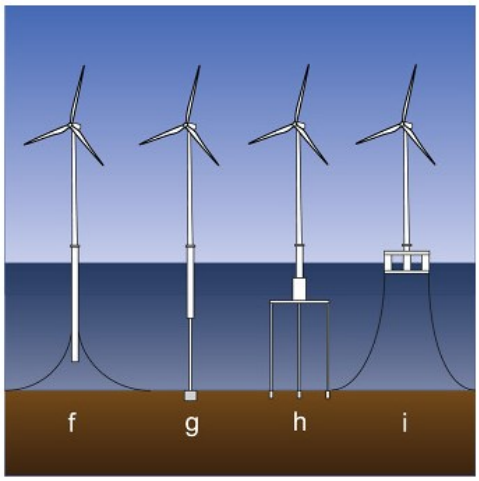

Figure 16: floating substructures for offshore wind turbines: Spar (f), tension-legged platform (g and h) and semi-submersible (i) [10]

Figure 16f is called the spar type consisting of a long closed cylinder which is made compliant by catenary mooring lines and anchor. The cylinder floats upright while the system is stabilized by ballast at the base due to the buoyancy force. [10] Figure 16g and h are called the tension-legged platform. It is partially submerged underneath the sea surface and fixed to slim tension rod(s) or line(s) that are anchored to the seabed. This structure must have enough buoyancy to support the turbine and maintain tension in the legs under all sea and wind condition. [10] Figure 16i is the semi-submersible substructure which consists of a column-stabilized units that provide buoyancy and stability which are normally designed in a triangular or rectangular formation and kept in place with catenary mooring lines. [10]

3 Soil-Structure Interaction

The soil-structure interaction must be taking into account when evaluating the structural response of offshore wind turbines. To better understand the soil-structure interaction, it is important to understand foundation modelling, basic soil and foundation principles. In this chapter, a general information on foundation and soil classification is provided. The foundation types used for offshore wind turbines have already been provided in chapter 2. In addition, a review on three different foundation models that can be used to model the soil-monopile interaction is provided. The coupled spring model was used for subsequent analysis in this thesis. The principles provided in section 3.4 must be followed thoroughly in other to use the formulations provided in Table 5 to theoretically compute foundation stiffness of the coupled spring model. The formulations in Table 5 were used in chapter 5 to compute theoretically the foundation stiffness of the specific area in Tahkoluoto considered in this thesis as case study.

3.1 Foundation Basics

Foundation in civil engineering generally refers to the connection between the structure and the ground that supports it (the structural element that connect the structure to the soil). Structures must have the right kind of foundation based on the kind of soil condition, the structure and the loads in other to withstand failure. The limitation in the knowledge on actual site service load, soil conditions and soil-structure interaction introduce uncertainty into foundation design problems. Factors of safety are used in foundation designs to compensate for these uncertainties. There are building codes which are the minimum design requirement used for foundation design and construction (Eurocode 7 (BS EN 1997-1) for geotechnical design, the international building code (IBC) in the United States). [14, 15]

Foundations or the structural element that connect the structure to the ground can be made of wood, steel and concrete. Foundations can be categorized into two types: shallow foundations and deep foundations. In shallow foundation, the load is transmitted to the near-surface soils while in deep foundation like it name indicates some or all of the loads are transmitted to deeper soil. For the design and construction of foundation, drill rigs are used for soil exploration to know the conditions beneath a construction site and to obtain soil samples which are taken to the laboratory for evaluation and testing. Drill rigs are also used for creating the space where the foundation element will be embedded for example when drilled shaft are used as deep foundation, a drill rig is used to create a cylindrical hole to the ground where a reinforcing steel cage will be inserted while the hole will be filled with concrete. In foundation design the performance, strength and serviceability requirements must be met. [14]

3.2 Soil Basics

Earth or ground material can be divided into two main groups which are rocks and soil. Soil material is the most common used earth material. Soil material is not a continuous solid material like engineering materials. It is an assemblage of many individual particles. In addition, it can contain simultaneously particles in solid, liquid and gaseous state. The strength

and compressibility of a soil material is not a function of the internal properties of its individual particles. These engineering properties depend on the arrangement and the interaction between these particles. The solid particles can include one or more of the following materials: rock fragments (granite, limestone and basalt); rock minerals (quartz, feldspar, mica and gypsum); Clay materials (kaolinite, smectite and illite); Organic matters (decomposed plants); Cement agent (calcium carbonate); miscellaneous materials (man-made debris). The liquid element is usually water while the gaseous element is generally air. These two fill the void between the solid particles and can also contain other materials other than water and air. [14]

Soil can be divided into five general types: clay, gravel, sand, silt and organic. Different standardized systems of soil-classification have been developed for foundation engineering problems (ISO 19901-4, USCS). These general soil types can be further classified into subclasses. For example, sand can be further classified into the following main types: loose sand, medium sand, dense sand and very dense sand. Clay can be classified into soft, stiff and hard clay. The soil in-depth composition can vary significantly. An example of three offshore locations and the different in-depth composition of the soil of these locations is shown in Figure 17. Soil properties (density of submerge soil, soil undrained shear strength S_u, soil undrained strain ε, soil angle of friction $\acute{\emptyset}$, the initial modulus of horizontal subgrade reaction k_h) required for foundation design are usually obtained through in-situ sampling and analysis from drilled samples in the laboratory. Table 1 provides an overview of typical values of the undrained soil density and strain for clay, at 50% the maximum stress. [14, 19]

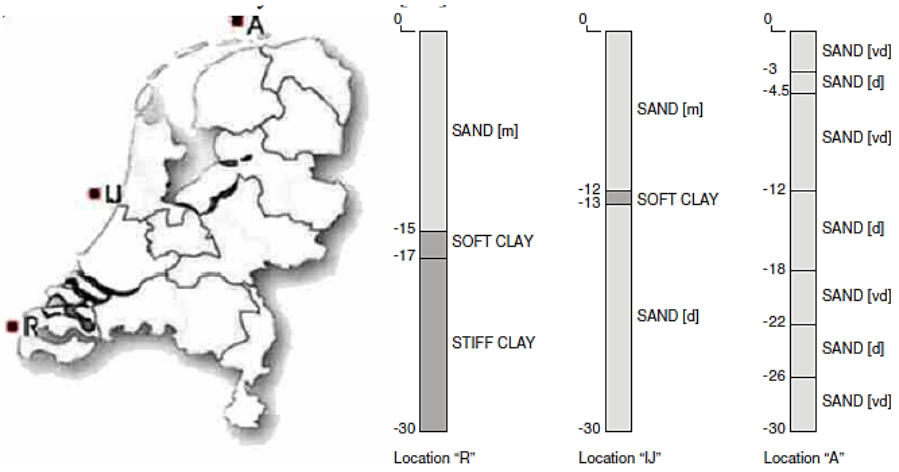

Figure 17: Soil layers for three offshore sites with medium [m], dense [d]and very dense [vd] sand layers; and soft and stiff clay layers [19]

Table 1: Characteristic parameters of clay; Soil undrained shear strength (S_u); Soil secant young's modulus (ε_{50}) [19]

Clay type	s_u [kPa]	ε_{50} [%]
soft	0-25	1.5
firm	25-50	1.5
stiff	50-100	1.0
very stiff	100-200	0.5
hard	> 200	0.5

3.3 Foundation Modelling

The load from the structure is transferred to the surrounding soil by its foundation. It is important that the foundation can sustain and transfer all the loads that may be applied, especially during extreme environmental conditions. The connection to the ground can significantly affect the dynamics of the structure. [16] Three different models used for modelling the effect of the soil-pile interaction are presented in this section. These models includes the so called p-y curve method, effective fixity length and the coupled spring models. [17]

3.3.1 Coupled Spring Model

In the coupled spring model (Figure 18), the spring properties are derived by applying two load sets that are typical for operational conditions of offshore wind turbines to the nonlinear model and using the outcome to derive the spring constants in Equation (2). For laterally loaded offshore turbines, the relationship between the loads and the soil-pile connection stiffness matrix can be approximated by Equation (2). According to Jan Vander Temple (2006) [19], the nonlinear p-y curves model and the coupled spring model have been proven to be the most suitable for offshore wind turbine design. [19] The coupled spring model was chosen for subsequent analysis in this project because it was easier to compute the soil stiffness theoretically, in the absence of site specific measurement, following the guide provided in section 3.4.

$$\begin{bmatrix} F \\ M \end{bmatrix} = \begin{bmatrix} K_{xx} & K_{\varphi x} \\ K_{x\varphi} & K_{\varphi\varphi} \end{bmatrix} \begin{bmatrix} x \\ \varphi \end{bmatrix} \tag{2}$$

Where, F is the lateral force and M the over-turning moment; x is the lateral displacement and φ is the rotation of the tower as illustrated in figure 22; K_{xx}, $K_{\varphi\varphi}$, $K_{\varphi x}$ and $K_{x\varphi}$ are the foundation stiffness in the lateral and rotational directions (K_{xx} in GN/m, $K_{\varphi\varphi}$ in GN.m/rad, $K_{\varphi x}$ and $K_{x\varphi}$ in GN).

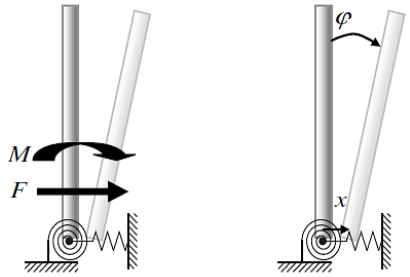

Figure 18: Coupled lateral and rotational springs for foundation representation with loads *F* and *M*; and reaction *x* and *φ* [19]

3.3.2 P-Y Curve Method

In the p-y curve method, the soil is modelled as a set of nonlinear springs as illustrated in Figure 19. In this method, the soil-pile interaction is described by three types of nonlinear resistance-displacement curves known as the p-y, t-z and Q-z curves based on Winkler's hypothesis (Figure 21). Basically, the pile is modelled as a beam on a series of uncoupled nonlinear springs representing the interaction between soil and pile. The p-y curve describes

the relationship between the lateral soil pressure (p) and the corresponding pile displacement (y). The t-z curve describes the relationship between skin friction (t) and the relative vertical displacement (z) between the pile and the soil. The Q-z curve describes the relationship between the bearing stress at the pile tip (Q) and the pile tip settlement (z). The p-y, t-z and Q-z curves are developed from soil-structure interaction response from static loading condition. The p-y curves are suitable for foundations of offshore structures with smaller diameter. [19, 21, 47, 48]

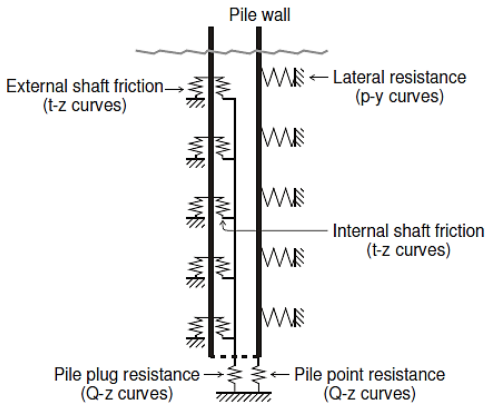

Figure 19: Distributed spring model of pile-soil interaction [19]

Figure 20 illustrates an example of p-y curves for laterally loaded pile installed in soft clay. The soil reacts linearly and elastically in the first part of the curve. This means that the soil will return to its original state when the load is released. The deformations will become permanent and the soil will begin to loose resistance if the load exceeds the breaking point in the curve. [19]

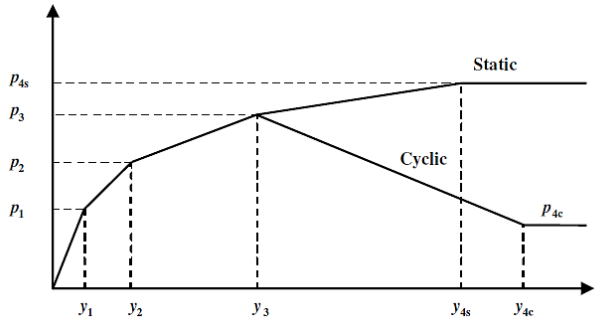

Figure 20: Typical shape of horizontal load *p* and displacement *y* in a p-y curve for soft clay under static and cyclic loading according to Matlock [19]

Figure 21 illustrates a physical representation of the Winkler foundation. According to Winkler's hypothesis, the soil medium is represented by a number identical but mutually independent, closely spaced, discrete, linearly elastic springs. The deformation of the foundation due to applied load is considered to be confined to the loaded region only. [47, 51]

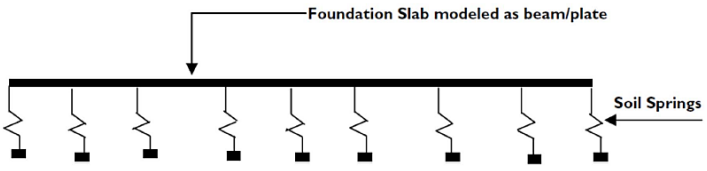

Figure 21: Winkler foundation [51]

3.3.3 Effective Fixity Length

The stiffness at mudline for the effective fixity length is given in accordance with Equation (3) and (4). [17]

$$F = KU \tag{3}$$

$$\begin{bmatrix} F_x \\ M \\ F_z \end{bmatrix} = \begin{bmatrix} K_{xx} & K_{\varphi x} & 0 \\ K_{x\varphi} & K_{\varphi\varphi} & 0 \\ 0 & 0 & K_z \end{bmatrix} \begin{bmatrix} x \\ \varphi \\ z \end{bmatrix} \tag{4}$$

Where F_x is the lateral force, F_z is the vertical force, z is the vertical displacement, K_z is the vertical soil stiffness, M the over-turning moment, x is the lateral displacement and φ is the rotation of the tower at mudline.

In the effective fixity length model, the clamping effect of the soil is replaced by a rigid clamping of the foundation at an effective depth below the sea bed. In other words, the foundation (pile) is considered a cantilever completely fixed at a particular depth below the sea bed as illustrated in Figure 22. Depending on the soil condition, the effective fixity length can vary between 3.5 to 8 times the pile diameter according to Barltrop or can vary between 3.3 and 3.7 the pile diameter according to Kuhn. For a pile with an effective fixity length l, the soil stiffness matrix K at the mudline described in Equation (4) can be theoretically estimated using Equation (5). [17]

$$K = \frac{2E_pI_p}{l^3} \begin{bmatrix} 6 & -3l & 0 \\ -3l & 2l^2 & 0 \\ 0 & 0 & \frac{A_pl^2}{2I_p} \end{bmatrix} \tag{5}$$

Where, l is the effective fixity length (m), E_p is the elastic modulus of the pile, I_p is the second moment of area of the pile and A_p is the pile cross-section area.

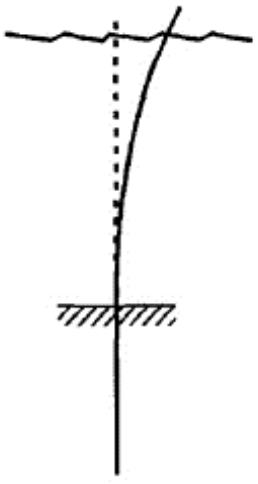

Figure 22: Effective fixity length [17]

3.4 Theoretical Computation of Foundation Stiffness

The stiffness of the pile foundation in Equation 2 (coupled spring model) can be theoretically estimated using the existing formulations in Table 5 in the absence of careful and detailed site measurement data. Before selecting the right formula for computing the soil's stiffness theoretically, the principles explained in this section must be followed thoroughly. The calculation methodology for theoretical foundation stiffness depends on the following parameters: pile slenderness/rigidity; soil condition and ground profile at site. [25] In this section, detail explanation is giving on how the spring stiffness of the coupled foundation model (section 3.5) can be computed theoretically taking into account pile slenderness/rigidity, soil condition and ground profile at site.

3.4.1 Soil Conditions and Ground Profile at site

Soil condition and ground profile at site can be categorized into four main types which are cohesive soils, cohesionless soils, bed rock and complex layered soils. Figure 23 shows the depth-wise variation of the soil undrained shear strength (S_u). [18]

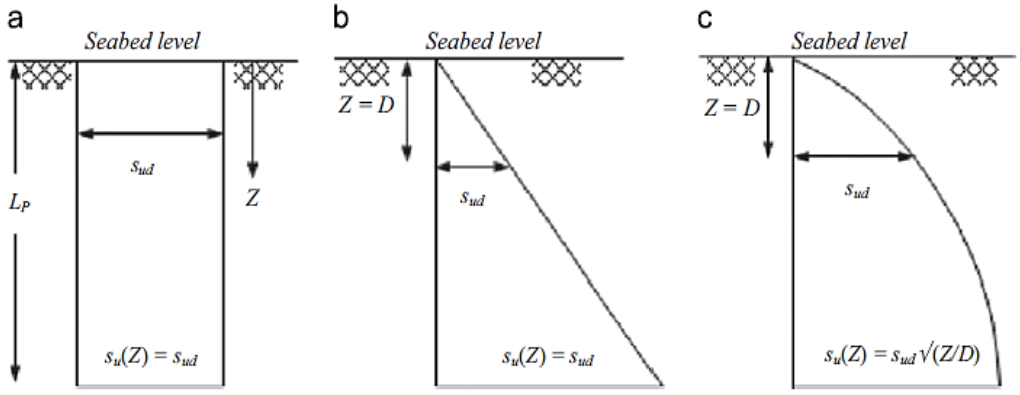

Figure 23: Depth-wise variation of undrained shear strength of soil: a) homogeneous, b) linear and c) parabolic [18]

In cohesive soils, the horizontal modulus of subgrade reaction (k_h) is considered to be constant with depth below the mud-line. Over-consolidated clayey soils often found offshore are considered to have a horizontal modulus subgrade reaction that is constant with depth. Furthermore, the undrained shear strength is uniform as illustrated in Figure 23a. However, the subgrade reaction is assumed to increase linearly with depth for normally consolidated cohesive soils. The constant horizontal modulus of subgrade reaction can be found using Equation (6). In addition, it can also be calculated using the secant young's modulus E_{50} or in terms of the undrained shear strength (S_u). It is used to calculate the foundation stiffness theoretically in Table 5. [25]

$$k_h = \frac{0.65}{D_p} \sqrt[12]{\frac{E_S\, D_p^4}{E_p I_p}} \left(\frac{E_S}{1-\nu_s^2}\right) \tag{6}$$

Where k_h in KN/m^3, I_p is the second moment of area of the pile, D_p is the monopile diameter E_s is the elastic modulus of the soil, E_p is the elastic modulus of the pile and v_s is the poisson's ratio of the soil.

In cohesionless soils, the horizontal modulus subgrade reaction is considered to increase with the square root of the depth below the mud-line which is typical for loose to medium dense sand and gravel. The linearly depth varying modulus of subgrade reaction of cohesionless soils (k_h) can be found using Equation (7). Furthermore, the modulus of subgrade reaction can also be found from Figure 24 knowing the relative density of the soil and the angle of internal friction. The coefficient of subgrade reaction η_h is used for calculating the foundation stiffness theoretically in Table 5. [25]

$$k_h = \eta_h \frac{z}{D_p} \tag{7}$$

Where z is the depth from the soil surface in m, D_p the monopile diameter in m and η_h in kN/m^3 is the coefficient of subgrade reaction which can be measured or calculated for sand using Equation (8) where γ_{sand} is the specific weight of sand in kN/m^3 and the constant A is given in Table 2.

$$\eta_h = \frac{A.\gamma_{sand}}{1.35} \tag{8}$$

Table 2: Values of A for different sand type [25]

Soil types	Loose sand	medium sand	dense sand
A	100 - 300	300 - 1000	1000 - 2000

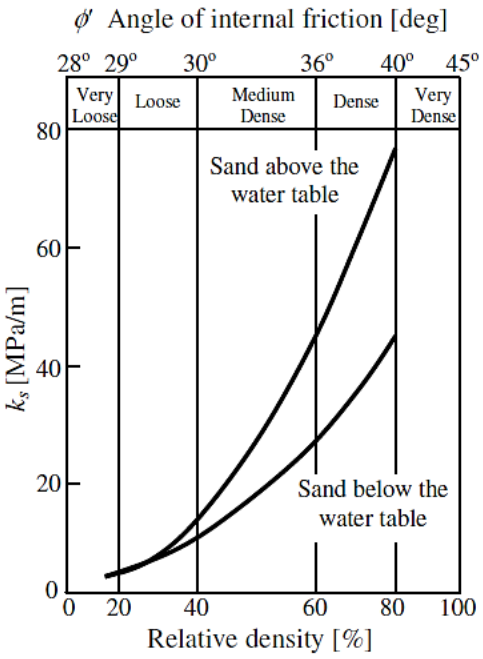

Figure 24: Initial modulus of subgrade reaction k_s (k_h) as a function of ϕ' [19]

In bedrock soils, the shear modulus of the soil determines the foundation stiffness which is typical for very dense sand and weathered bedrock. [25] In complex layered soils which is typical for real soil sites, one of the above categories may be chosen bearing in mind that for pile head deflection/ rotation and pile stiffness, the upper layers of the soil are of greater importance and should be weighted accordingly. The stiffness for this kind of sites can be more accurately obtained from the p-y curves. [25]

The soil design parameters are generally measured for site specific information. In the absence of these site specific soil properties, the soil design parameters can be selected from available data tables. For example, Table 3 can be used for the selection of design parameters if the soils (Cohesionless soils) fall within the range of soil density presented or the materials do not have unusual weak grains. [22]

Table 3: Design parameters for cohesionless Siliceous soils [22]

Density	Soil Description	Soil-Pile Friction Angle, δ Degrees	Limiting Skin Friction Values kips/ft^2 (kPa)	N_q	Limiting Unit End Bearing Values kips/ft^2 (MPa)
Very Loose	Sand	15	1.0 (47.8)	8	40 (1.9)
Loose	Sand-Silt**				
Medium	Silt				
Loose	Sand	20	1.4 (67.0)	12	60 (2.9)
Medium	Sand-Silt**				
Dense	Silt				
Medium	Sand	25	1.7 (81.3)	20	100 (4.8)
Dense	Sand-Silt**				
Dense	Sand	30	2.0 (95.7)	40	200 (9.6)
Very Dense	Sand-Silt**				
Dense	Gravel	35	2.4 (114.8)	50	250 (12.0)
Very Dense	Sand				

*The parameters listed in this table are intended as guidelines only. Where detailed information such as in situ cone tests, strength tests on high quality samples, model tests, or pile driving performance is available, other values may be justified.
**Sand-Silt includes those soils with significant fractions of both sand and silt. Strength values generally increase with increasing sand fractions and decrease with increasing silt fractions.

3.4.2 Slenderness and Rigidity of Pile

Monopile foundation can be idealized as "slender" or "rigid" depending on its failure mechanism. A monopile foundation is considered to be slender or infinitely long if the pile fails first by yielding through a plastic hinge (as opposed to the failure of the soil). On the other hand, it is idealized as rigid or infinitely stiff if the pile undergoes rigid body rotation such that the soil fails first. There exists several methods for evaluating the slenderness or rigidity of piles. One of these methods consists of using the modulus subgrade reaction (k_h) and the bending stiffness of the pile (E_pI_p). The slenderness parameter (β) can be calculated by equation (9). The slenderness/ rigidity of pile is defined as described in Table 4. L_p in Table 4 is the pile embedded length. [25]

$$\beta = \sqrt[4]{\frac{k_h D_p}{4E_p I_p}} \tag{9}$$

Table 4: Pile slenderness and rigidity [25]

Slenderness/rigidity of pile	Slender or infinitely long	Rigid or infinitely stiff
βL_p	>2.5	<1.5

3.5 Foundation Stiffness Formulations

The foundation stiffness of the coupled spring model can be approximated using the formulae provided in Table 5 developed based on the soil condition and pile slenderness explained in section 3.4. According to Laszlo Arani, S. Barttasharya, John H. G. Macdonald and S. John Hogan (2016) [25], these formulae were proven to provide a good approximation in terms of natural frequency. The principles provided in subsections 3.4.1 and 3.4.2 should be followed before selecting the right formulae from Table 5 for theoretically computing site specific foundation stiffness. [25]

Table 5: Theoretical pile-foundation stiffness formulations [25]

	Slender pile	Rigid pile
Cohesive soil Constant K_h	$\begin{bmatrix} F \\ M \end{bmatrix} = \begin{bmatrix} \frac{k_h D_p}{\beta} & -\frac{k_h D_p}{2\beta^2} \\ -\frac{k_h D_p}{2\beta^2} & \frac{k_h D_p}{2\beta^3} \end{bmatrix} \begin{bmatrix} x \\ \varphi \end{bmatrix}$	$\begin{bmatrix} F \\ M \end{bmatrix} = \begin{bmatrix} k_h D_p L & -\frac{k_h D_p L^2}{2} \\ -\frac{k_h D_p L^2}{2} & \frac{k_h D_p L^3}{3} \end{bmatrix} \begin{bmatrix} x \\ \varphi \end{bmatrix}$
Cohesionless soil Linear K_h	$\begin{bmatrix} F \\ M \end{bmatrix} = \begin{bmatrix} 1.077\eta_h^{\frac{3}{5}}(E_p I_p)^{\frac{4}{5}} & -0.99\eta_h^{\frac{2}{5}}(E_p I_p)^{\frac{3}{5}} \\ -0.99\eta_h^{\frac{2}{5}}(E_p I_p)^{\frac{3}{5}} & 1.485\eta_h^{\frac{1}{5}}(E_p I_p)^{\frac{4}{5}} \end{bmatrix} \begin{bmatrix} x \\ \varphi \end{bmatrix}$	$\begin{bmatrix} F \\ M \end{bmatrix} = \begin{bmatrix} \frac{1}{2}L^2\eta_h & -\frac{1}{3}L^3\eta_h \\ -\frac{1}{3}L^3\eta_h & \frac{1}{4}L^4\eta_h \end{bmatrix} \begin{bmatrix} x \\ \varphi \end{bmatrix}$
Bedrock-shear modulus G_h based	$\begin{bmatrix} F \\ M \end{bmatrix} = \begin{bmatrix} 3.15G^* D_p \left(\frac{E_e}{G^*}\right)^{\frac{1}{7}} & -0.53G^* D_P^2 \left(\frac{E_e}{G^*}\right)^{\frac{3}{7}} \\ -0.53G^* D_P^2 \left(\frac{E_e}{G^*}\right)^{\frac{3}{7}} & 0.25G^* D_P^3 \left(\frac{E_e}{G^*}\right)^{\frac{5}{7}} \end{bmatrix} \begin{bmatrix} x \\ \varphi \end{bmatrix}$	$\begin{bmatrix} F \\ M \end{bmatrix} = \begin{bmatrix} \frac{3.15G^* D_p^{\frac{2}{3}} L^{\frac{1}{3}}}{1-0.28\left(\frac{2L}{D_p}\right)^{\frac{1}{4}}} & -\frac{2G^* D_p^{\frac{7}{8}} L^{\frac{9}{8}}}{1-0.28\left(\frac{2L}{D_p}\right)^{\frac{1}{4}}} \\ -\frac{2G^* D_p^{\frac{7}{8}} L^{\frac{9}{8}}}{1-0.28\left(\frac{2L}{D_p}\right)^{\frac{1}{4}}} & \frac{4G^* D_p^{\frac{4}{3}} L^{\frac{5}{3}}}{1-0.28\left(\frac{2L}{D_p}\right)^{\frac{1}{4}}} \end{bmatrix} \begin{bmatrix} x \\ \varphi \end{bmatrix}$

Where k_h is the modulus of subgrade reaction; F is the lateral force at mudline (Figure 18); M is the over turning moment at mudline (Figure 18); x is the mudline pile-head lateral displacement (Figure 18); φ is the rotation of the pile-head at mudline; D_p is the pile diameter; I_p is the second moment of area of the pile; E_e is the pile equivalent young's modulus; E_p is the elastic modulus of the pile; η_h is the coefficient of subgrade reaction defined in Equation 8; β is the slenderness parameter defined in Equation 9; L is the pile length; G^* is the soil equivalent shear modulus.

4 Load Modelling

General theory on some load models used to numerically compute wave, wind and ice loads is provided in this chapter. The models presented here are used later on in chapter 5 to evaluate wave, wind and ice loads in the case study taking into account site specific environmental conditions in Tahkoluoto used in the reference simulation.

The design, installation and analysis of offshore structures are quite challenging due to the complexity and uncertainties of the marine environment. The applied vertical loads are usually smaller than the over-tuning loads from wind and wave due to the lightweight of the turbine structure. The horizontal loads comprises of wind and wave (or wind and ice). During the worst loading case, the turbine operates at moderate wind while the sea is in an extreme condition. Generally, the load cases where the turbine operates at extreme wind and sea conditions are not critical due to the fact that the blades are fluttered during extreme winds. The wind load contributes 25% the horizontal load but 75% of the over-tuning moment because it is applied at a high level. [16] Figure 25 illustrates the loads an offshore wind turbine in ice-covered sea can be exposed to during winter. These loads vary in time. The data for wind and wave properties can be obtained by direct measurement, satellite observations or theoretical models developed for wind and wave fields. [19, 20]

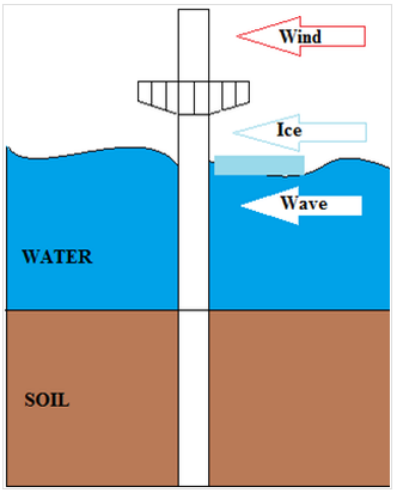

Figure 25: Monopile foundation profile [20]

4.1 Wave

Offshore wind turbines are exposed to hydrodynamic loads such as wave loads and current loads. Wave loading on monopile wind turbines is an important design criterion. Current loads are not considered in this analysis and can be ignored in case of inertia dominated waves or if the current velocity is small and negligible. Waves are characterized by a depth parameter (kd_w), wave steepness (h_w /L) and a spectrum if irregular. k is the wave number, d_w is the depth, h_w is the wave height and L is the wavelength. Waves can be classified into three main types depending on the water depth: shallow-water waves ($kd_w < 0.3$), deep-water waves ($kd_w > 3$) and intermediate-depth waves ($0.3 < kd_w < 3$). Generally, offshore wind turbines are installed in intermediate to shallow water with depth less than half a wavelength. [18, 26]

4.1.1 Wave Load

The wave load on a slender monopile structure can be estimated using Morison's equation in Equation 9. If the structure itself is also moving which is usually the case for floating offshore turbines, then its velocity should be accounted for and added to the equation. If the current velocity is significant, its effect can also be incorporated into the Morison's wave load equation. The induced wave velocity and acceleration of the water are time dependent and can be computed using linear wave theory given by the Equation (11a) and (11b). [18, 26, 27]

$$F_{wave} = F_M + F_D = \frac{1}{4} C_M \rho \pi D^2 \ddot{u} + \frac{1}{2} C_D \rho D \dot{u} |\dot{u}| \tag{10}$$

Where F_{wave} is the wave force per unit meter in N/m; F_M is the inertia force per unit meter in N/m; F_D is the drag force per unit meter in N/m; d_w is the water depth in m; C_M is the mass coefficient generally 2 for a smooth tubular section; C_D is the drag coefficient generally 0.7 for a smooth tubular section; ρ is the mass density of the sea water kg/m^3; D is the diameter of the monopile in m; $\ddot{u}$ is the wave induced acceleration of the water in horizontal direction; u is the wave induced velocity of the water in horizontal direction. [18, 26, 27]

$$\dot{u} = \frac{h_w \pi}{T_w} \frac{\cosh\left(k(z_2 + d_w)\right)}{\sinh(k d_w)} \cos(kx - \omega_w t) \tag{11a}$$

$$\ddot{u} = \frac{2 h_w \pi^2}{T_w^2} \frac{\cosh\left(k(z_2 + d_w)\right)}{\sinh(k d_w)} \sin(kx - \omega_w t) \tag{11b}$$

Where h_w is the wave height (m); k is the wave number (m^{-1}) given by $k = 2\pi/\lambda_{wave}$ where λ_{wave} is the wavelength in m; ω_w is the wave frequency (rad/s); T_w is the wave period (s); z_2 is the depth below the sea surface (m); x is the horizontal position (m). [19, 20]

4.1.2 Diffraction

Morison's theorem assumes that the submerged members on which the wave loads are calculated do not affect the wave. This work quite well with cylinder diameter relatively very small compared to the wave length. However for larger diameter ($D > 0.2\ \lambda_{wave}$) structures such as offshore wind turbines installed in shallow water with reduced wavelength, the effect of the structure on the wave must be incorporated into Morison's equation. This effect is referred to as diffraction. The effect of the structure on the wave is incorporated into Morison's equation by incorporating the MacCamy-Fuchs correction factor which reduces the magnitude of the of the inertia coefficient. The correction factor depends on the ratio of the monopile diameter over the wavelength (D/λ_{wave}). In Figure 26, it can be observed that the inertia coefficient C_m reduces with increasing ratio (D/λ_{wave}). Small structures are referred to those with small kD and large AD (k = wave number and A= wave amplitude) while large structures are those with $kD > 1$ and small AD. [19, 28, 29]

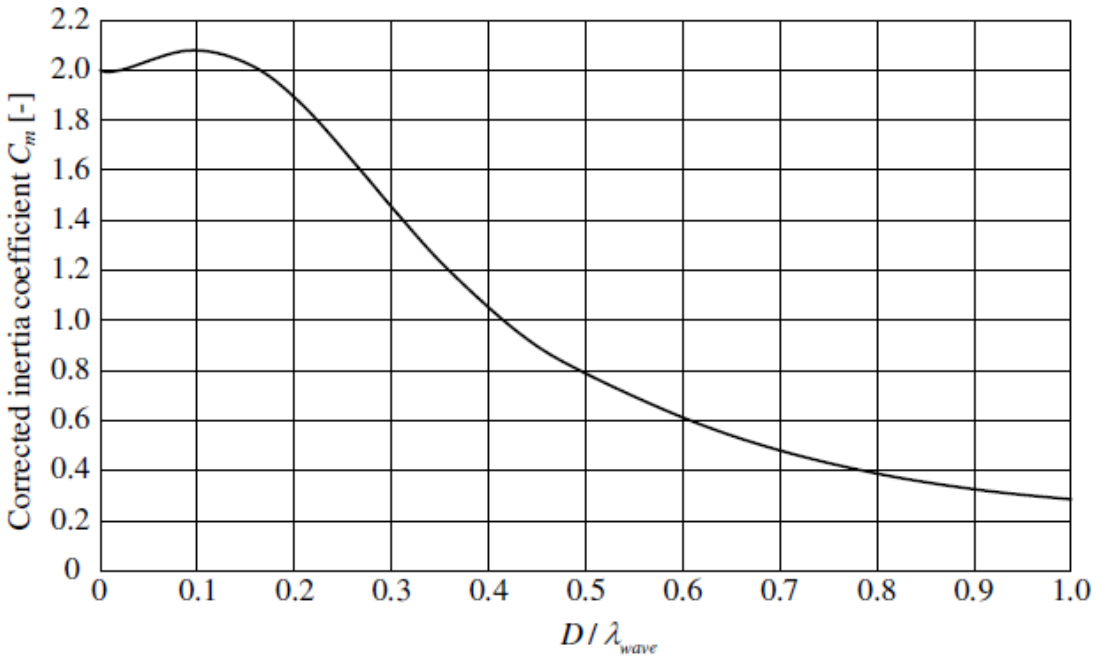

Figure 26: MacCamy-Fuchs diffraction correction of the inertia coefficient C_m in the Morison's equation for cylinder diameter over wavelength [19]

4.1.3 Breaking Waves

Unstable wave crest may lead to breaking waves. Waves are assumed to break when $h_w / d_w > 0.78$. During intense wave breaking, there's air entrainment which results in white-capping. The maximum wave height can be limited by breaking wave limit or due to reduce water depth at the site or in the vicinity. The linear wave theory does not completely describe the non-linear features of extreme waves when used for computing the wave loads on a structure. It is important to evaluate the probability of breaking waves at a specific offshore wind farm site as waves breaking directly onto the pile may induce large loads on the structure. There are many theories available to quantify breaking waves such as approaches based on wave steepness and acceleration. The applicability of various wave theories is summarized by LeMehaute in Figure 27. In Figure 27, the vertical axis illustrates the non-dimensionalized wave height plotted against the non-dimensionalized water depth on the horizontal axis. [19, 28] Det Norske Veritas (DNV) proposed Equation 12 for calculating the load of breaking wave on structures (F). [19, 28]

$$F = \frac{1}{2}\rho_{water} C_s A u^2 \tag{12}$$

Where ρ_{water} is the water density in Kg/m^3; C_s is the slamming coefficient generally 2 - 6.3; A is the area exposed to breaking waves m^2; u is the water particle velocity in breaking wave crest in m.

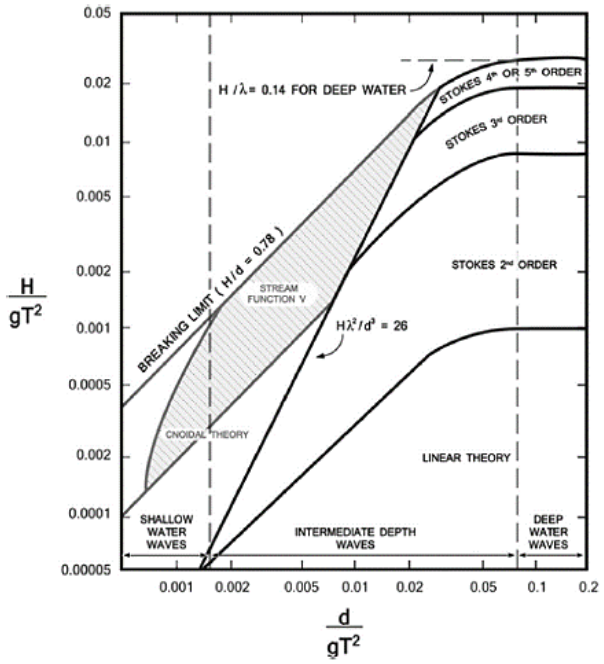

Figure 27: Approximate regions of applicability for different wave theories, depending on wave height and water depth from LeMehaute [28]

4.2 Wind

The models used to evaluate the wind loads acting on the turbine's blades and tower are presented in this subsection. In addition, this subsection presents the models used to evaluate the average wind speed which is a function of turbine's height. These models are used later on in chapter 5.

4.2.1 Wind Load

The total wind load acting on a wind turbine can be classified into two components: the load acting on the turbine blades (F_b) and the load acting on the turbine tower (F_t). It should be noted that the frequency of wind load is same as the rotor frequency. More details on the aerodynamic load acting on the blades can be found in appendix 1. [18]

$$F_b = \frac{1}{2}\rho_a A V^2 C_T(\lambda_s) \tag{13}$$

Where F_b is the wind load acting on the hub in N; V is the speed of the wind at the hub height in m/s; ρ_a is the density of air in Kg/m^3; A is the cross section area of the rotor in m^2 given by $A = \pi R_r^2$ with R_r being the rotor radius in m; $C_T(\lambda_s)$ typically 0.7 for a tubular tower, is the thrust coefficient which is as a function of the tip speed ratio (λ_s).

The wind load acting on the turbine tower can be divided into two components: the load acting on the part of the tower unobstructed and the load acting on the part of the tower obstructed by the movement of the blades. The wind load on the tower is found using the equation below. [18, 19]

$$F_t(z) = 0.61V^2(z)C_hC_sD \quad (14)$$

Where F_t is the wind load acting on the tower per unit meters in N/m; D is the diameter of the tower in m; $V(z)$ is the wind velocity profile in m/s as a function of the tower height (Figure 29); C_h is the height coefficient for tower's height ranging from 0 to 100m (C_h varies from 1 to 1.58); C_s is the shape coefficient which is generally 0.5 for cylindrical structure. [18, 19]

4.2.2 Wind speed

Undisturbed wind velocity is variable in space, time and direction. The varying character of the wind which is generally time depended can be captured in a wind spectrum showing variable frequency ranges if the measurement period is quite long. An example of a wind spectrum by Van Der Hoven is shown below in Figure 28. In Figure 28, the frequency range at the left hand side (Mesometeorological range) shows the yearly changes, pressure system and diurnal changes while at the right hand side (Micrometeorological range) the turbulence is presented. The spectral gap separates the slowly changing and the turbulent ranges. The wind speed over this frequency range (10 minute to 1 hour) does not change. [19, 27]

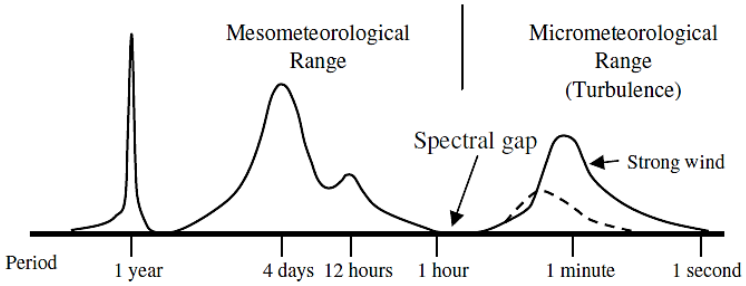

Figure 28: Wind speed spectrum over a wide range of frequencies [19]

Since the wind speed varies constantly, it should be expressed in terms of mean wind speed. The mean wind speed increases with height as shown in Figure 29. This is related to the fact that wind is decelerated at low heights as a result of the friction between the moving air and the earth's surface. The mean wind speed over a short period of time (3-10s) is referred to as gust. [19, 27]

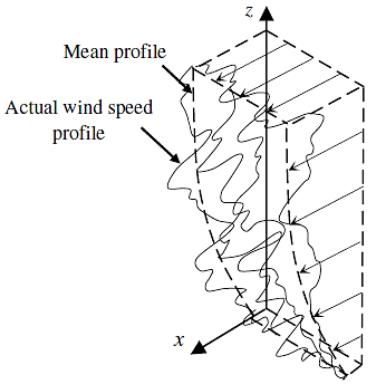

Figure 29: Mean wind speed profile as a function of height [19, 27]

From about 2 km above the ground to the surface, the mean wind speed decreases and is almost zero at the surface. The vertical wind variation of the mean wind speed can be expressed by two main models most commonly used: the logarithmic profile and the power law profile as described by Equation (15a) and (15b). Both models are commonly used and do not result in any significant differences in the average wind speed. A sensitivity test run on both mean wind speed models is provided in the appendix (Appendix 2). [19, 27] Table 6 shows the typical values for the surface roughness length and the power law coefficient for different types of terrain. Z_0=0.20mm for a calm open sea and 0.50mm for a rough sea. [1, 19, 27]

$$V(z) = V_{w,r} \frac{\ln\left(\frac{z}{z_0}\right)}{\ln\left(\frac{z_r}{z_0}\right)} \tag{15a}$$

$$V(z) = V_{w,r} \left(\frac{z}{z_r}\right)^{\alpha_{shear}} \tag{15b}$$

Where $V(z)$ is the mean wind speed at height z in m/s; $V_{w,r}$ is the mean wind speed at reference height z_r in m/s; z is any given height in m; z_r is the reference height in m; z_0 is the surface roughness length in m; α_{shear} is the power law coefficient. [19, 27]

Table 6: Roughness length and power law factor for different types of terrain [19]

Type of terrain	z_0 [m]	α_{shear}
City centres	1-10	0.40
Cities, forests	0.7	
Suburbs, wooded country side	0.3	0.30
Villages, countryside with trees and hedges	0.1	
Open farmland, few trees and buildings	0.03	0.16
Flat grassy plains	0.01	
Flat desert, rough sea	0.001	0.12
Calm sea	0.0002	

4.2.3 Extreme Wind Speeds and Gusts

There are two main kinds of extreme wind load cases which are the extreme hourly wind speed with given return period (1, 50, 100 years) and the extreme incident wind speed within a given short period of time [19, 27]. There are design standards such as the IEC that prescribes extreme wind speed for different classes for the design of onshore wind turbines (Table 7). However, these classes are not directly related to specific sites. Therefore offshore sites require site-specific analysis. The site-specific analysis for offshore wind turbines can be based on extreme measured values and a Gumbel distribution. The extreme incident wind speed or gust wind speed within a certain time interval can be computed using the tail of the turbulence spectrum or the approximate formulation derived by Wieringa as prescribed by Equation (16). [19]

$$V_{gust}(t) = G(t).V(z) \tag{16a}$$

Where $V_{gust}(t)$ is the gust wind speed for the duration t; $V(z)$ is the mean wind speed at height z given by Equation (15a) and (15b); $G(t)$ is the gust factor defined by Equation (16b) shown below.

$$G(t) = 1 + 0.42 I_t \ln \frac{3600}{t} \tag{16b}$$

Where t is the duration of the gust; I_t is the turbulence intensity in percentage given by Equation (16c) provided below.

$$I_t = \frac{\sigma}{V(z)} \% \tag{16c}$$

Where σ is the standard deviation of the time varying wind speed in m/s. The turbulence intensity depends on the height and roughness of the terrain. Higher turbulence intensities occur at rougher terrain with lower altitude. Figure 30 illustrates the recommended turbulence intensities as a function of wind speed for different standards which can be selected for design load cases. [19]

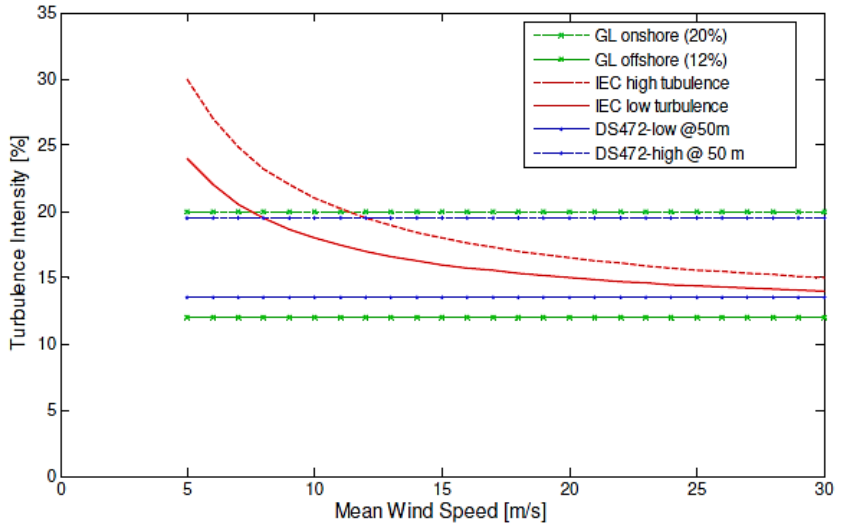

Figure 30: Turbulence intensity as a function of wind speed from different standards [19]

Table 7: Location classes according to IEC with yearly hourly mean wind speed ($V_{w,\,ext\,1h}$) and extreme 10-minute mean wind speed ($V_{w,\,ext\,10min}$) in m/s at the hub height [19]

Class	I	II	III	IV
$V_{w,\,ext\,1h}$ [m/s]	10	8.5	7.5	6.0
$V_{w,\,ext\,10min}$ [m/s]	50	42.5	37.5	30

4.2.4 Extreme Operating Gust Model

The dynamic effect of the wind load is evaluated in this thesis by assuming extreme operating gust wind load model in chapter 5. According to IEC61400-1, the wind speed for extreme operating gust is given by the equation below. [44]

$$V(z,t) = \begin{cases} V(z) - 0.37V_{gust}\sin\left(\frac{3\pi t}{T}\right)\left(1-\cos\left(\frac{2\pi t}{T}\right)\right) & For\ 0 \le t \le T \\ V(z) & Otherwive \end{cases} \quad (17)$$

Where T is the period; t is the time; $V(z)$ is the wind speed as a function of the tower height described by Equation (15); V_{gust} is the gust speed given in Equation (16). [44]

4.3 Ice

This section presents the models used to define horizontal ice loads on offshore wind turbines. As can be observed from subsection 4.3.1 and 4.3.2, the load models used to describe the horizontal ice load on monopiles with ice-breaking cone (conical structures) is different from that which is used to describe the horizontal ice load on monopiles without ice-breaking cone (horizontal structures). Since only monopile foundation without ice-breaking cone is considered in this thesis, only the equation presented in subsection 4.3.1 will be used later on in chapter 5 to describe the horizontal ice load in Tahkoluoto.

Ice becomes mobile as a result of the activities of wind and wave. Due to the effect of wind and wave, ice sheets are forced against offshore structures thereby creating additional external force. Deformations resulting from the lateral ice load may be significant. [20] There are two different ways ice can affect wind turbines: Icing on offshore wind turbine blades and drifting-level-ice-induced ice loads. Ice load on offshore wind turbine blades will cause an increase in the mass and subsequently a change in the aerodynamic performance of wind turbines which may in turn result to increased dynamic loads and reduced power production. Drifting ice load on the other hand may induce dynamic loads that may result in failure of the support structures of offshore wind turbines. In addition, ice loads may lead to an increase in the cost of construction and maintenance of offshore wind turbines due to the additional risk it causes. Thus ice loads constitute an important criteria for offshore wind turbines design. Ice failure depends on the ice thickness, the ice drifting speed, and the geometry of the structure. It can be classified into two main types: The crushing mode which occurs against vertical structures and the flexural mode which occurs against sloping structures. [30]

4.3.1 Horizontal Ice Load on Cylindrical Structures

When ice collides with a cylindrical (vertical) structure (Figure 31), it undergoes compressive stresses leading to a compressive failure process referred to as ice crushing. Ice crushing mode can be classified into the follow types depending on the ice speed: Intermittent ice crushing, frequency lock-in crushing and continuous brittle crushing. Intermittent ice crushing may occur when an ice cover approaches the structure with relatively low speed and the ice loading period is much longer than the longest natural period of the structure, while frequency lock-in crushing occurs at intermediate ice speeds where the frequency of ice action correspond to the natural frequency at waterline. Continuous brittle crushing consists of random ice action and structural response. [30, 31] IEC 61400-3, DNV-OS-J101 and GL Guideline propose the Korzhavin equation (Equation (18)) for the estimation of the global static

force on vertical structures. According to GL Guideline for the Construction of Fixed Offshore Installations in Ice Infested Water States, the Korzhavin equation should only be used when $D/h < 6$. [31]

$$F = k_1 k_2 k_3 h D \sigma_c \tag{18}$$

Where k_1 is the shape factor for the shape of the support structure on the ice impact side; k_2 is the contact factor for the ice contact against the support structure; k_3 is the factor for the ratio between ice thickness and the support structure diameter; h is the ice thickness in m; D is the diameter of width of the structure in m; σ_c is the compressive or crushing strength of ice in MPa. [29]

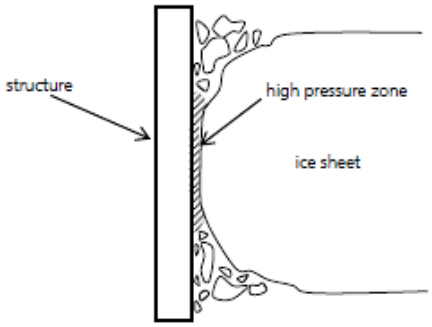

Figure 31: Ice Crushing Failure: Sketch according to ISO (2010) [31]

4.3.2 Horizontal Ice Load on Conical Structures

To reduce the effect of ice loads, conical structures are proposed for most offshore structures. Generally, an ice breaking cone is added to offshore wind turbine towers at the mean sea level in other to mitigate the ice loads by changing the failure modes from crushing to bending (Figure 33). Ice loads magnitude and ice-induced structural response of sloping or conical structures are much lower when compared to cylindrical structures with the same waterline diameter. The ice sheet may be broken downwards (Figure 34) or upwards (Figure 32) depending on the geometry of the conical structure. Different analytical models describing ice sheet failure exist e.g. Ralston's method based on plastic limit analysis, Croasdale's method based on elastic bending of a beam on an elastic foundation and the plastic method for cones. IEC and ISO standard proposed different design load cases for offshore wind turbines located in the Baltic Sea as shown in Figure 34. [30, 31]

IEC 61400-3 and DNV-OS-J101 propose Ralston's equation to calculate static ice on conical structures. This equation can be applied to downward and upward breaking cones. Only the horizontal load component is presented in this document since it focuses in the lateral response of offshore wind turbines support structures. The Horizontal component of force on upward breaking cone (Figure 33) can be found using the equation below. [31]

$$F_H = A_4\left(A_1 \sigma_b h^2 + A_2 \rho_w g h D^2 + A_3 \rho_w g h (D^2 - D_T^2)\right) \tag{19}$$

Where A_1, A_2, A_3 are dimensionless coefficients; σ_b is the bending strength of ice in MPa; h is the ice thickness in m; ρ_w is the water density in Kg/m^3; g is the gravitational acceleration

m/s^2; D is the cone diameter at the waterline in m; D_T is the cone diameter at the top of the cone. [31]

Figure 32: Upward ice breaking cone [31]

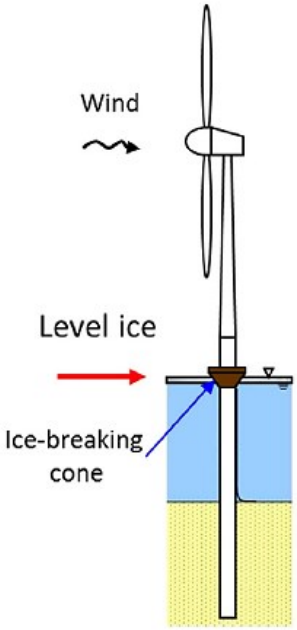

Figure 33: Monopile wind turbine with ice breaking cone [30]

For downward breaking cones, Ralston's equation given above for the horizontal force component is used with ρ_w changed to $1/9\rho_w$. This simply means that lower ice load apply for downward breaking cone. The horizontal component of the force on downward breaking cone is given by the equation below. [30, 31]

$$F_H = A_4\left(A_1\sigma_b h^2 + A_2\frac{\rho_w}{9}ghD^2 + A_3\frac{\rho_w}{9}gh(D^2 - D_T^2)\right) \quad (20)$$

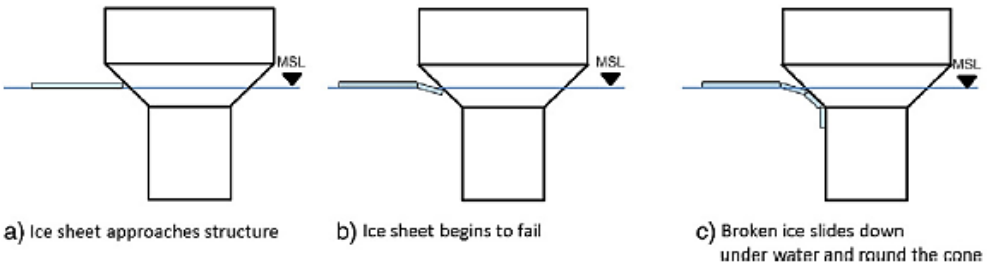

Figure 34: Interaction between a sloping structure (downward breaking cone) and level ice [30]

4.3.3 Dynamic Ice Load

Dynamic ice load applied to offshore wind turbines can induce extreme structural vibration and large displacements of the support structure at waterline. Ice load time series for intermittent crushing can analyzed according to the graph provided by ISO (2010) illustrated in Figure 35. Figure 35 shows the time histories of ice actions of period T with loading and unloading phases. The period of ice action equals the duration of loading/unloading cycles. F_{max} is the maximum horizontal ice load calculated using Korzhavin equation (Equation (18)). This model is used in chapter 5 to estimate the ice load time history in Tahkoluoto. [31]

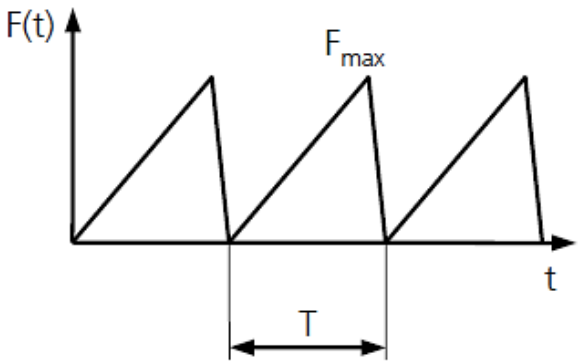

Figure 35: Ice load history for intermittent crushing, sketch according to ISO (2010) [31]

5 Case Study

To analyze the structural response of offshore wind turbines under wind, wave and ice load whilst using the coupled spring foundation model to describe the interaction between soil-monopile, finite element modelling was carried out on a 5 MW baseline offshore wind turbine using the engineering software called Abaqus. In this chapter, a brief information on the wind turbine specifications used for the finite element modelling in this project is presented. In addition, information regarding the specific location at the Gulf of Bothnia considered in this thesis is provided.

The spring stiffness of the coupled spring model was calculated in this chapter using the appropriate formulations in Table 5 given the case study and the soil properties at a specific location at the Gulf of Bothnia called Tahkoluoto. The calculation process is explained in section 5.3. The soil stiffness calculated in this chapter is used later on as boundary conditions in the finite element modelling in order to take into account the effect of the soil-monopile interaction (Chapter 6).

The wind, wave and ice loads in Tahkoluoto are calculated (section 5.4, 5.5 and 5.6) using the load models presented in chapter 4 and the environmental conditions present in Tahkoluoto. The calculated loads are used later on in chapter 6 as input loads for finite element analysis. It should be noted that the coordinate system used for calculating the wave and wind loads is different from that which is used in the finite element modelling. In the load calculations in this chapter, z-axis is the vertical axis whereas in the finite element modelling in chapter 6 y-axis is the vertical axis (Figure 45). It should be noted that at first the loads used as input for finite element modelling when the turbine is under wind, wave and ice loads applied separately were calculated using most of the environmental properties of Tahkoluoto (Gulf of Bothnia) used in a previous simulation done by VTT. This is because the structural response under these loads is later validated using the result of the said previous simulation. However the parameters proposed by IEC 64100-1 according to the design load cases selected (section 6.3), were used to evaluate the loads used to simulate the structural response of the turbine under combined loads.

5.1 5-MW Baseline Wind Turbine Specifications

The 5 MW baseline wind turbine used for finite element modelling in this project consisted of a rotor diameter of 126 m, a tower height of 77.6 m and monopile diameter of 6 m. The monopile was 45 m long with 15m of its length considered to be embedded underneath the seabed and 30 m above the seabed (Figure 45). The water depth considered here was 10 m. The material of the tower is steel. This turbine is called the "NREL offshore 5-MW baseline wind turbine" sponsored by the National Renewable Energy Laboratory (NREL). This turbine is actually a testing prototype used as reference turbine for testing and research in the aim to develop offshore systems and to aid in the standardization of baseline offshore wind turbine specifications. A summary of the properties of the 5 MW baseline wind turbine considered in this thesis is presented the table below. [49]

Table 8: Gross properties considered for the "NREL 5-MW Baseline Wind Turbine" used for finite element modelling in this thesis [49]

Rating	5 MW
Rotor Orientation, Configuration	Upwind , 3 Blades
Control	Variable Speed, Collective Pitch
Drivetrain	High Speed, Multiple stage Gearbox
Rotor, Hub Diameter	126 m, 3 m
Hub Height	90 m
Cut-in, Rated, Cut-out Wind Speed	3 m/s, 11.4 m/s, 25 m/s
Cut-in, Rated Rotor Speed	6.9 rpm, 12.1 rpm
Rated Tip Speed	80 m/s
Overhang, Shaft Tilt, Precone	5 m, 5°, 2.5°
Rotor Mass	110,000 kg
Nacelle Mass	240,000 kg

5.2 Gulf of Bothnia

The Gulf of Bothnia as illustrated in Figure 36 is the northernmost prolongation of the Baltic Sea located between Finland's west coast and the east cost of Sweden. [37]

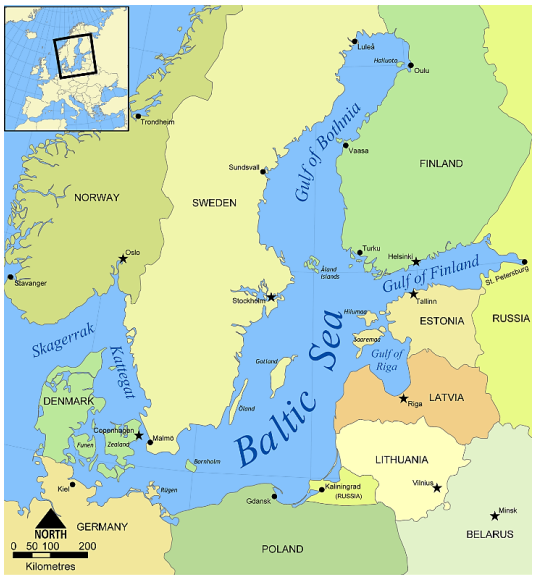

Figure 36: Map of the Baltic Sea showing the Gulf of Bothnia [36]

The Gulf of Bothnia has an average depth of about 60m and a maximum depth of about 295m. It is 725 km long and about 80-240 km wide. Its surface area is about 117,000 km². The land in the Gulf rises after being pressed down by the continental ice during the last ice age. This has led to a constant decrease in the depth and surface area of the Gulf of Bothnia. The land rises to about 80 cm every hundred years. The salinity of the gulf varies from the north to the south due to the fact that a number of rivers flow into the gulf. The gulf is frozen for over five months yearly. [36, 37] The area at the Gulf of Bothnia considered in this thesis is called Tahkoluoto. Tahkoluoto is the area highlighted in red in Figure 37. Tahkoluoto is located in the Meri-Pori area which is about 30 Km from the city. [38]

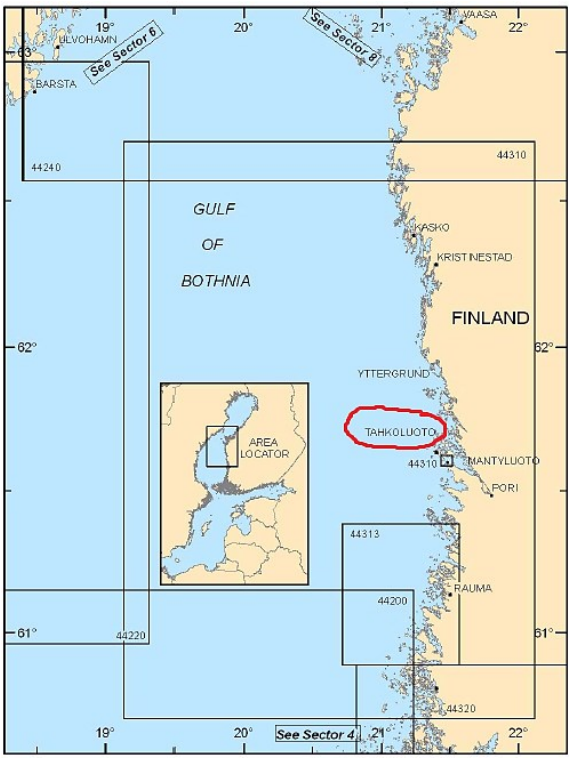

Figure 37: Gulf of Bothnia; Tahkoluoto highlighted in red [37]

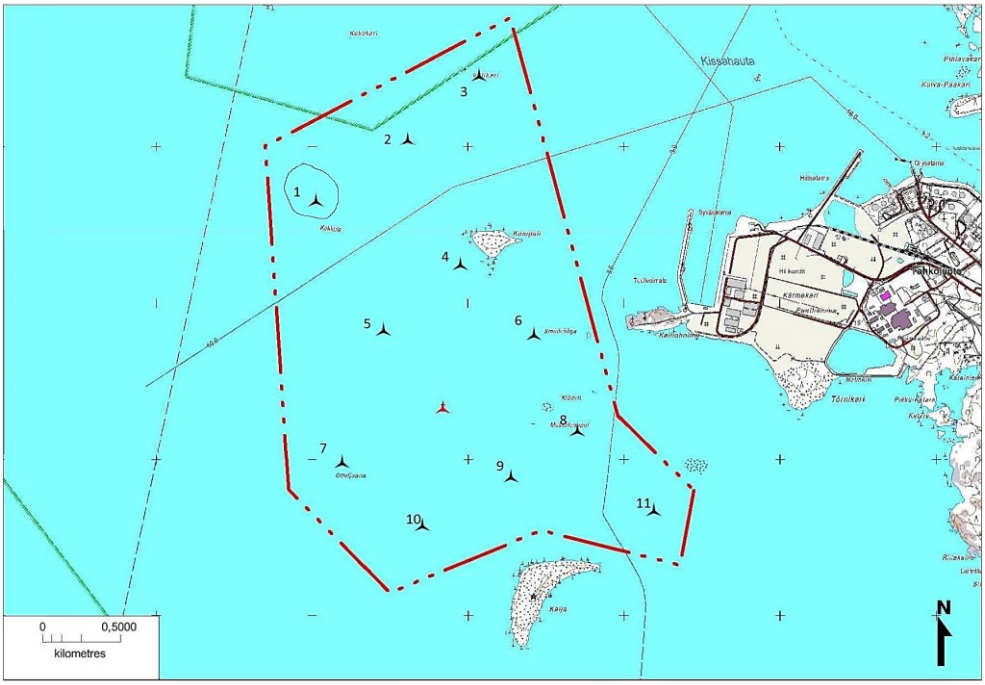

Figure 38: Wind energy project in Tahkoluoto layout sketched from reference; the numbered black symbols in the in area marked with red are planned turbines and the red symbol is an already installed turbine [42]

Tahkoluoto was announced to be one possible location for the first Finnish wind park (meri-tuulipuistolle) in January 2014. Figure 38 shows one of the going offshore wind turbine projects in Tahkoluoto. The numbers and turbine symbols in the area marked with red in Figure 38 represent planned turbines in their respective locations or positions for ongoing

offshore wind project in Tahkoluoto. The red turbine symbol represents already installed turbine which was built as a pilot turbine in 2010. The pilot turbine is similar to the baseline turbine used in this thesis. [38] The soil parameters and the environmental conditions used in the subsequent sections are those present in the area circled and marked with number 1 in Figure 38.

5.3 Foundation Stiffness

According to the site specific information provided for the area marked with number 1 in Tahkoluoto in Figure 38, the soil type is glacial till. Since the soil is mixed sediment including glacial clay, till, bedrock and other sediments, it was ambiguous as to whether to classify the soil type as cohesive or cohesionless which are crucial classification needed in the theoretical computation of the soil stiffness using the coupled spring model (as demonstrated in section 3.4). In this work, the soil was evaluated both as cohesive and cohesionless soil and a conclusion was reached. The cohesionless model gave two different results regarding foundation stiffness and consequently the lateral structural response. Detail information on one of the results is presented in Appendix 3. The structural response whilst considering the cohesive foundation model is presented in chapter 6. Emphasis was made on the cohesive foundation model because it was easier to find informations about the most critical soil parameter (Elastic modulus of the soil: Appendix 4) used in the cohesive model in the absence of site specific measurements. The foundation stiffness calculated using the cohesive and cohesionless model in this chapter are used later on as boundary conditions for the finite element modelling in chapter 6 and Appendix 4. The pile was evaluated to be rigid (Section 5.3.1) and the respective soil models were selected from Table 5.

5.3.1 Cohesive Soil Model

In this subsection, the properties of glacial till soil type used to compute the soil stiffness considering the cohesive model is initially presented after which the slenderness/rigidity of the monopile is tested. The founadtion stiffness is then calculated using the soil properties and Table 5.

A. Soil Properties

The elastic modulus of glacial till soil type can vary from 10-1440 MPa depending on whether it is loose (10-150 MPa), dense (150-720 MPa) or very dense (500-1440 MPa). In the following calculations, the soil is considered to be loose glacial till. The soil and monopile properties used for the cohesive model are listed as follows: The elastic modulus of the soil E_s considered is 144 MPa; The elastic modulus of monopile E_p is 210 Gpa; The Poisson ratio of cohesive undrained soil was chosen to be 0.5 (No information regarding the Poisson ratios of glacial till was found so a value was taken from the range of Poisson ratios of cohesive soils); The soil modulus of subgrade reaction for cohesive soil is calculated using Equation 6 giving K_h is 14859413 N/m^3; The second moment of area of the pile I_p is 4.94 m^4 calculated from Equation (20) where D (6 m) is the outer diameter of the pile and d (5.88 m) is the inner diameter of the pile. A summary of the soil parameters used to compute foundation stiffness whilst considering cohesive soil model is presented in Table 9. [45]

$$I_p = \frac{\pi(D^4 - d^4)}{64} \tag{21}$$

Table 9: Summary of cohesive soil parameters used

Elastic modulus of the soil E_s (MPa)	Elastic modulus of monopile E_p (GPa)	Soil poisson ratio ν_s	Soil modulus of subgrade reaction K_h (N/m^3)	Second moment of area pile I_p (m^4)	Pile Diameter D (m)	Pile embedded length L_p (m)
144	210	0.5	1.4859×10^7	4.94	6	15

B. Pile Slenderness/ Rigidity Test

The monopile slenderness/rigidity must be evaluated in order to choose the right equation in Table 5 to compute the soil stiffness theoretically. The slenderness/rigidity parameter β can be calculated using the Equation 9. The following parameters are used for the calculation: The modulus of subgrade reaction calculated for cohesive soil K_h is 14859413 N/m^3 (A. Properties); Pile diameter D_p is 6 m; Pile elastic modulus E_p is $2{,}1 \times 10^{11}$ N/m^2; Pile second moment of area I_p is 4.94 m^4; The pile length embedded into the soil L_p is 15 m; Thus, the slenderness/rigidity parameter β is 0.0681. According to Table 4, $\beta L_p = 1.0215 < 1.5$ implies that the pile is rigid.

C. Stiffness

According to Table 5, the soil stiffness for cohesive soil whilst considering rigid pile can be found using Equation 22.

$$\begin{bmatrix} F \\ M \end{bmatrix} = \begin{bmatrix} k_h D_p L & -\frac{k_h D_p L^2}{2} \\ -\frac{k_h D_p L^2}{2} & \frac{k_h D_p L^3}{3} \end{bmatrix} \begin{bmatrix} x \\ \varphi \end{bmatrix} \tag{22}$$

The soil modulus of subgrade reaction, the diameter of the pile and the pile embedded length used in Equation (22) have already been defined above. Taking into account Equation (6) and Equation (22), the soil stiffness can be calculated as follow: The lateral soil stiffness K_{xx} is 1.33735×10^9 N/m; the rotational soil stiffness $K_{\varphi\varphi}$ is 1.003×10^{11} Nm and the coupled soil stiffness $K_{x\varphi}$ is -1.003×10^{10} N.

5.3.2 Cohesionless Soil Model

In this subsection, the properties of glacial till soil type used to compute the soil stiffness considering the cohesionless model is initially presented after which the soil stiffness is calculated taking into account pile slenderness/rigidity evaluated in section 5.3.3 and Table 5. It was difficult to find the coefficient of subgrade reaction (most important soil parameter for the cohesionless model) for glacial till soil in the absence of site specific measurement. The information differ from one source to another therefore, in this section the soil stiffness is calculated using two different values of the coefficient of subgrade reaction found from two different sources in order to demonstrate the effect of the soil coefficient of subgrade reaction on the soil stiffness.

A. Properties

The coefficient of subgrade reaction is calculated using two different ways. In the first procedure, the coefficient of subgrade reaction is calculated using Figure 39. The internal angle of friction for glacial till ϕ is about 38 degree. Therefore its coefficient of subgrade reaction from Figure 39 will be about η_h = 10 MN/m^3. [40, 41]

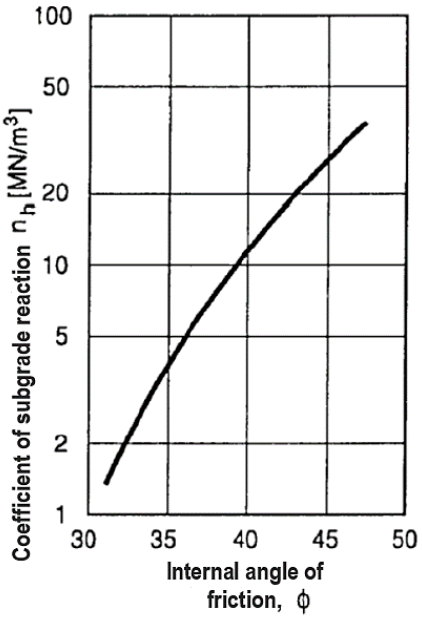

Figure 39: Soil coefficient of subgrade reaction as a function of the soil internal angle of friction [40]

According to Rasi-Koskinen Hanna (2014) [40], the product of the soil modulus of subgrade reaction and the pile diameter for glacial till soils gives $K_h.D_p$ = 30 MN/m^2. Using Equation 7, the coefficient of subgrade reaction (η_h) will be 2 MN/m^3.

B. Stiffness

According to Table 5, the soil stiffness for cohesionless soil whilst considering rigid pile can be found using Equation 23.

$$\begin{bmatrix} F \\ M \end{bmatrix} = \begin{bmatrix} \frac{1}{2}L^2\eta_h & -\frac{1}{3}L^3\eta_h \\ -\frac{1}{3}L^3\eta_h & \frac{1}{4}L^4\eta_h \end{bmatrix} \begin{bmatrix} x \\ \varphi \end{bmatrix} \tag{23}$$

The values of the coefficient of subgrade reaction calculated using two different references (Section 5.3.2, A. Properties) are quite different from each other (η_h = 10 MN/m^3 and η_h = 2 MN/m^3). Therefore, the soil stiffness will be calculated using both cases (small η_h and large η_h) in order to show the effect of the soil coefficient of subgrade reaction on the soil stiffness. For the coefficient of subgrade reaction with smaller value (η_h = 2 MN/m^3), the soil stiffness calculated using Equation (23) is as follows: The lateral soil stiffness K_{xx} is 2.25x10^8 N/m; the rotational soil stiffness $K_{\varphi\varphi}$ is 2.53x10^{10} Nm and the coupled soil stiffness $K_{x\varphi}$ is -2.25x10^9 N. For the coefficient of subgrade reaction with bigger value (η_h = 10 MN/m^3), the soil stiffness calculated using Equation (23) is as follows: The lateral soil stiffness K_{xx} is

$1.125x10^9$N/m; the rotational soil stiffness $K_{\varphi\varphi}$ is $1.266x10^{11}$ Nm and the coupled soil stiffness $K_{x\varphi}$ is $-1.125x10^{10}$ N.

Table 10 summarizes the foundation stiffness calculated in this chapter using the coupled spring model while considering both cohesive and cohesionless soil models. These values are used later on in chapter 6 as spring constants for the springs representing the seabed used as boundary conditions for the finite element modelling.

Table 10: Summary of the soil stiffness calculated using the coupled spring foundation model

Soil stiffness	Cohesive Model	Cohesionless Model (small η_h)	Cohesionless Model (big η_h)
Lateral soil stiffness (K_{xx} in N/m)	$1.337x10^9$	$2.250x10^8$	$1.125x10^9$
Rotational soil stiffness ($K_{\varphi\varphi}$ in Nm)	$1.003x10^{11}$	$2.530x10^{10}$	$1.266x10^{11}$
Coupled soil stiffness ($K_{x\varphi}$ in N)	$-1.003x10^{10}$	$-2.250x10^9$	$-1.125x10^{10}$

According to the sensitivity test run on the soil model for cohesionless soil (Appendix 4), the coefficient of subgrade reaction (η_h) is the most important soil parameter for the cohesionless model. As can be observed from Table 10, the soil stiffness calculated for cohesionless soil using different sources gave significantly different results which prove that indeed the coefficient of subgrade reaction can greatly affect the soil stiffness. Since the value for the coefficient of subgrade reaction for glacial till soil type seemed different from one source to another, emphasis was made on the result achieved using the cohesive model in chapter 6.The most important soil parameter (E_s) for the cohesive model could be found and the information seemed constant from one source to another. In other words, it was easier to find information on the elastic modulus of glacial till in the absence of site specific measurement. The final result of the lateral structural response obtained using both foundation models are compared in chapter 6.

5.4 Ice Load

The ice-load time series for intermittent ice crushing in Tahkoluoto (Figure 38) was modelled in this section in accordance with Figure 35. The maximum ice load was estimated using the Korzhavin equation (Equation (18)). The maximum load obtained was compared against the maximum ice load obtained from the reference simulation.

5.4.1 Ice properties

The ice thickness at tahkoluoto was estimated to be 0.6 m. The parameters used for the Korzhavin equation were selected according to IEC61400-3 as follows: The shape factor k_1 for circular structures is 0.9; The contact factor k_2 for ice contact against the support structure when the ice is continuously moving is 1.5; The ice crushing strength σ_c for ice in motion from wind and current at the coolest time of the year is 3 MPa; The indentation factor k_3 is 1.2 calculated according to Equation (24) with h the ice thickness (0.6m) and D is the pile diameter (6m) .

$$I = \sqrt{1 + 5h/D} \tag{24}$$

5.4.2 Result of Ice Load vs Reference Simulation

Figure 40 presents the ice load time series for intermittent ice crushing with maximum load defined using Korzhavin equation (Equation (18)) and the ice properties presented in the previous subsection (section 5.4.1). This ice load time series is used later on in chapter 6 as ice load input for finite element modelling. The frequency of the 5 MW baseline wind turbine considered is 0.3 Hz and the period used for the plot in Figure 40 is 3.33s.

In order to make sure that the ice load calculated and used in this thesis was close to the actual ice condition present in Tahkoluoto, the result of the ice load calculated was validated using the results obtained from previous simulations carried out by VTT at the Gulf of Bothnia. The result of the ice load calculated in this thesis was validated by comparing the maximum ice load obtained against the maximum ice load obtained from the previous simulation. Based on the parameters provided in section 5.4.1, the maximum horizontal ice load found was about 5832 kN as shown in the Figure 40.

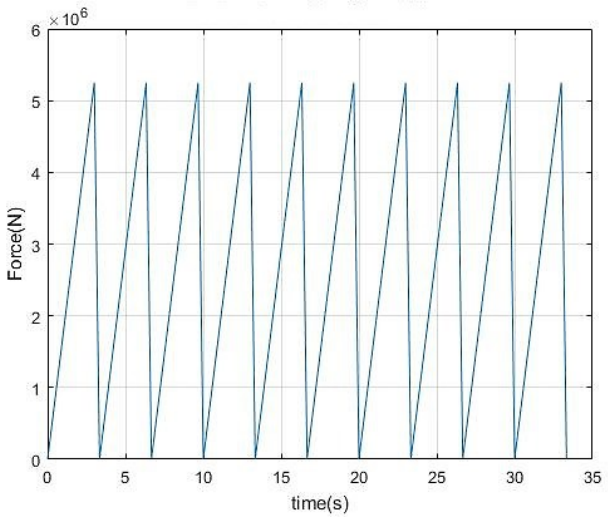

Figure 40: Ice load time series for intermittent ice crushing used as input ice load for finite element modelling in this thesis

The result of the previous simulation done by VTT presented in Figure 41 was produced using a different model but with similar parameters presented in section 5.4.1. The following parameters were used in the previous simulation: 0.6m for the ice thickness, 10m water depth and 6m monopile diameter. Continuous random crushing was assumed as the ice failure mechanism in this reference simulation. This simulation was done with FAST wind turbine simulation software by VTT and the dynamic ice load was evaluated using the Määttänen-Blenkarn model. With this model, the dynamic ice load is determine with a dependency on the ice conditions (ice thickness and velocity) and structure (dimensions and deflection). According to Figure 41, the maximum horizontal ice load obtained from the previous simulation was about 5000 kN which is close to the value of the horizontal ice load calculated in this thesis. [43]

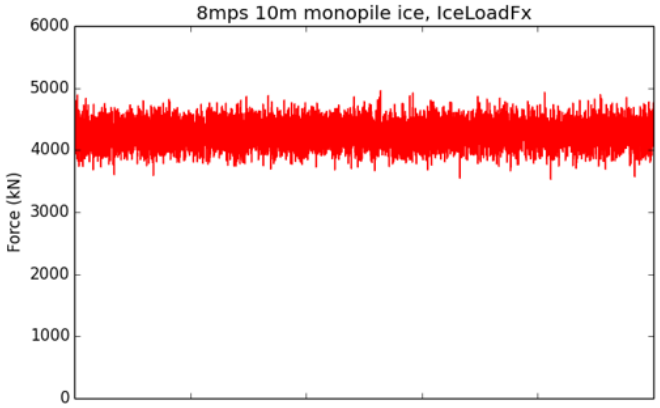

Figure 41: Horizontal ice load from previous simulations as a function of time; the x-axis is time that range from 100 to 150s with time increment of 10s [43]

5.5 Wave Load

The wave load is a dynamic load which is time dependent. Linear wave theory is assumed and the total wave force is found by integrating Morison's equation from the seabed to the mean water level. Therefore, to estimate the wave force in N, Equation (10) was integrated over the water depth considered to be 10 m (limit of integration: (water depth) $-10 \leq z_2 \leq 0$ (water surface or mean water level)). The wave properties used in Equation (10), (11a) and (11b) are presented in section 5.5.1. The wave load time series presented in this section is used as input wave load in chapter 6 for finite element modelling.

5.5.1 Wave properties

The wave properties in tahkoluoto and the parameters used to compute the wave load using Morrison's equation (Equation (10)) are the following: The water depth d_w is 10 m; The wave speed V_w is 8 m/s; The wave period T_w is 6.28s; The wave frequency f is 0.16 Hz; The wavelength $\lambda_{wave} = V_w / f = 50$ m; The wave height h_w is 1.41 m; The wave number $K = 2\pi/\lambda_{wave} = 0.13$ m^{-1}; The wave angular velocity $\omega = 2\pi f = 1.005$ rad/s; Monopile diameter D is 6 m; The drag coefficient for smooth tubular section C_d is 0.7; The density of sea water 1005 Kg/m^3; The time $0s \leq t \leq 31.4s$; The wave horizontal position $-31.4 \text{ m} \leq x \leq 0$ m (wave moves from the left to the right). The wave horizontal position was selected randomly to be in the same dimension as the time in order for the integration to be calculated easily using MatLab.

Generally, the mass coefficient C_m for smooth tubular section is 2. However, because the monopile diameter is large, the MacCamy-Fuchs correction factor must be incorporated into Morrison's equation to compensate for diffraction. The MacCamy-Fuchs correction factor is found using Figure 26 in section 4.1.2. The corrected inertia coefficient C_m is found by calculating $D/\lambda_{wave} = 0.12$ and selecting the corresponding mass coefficient from Figure 26. The corrected inertia coefficient C_m according to Figure 26 is 2.1. These parameters are similar to those used in the reference simulation which is used here to validate the maximum wave load calculated in this thesis.

5.5.2 Result of Wave Load vs Reference Simulation

Figure 42 shows the result of the wave load calculated by integrating Morrison's equation over the water depth using the wave properties presented in 5.5.1. The maximum wave load is about 324 kN. In other to validate the wave load calculated, the maximum wave load obtained was compared against the maximum load from previous simulation done by VTT using as case study the Gulf of Bothnia.

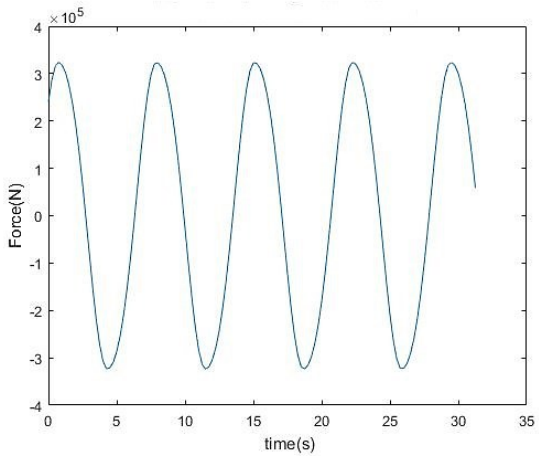

Figure 42: Wave load time series used as input wave load for finite element modelling in this thesis

The result presented in Figure 43 was achieved using similar wave properties presented in section 5.5.1. Some of the parameters used in the previous simulation are as follows: wave height h_w = 1.41 m; wave time period T_w = 6.28 s; water depth d_w = 10 m; wave mode 2. The wave load spectrum was evaluated in this reference simulation using the Pierson-Moskowitz model. The simulation was done using the HydroDyn which is a time-domain hydrodynamics module that is coupled into the FAST wind turbine computer-aided engineering software. The maximum wave load from the previous simulation used as reference is about 400 kN which is quite close to the wave load computed in this thesis. [43, 52]

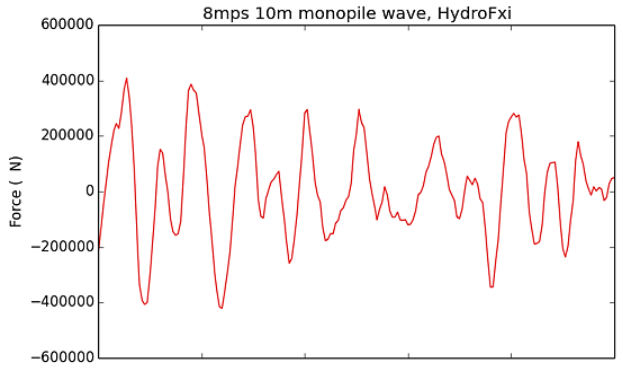

Figure 43: Wave load from previous simulations; the x-axis is time that range from 100 to 150s with time increment of 10s [43]

5.6 Extreme Operating Gust Wind Load

The dynamic effect of the wind load is evaluated in this thesis by assuming extreme operating gust wind load model. According to IEC61400-1, the wind speed for extreme operating gust is given by the equation

5.6.1 Wind properties

The wind properties and the parameters used to compute the wind load in Tahkoluoto are presented as follows: The reference wind speed V_w is 8.7 m/s; The power law coefficient α_{shear} is 0.12; The density of air ρ_a is 1.23 kg/m^3 at 15 ºC at 1 atm; The thrust coefficient $C_T(\lambda s)$ is 0.7 for a tubular tower; The rotor diameter is 130 m; The diameter of the tower D is 3.87 m; The height coefficient C_h is 1.58; The shape coefficient for cylindrical structure C_s is 0.5. The reference wind speed is considered here as the wind speed at the hub height. The power law coefficient is used as recommended by IEC61400-1. [18, 19, 27, 44]

5.6.2 Wind Load on the Turbine Blades

The wind load at the blades centered at the hub and the wind load on the turbine tower have the same spectrum reasons why only the blade wind load at the hub is presented here since it is the also the most critical. The maximum blade wind load at the hub based on the extreme operating gust model is about 1620583 N (1621 KN) as shown in Figure 44.

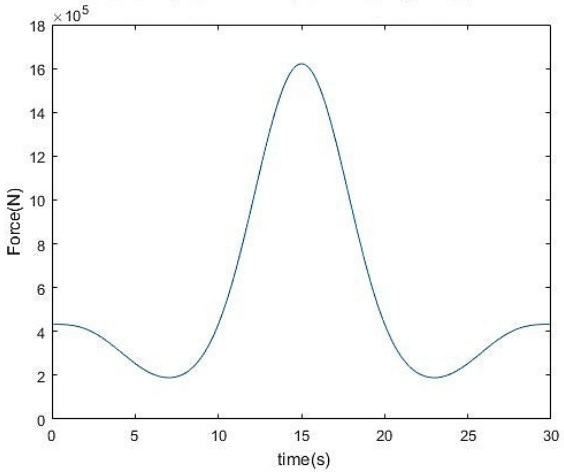

Figure 44: Time series of the blade load at the hub for a period of 30s used as input wind load for finite element modelling in this thesis

A summary of the loads calculated in this thesis is presented in Table 11. As can be observed the wave and ice loads calculated in this thesis are closed to those obtained from the previous simulation done in VTT using the Gulf of Bothnia as case study. No wind load data was obtained from the previous simulations thus, only the ice and wave loads have been validated. The slight difference may be due to the different models used which incorporated slightly different parameters. For example, the ice load model (Määttänen-Blenkarn model) used in the previous simulation incorporated ice velocity in order to evaluate the maximum ice load which was not considered in the Korzhavin equation used in this thesis.

Table 11: Summary of loads calculated

Maximum load	Thesis (kN)	Previous simulation (kN)
Ice load	5832	5000
Wave load	324	400
Wind load at the blade	1621	-

6 Finite Element Modelling

This chapter presents the result of the lateral structural response under dynamic single and combined loads. In addition, it presents the result of the Eigenfrequency analysis carried out during this project using Abaqus. Figure 45 shows a sketch of the 5 MW baseline wind turbine modelled in Abaqus. The turbine was modelled in Abaqus as a 2D deformable beam with boundary conditions consisting of a set of springs connected to the to the monopile foundation at mudline as shown in Figure 45. The spring stiffness in Table 10 calculated earlier in chapter 5 were used as the spring constants for the springs in Figure 45. Only the lateral response of the structure was evaluated in this thesis. The vertical displacement of the turbine was considered fixed since the stiffness of the vertical soil spring was unknown and out of interest in this thesis. The embedded monopile length was ignored. The nacelle-rotor assembly was modelled as a point mass (Figure 45). The 2D beam element was sectioned into 17 finite elements join together by nodal points in Abaqus. Node 1 was used to evaluate the lateral behaviour of the monopile at the seabed while node 18 was used for the tower top. These two nodes were the focus, during the dynamic analysis. The global coordinate considered was as shown in Figure 45. The result of the structural response obtained using the cohesive foundation model is presented in this chapter while that which was obtained using the cohesionless foundation model is presented in Appendix 3. This is due to the reasons mentioned in section 5.3 and because the first natural frequency found whilst considering the cohesive model was also quite close to the actual natural frequency of the system.

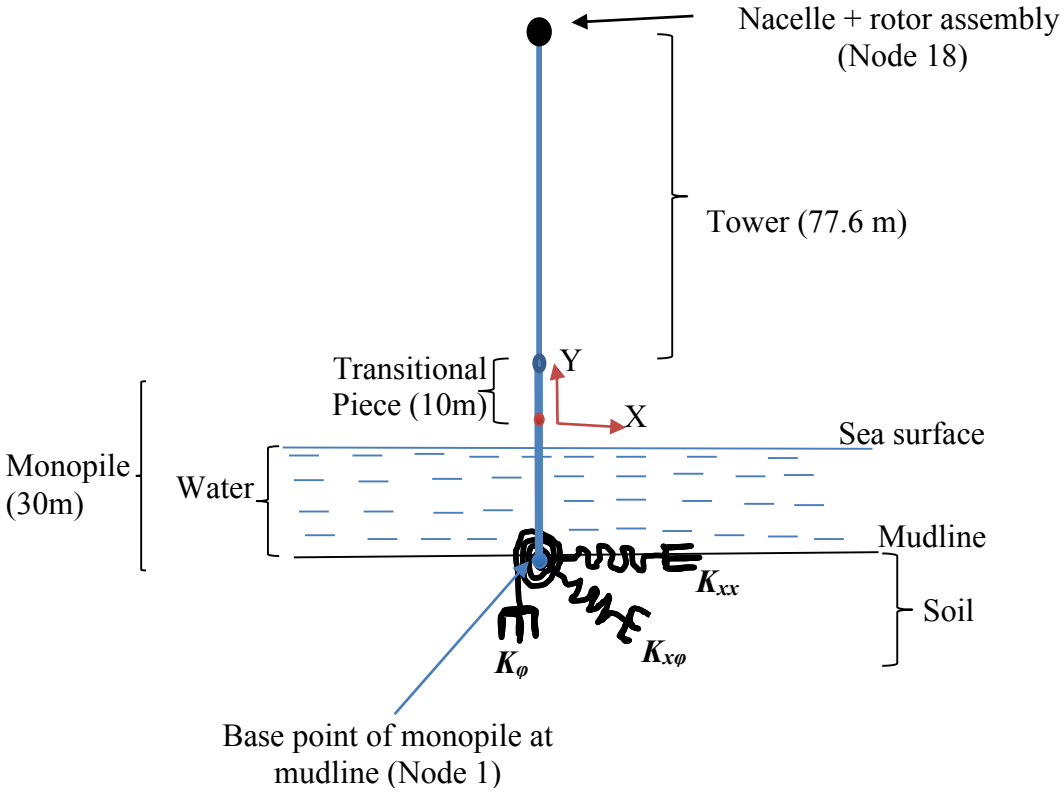

Figure 45: Schematic illustration of modelled 5-MW Baseline wind turbine

The coupled spring foundation model was modelled in Abaqus such that the lateral and rotational springs were computed using springs (connected to the ground) in direction 1 (x-direction) and 6 (rotation around z-direction) found in Abaqus. However, there was no direct

means of computing the coupling term of the coupled spring model in Abaqus so, the coupling term was modelled using basic connector element. The connector element had the following properties based on the features found in Abaqus: Axial translation and rotation connection types; Coupled linear elastic behaviour. The foundation stiffness calculated was used as the constants of elasticity.

6.1 EigenFrequency

The fundamental frequency of the system was determined using Eigenfrequency analysis. The first natural frequencies of the structure using cohesive and cohesionless soil models are presented in this section in Table 12. The structural response of the free vibration is also presented in Table 12. As can be observed from Table 12, the first natural frequency obtained while considering the cohesive model and the cohesionless model with bigger coefficient of subgrade reaction (η_h) are quite close to the actual natural frequency of the 5 MW baseline wind turbine modelled during this project. In addition, they give almost same result for the maximum lateral displacement of the free vibration at mudline and at the tower top.

Table 12: Result of the first natural frequency

Models	First natural frequency (Hz)	Maximum lateral displacement of the free vibration at mudline (m)	Maximum lateral displacement of the free vibration at tower top (m)
5 MW Baseline Wind Turbine	0.3	-	-
Cohesive Model	0.25	0.7	1
Cohesionless Model (small η_h)	0.22	0.88	1
Cohesionless Model (big η_h)	0.25	0.7	1

6.2 Lateral Structural Response

In this section, the result of the lateral displacement of the 5MW baseline wind turbine under dynamic ice, wave and wind loads (applied seperately) simulated for a time period of 31.5s is presented. The loads calculated in chapter 5 are used here as input loads. The spring stiffness calculated using the cohesive soil model earlier is used as boundary conditions for this analysis.

The result of the lateral response of the turbine under wave load is presented in Figure 46, 47 and 48. In Figure 46, the lateral response of all the nodes at 31.5 seconds is shown. The blue colour (at the bottom) represents the support structure and the red represents the tower top. The maximum lateral displacement is at the tower top as can be observed in Figure 46. The lateral displacement at the mudline is shown in Figure 47. The maximum displacement of the substructure (monopile) at the seabed under wave load is about 0.16 mm. The maximum lateral turbine displacement is at the turbine top. The maximum lateral displacement of the tower top is about 12 mm as shown in Figure 48.

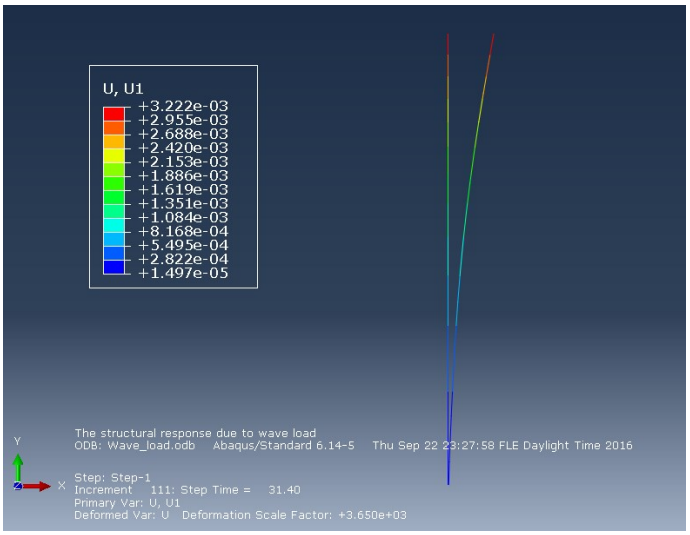

Figure 46: Structural response under wave load; U1 is the lateral displacement of the baseline offshore wind turbine

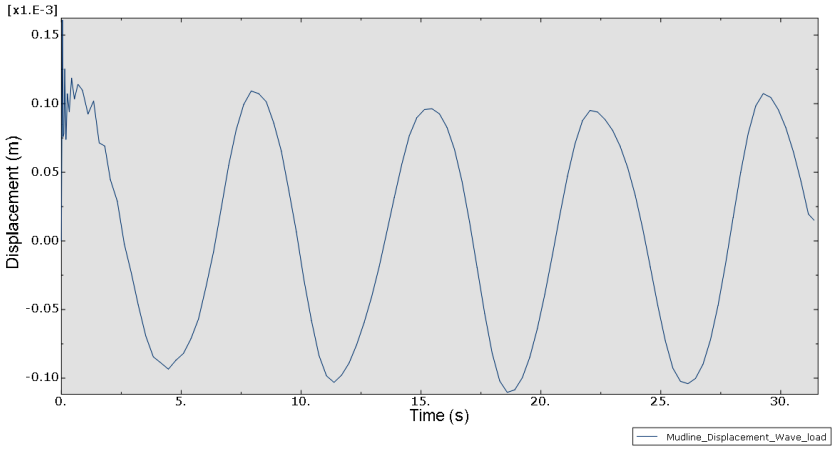

Figure 47: Lateral displacement of the baseline offshore wind turbine at the mudline

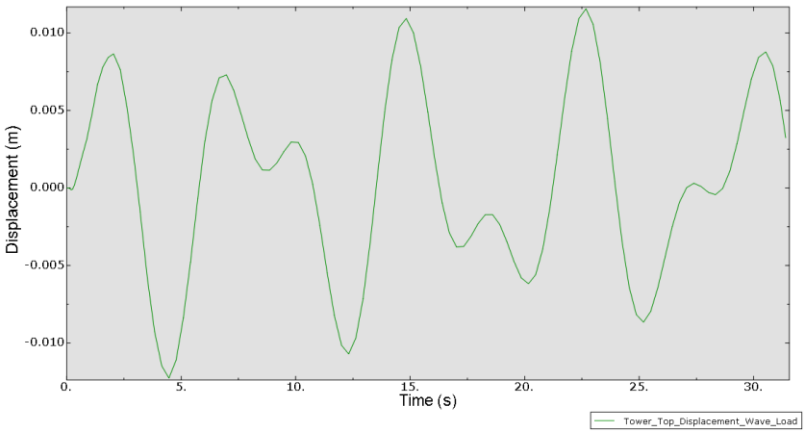

Figure 48: Lateral displacement at the tower top of the baseline offshore wind turbine

The result of the lateral response of the turbine under dynamic ice load is presented in Figure 49, 50 and 51. The lateral displacement of all the nodes at 30 seconds is shown in Figure 49. The yellowish-brown colour (at the bottom) represents the support structure and the blue represents the tower top. The maximum lateral displacement is at the tower top as can be

observed in Figure 49. The lateral displacement at the mudline is shown in Figure 50. The maximum displacement of the substructure at the seabed under ice load is about 2 mm. The maximum lateral turbine displacement is at the tower top and it is about 136 mm as shown in Figure 51.

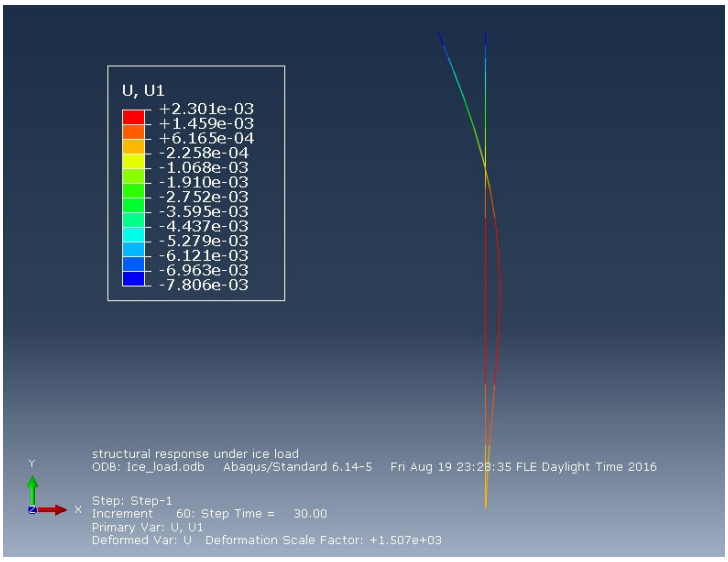

Figure 49: Structural response under Ice load; U1 is the lateral displacement of the baseline offshore wind turbine

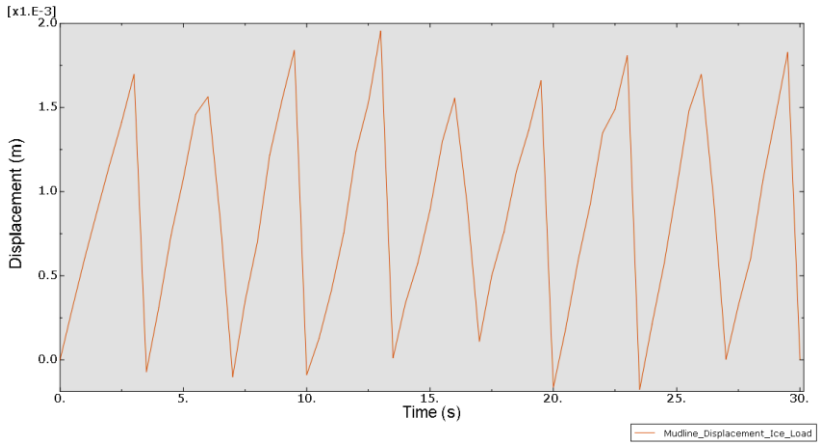

Figure 50: Lateral displacement at mudline of the baseline offshore wind turbine

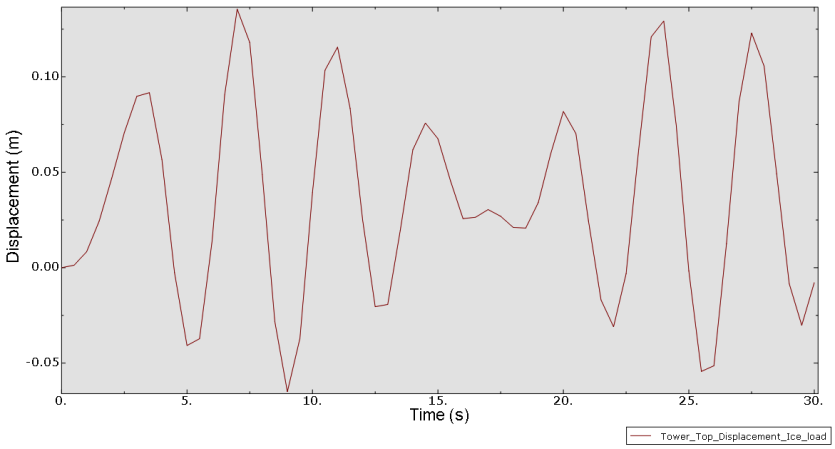

Figure 51: Lateral displacement at the tower top of the baseline offshore wind turbine

The wind load was modelled in Abaqus as a line load whereby the power law wind profile model was used to describe the variation of the wind as a function of the tower height as shown in Figure 52. The result of the lateral response of the turbine under extreme operating gust wind load is presented in Figure 53, 54 and 55. The lateral displacement of all the nodes at 30 seconds is shown in Figure 53. The blue colour (at the bottom) represents the support structure and the red represents the tower top. The lateral displacement at the mudline is shown in Figure 54. The maximum displacement of the substructure at the seabed under wind load is about 4 mm. The maximum lateral turbine at the tower top is about 2072 mm as shown in Figure 55.

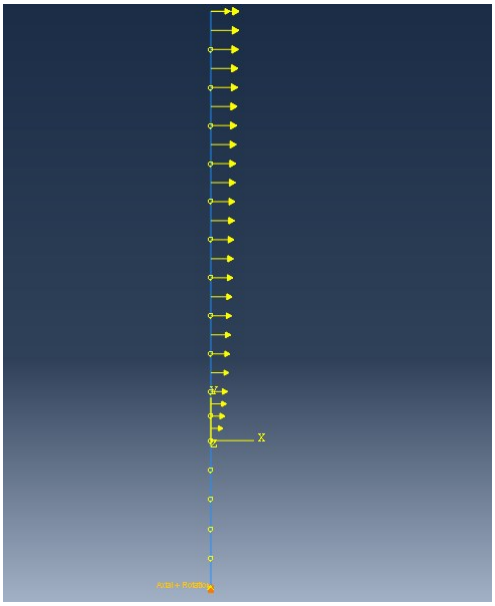

Figure 52: Abaqus model of the baseline wind turbine under wind load

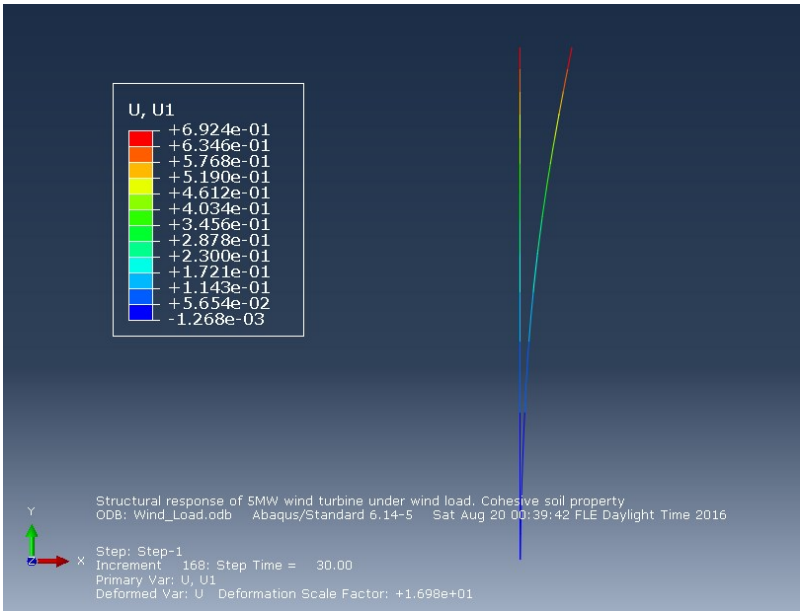

Figure 53: Structural response under extreme gust wind load; U1 is the lateral displacement of the baseline offshore wind turbine

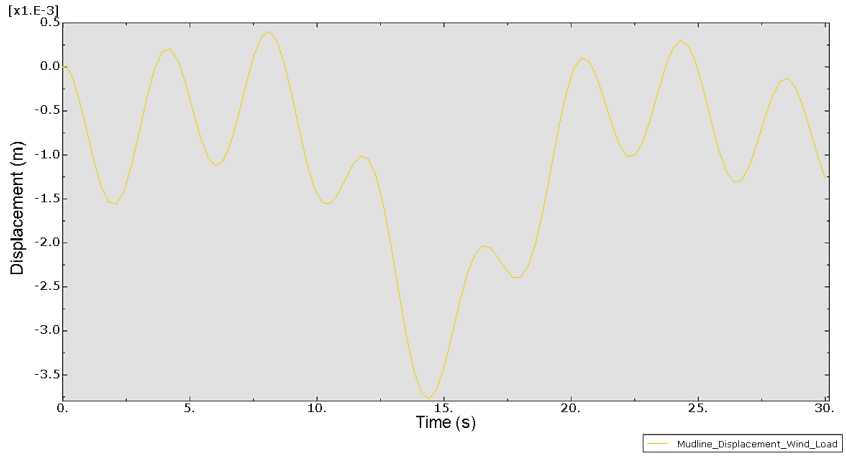

Figure 54: Lateral displacement at mudline of the baseline offshore wind turbine

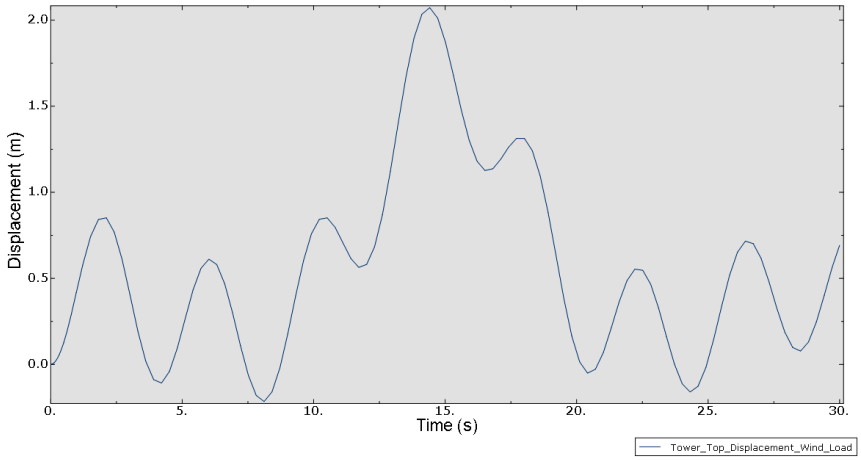

Figure 55: Lateral displacement at the tower top of the baseline offshore wind turbine

6.3 Design Load Cases

To model the effect of combined loads on the structural response of offshore wind turbines, two design load cases were selected according to IEC 61400-1: Design load case 3.2 for start-up and design load case E3 for power production design situations. Combined loads refers to two different kind of loads applied simultaneously in the same simulation. The results from both design load cases simulated for a period of 30 seconds are discussed in this section. [44]

6.3.1 Start-up: Design Load Case 3.2

This design load case describes a design situation whereby a wind turbine is under combined wave and wind loads during the transients from any standstill or idling situation to power production. The result of the turbine lateral response under combined wave and wind loads is presented in this section. According to this design load case, both loads are co-directional and unidirectional. The extreme operating gust wind load and the wave load models used in chapter 5 are used here to calculate the loads but with slightly different parameters selected according to IEC 61400-1. [44]

The wind speed at the hub is the reference speed $V_{w,r} \pm 2$ m/s thus, the wind speed at the hub considered for this design load case is 10.7 m/s (Section 5.6) while the wave height h_w is found as a function of the wind speed as described by Simo Rissanen and Jaakko Heinonen (2016) [43]. The wave height of a wind speed of 10.7 m/s is about 2 m. The maximum wave load calculated earlier in section 5.5 increased in this case to about 42% (459 kN) due to the increase in wave height. In addition, the maximum wind load at the hub calculated in section 5.6 increased in this case to about 47% (2380 kN) due to the change in reference speed. [44]

Figure 56 shows the nodal displacements of the 5-MW baseline wind turbine under combined extreme operating gust wind load and wave load. In the legend in Figure 56, U:U1 refers to the displacement in the x-direction (lateral displacement), Part-1-1 refers to the turbine and N refers to the nodes. N:1 or node 1 is refers to the nodal point at the seabed. N:1 to N:8 are nodes in the support structure while N:8 to N:18 are nodes in the tower. Node 18 is used for the tower top. The maximum turbine lateral response at the seabed for a period of about 30s under combined extreme operating gust wind load and wave load is about 5.5 mm. The maximum lateral displacement at the tower top is about 3074 mm while the maximum displacement at the support structure is about 332 mm.

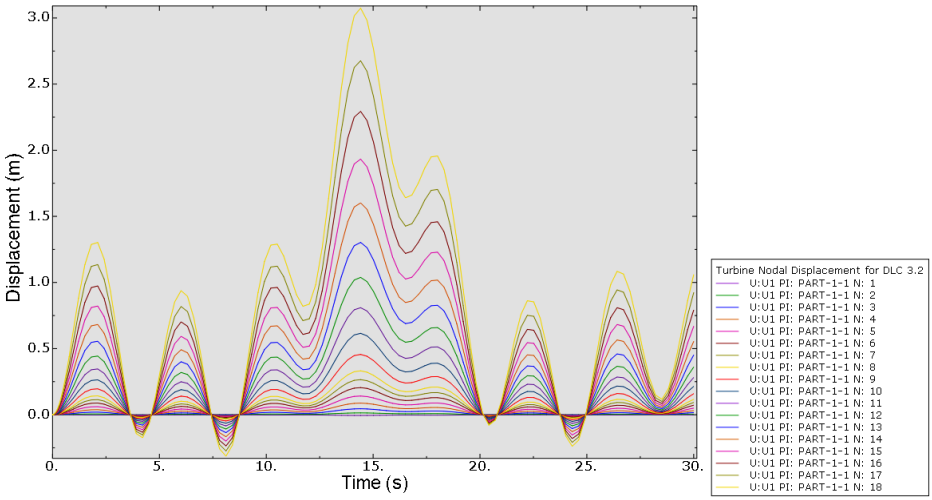

Figure 56: Nodal lateral displacement of the 5-MW wind turbine for design load case 32; U1 is the lateral displacement, part-1-1 is part number of the model in Abaqus and N:1 to18 represent the node numbers

6.3.2 Power Production Design Situations: Design Load Case E3

This design load case describes a design situation whereby a wind turbine is under combined ice and wind loads during power production. The result of the turbine's response under the combination of ice and wind load according to the design load case E3 by IEC61400-3 is presented in this section. The wind load in this design load case was evaluated using the normal turbulence model (NTM). The maximum ice load was described using the Korzhavin model as calculated in Section 5.4 but with slightly different parameters. The ice thickness used here is that with a 50 year recurrence (0.8 m) and wind speed at the hub used is 10.7 m/s ($V_{w,r} \pm 2$). The ice compressive stress used was from a VTT document (4.8MPa). Given the above mentioned new parameters, the maximum ice load calculated in section 5.4 increased to about 62% (9435 kN).[44] In the normal turbulence model for the wind load, the

wind load is evaluated using Equation (13), (14), (15b) and (16) with the turbulence standard deviation σ calculated by the equation below.

$$\sigma = I_{ref}(0.75V_{hub} + b) \tag{25}$$

Where I_{ref} is the expected value of the hub-height turbulence intensity at 15 m/s; V_{hub} is the wind speed at the hub and b = 5.6 m/s. The turbulence intensity I_{ref} was found using Figure 30 and the reference wind speed. Considering the GL offshore curve and a mean speed of 15 m/s (wind speed at the hub) in Figure 30, the turbulence intensity was about 20% thus I_{ref} used was 0.2. The maximum normal turbulence wind load at the hub calculated was about 1075 N. This value is quite small compared to the maximum wind load calculated using the extreme operating gust model in section 5.6 (1621 kN). Since in this design load case, the direction of the loads is not specified, both cases of when the loads are co-directional and when they are applied to opposite direction are evaluated. [44]

When the loads are co-directional, the maximum turbine lateral response at the seabed for a period of 30 seconds under combine dynamic ice load and normal turbulence wind load is about 4.4 mm. The maximum lateral displacement at the turbine top is about 313 mm while the maximum displacement at the support structure is about 71 mm. Figure 57 shows the lateral nodal displacement of the 5-MW baseline wind turbine under combine dynamic ice load and normal turbulence wind load with the loads applied to the same direction. The definition of the node numbers in Figure 57 is the same as already explained in section 6.3.1.

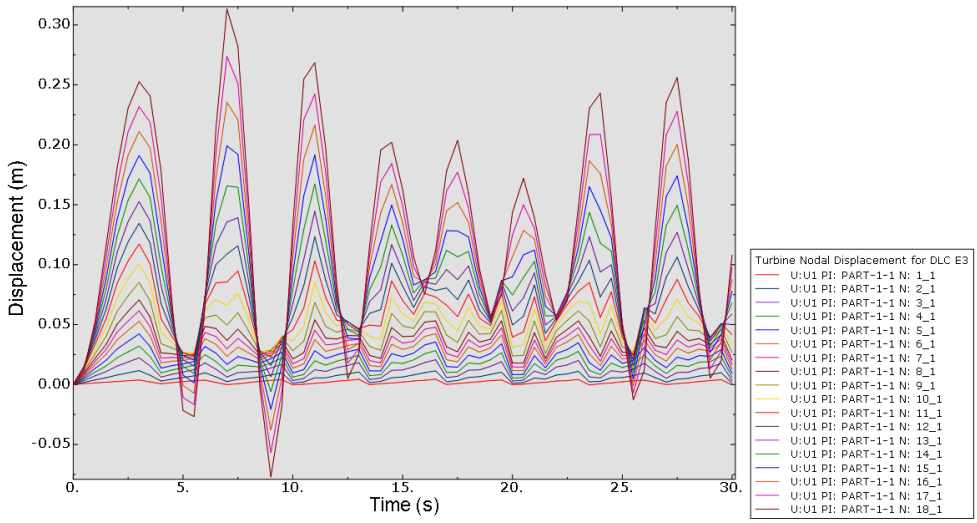

Figure 57: Nodal lateral displacement of 5-MW wind turbine for design load case E3 when the loads are co-directional; U1 is the lateral displacement, part-1-1 is part number of the model in Abaqus and N:1 to18 represent the node numbers

When the loads are applied to opposite-direction, the maximum turbine lateral response at the seabed for a period of 30 seconds under combine dynamic ice load and normal turbulence wind load is about 4.5 mm. The maximum lateral displacement at the turbine top is about 223 mm while the maximum displacement at the support structure is about 58 mm. Figure 58 shows the lateral nodal displacements of the turbine under combined dynamic ice load and normal turbulence wind load when the loads are applied to opposite directions.

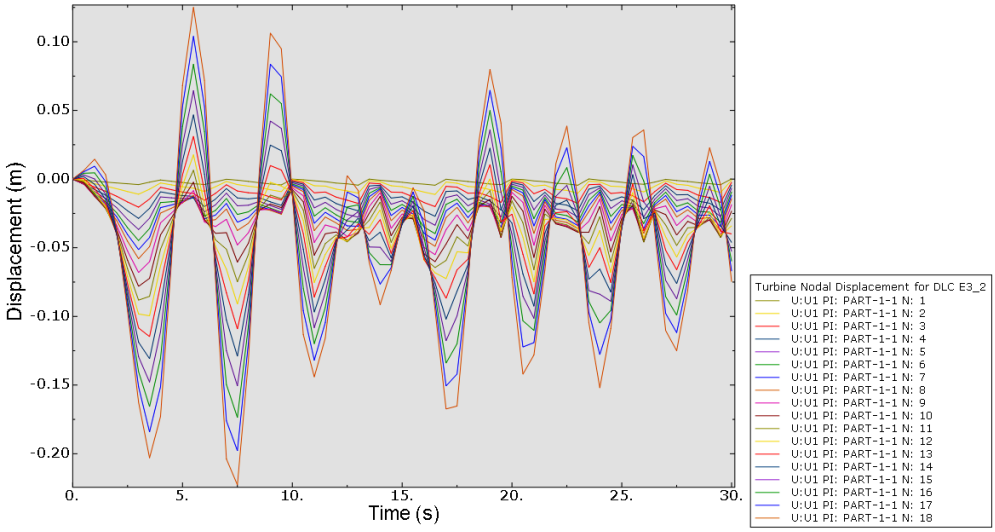

Figure 58: Nodal lateral displacement of 5-MW wind turbine for design load case E3 when the loads are in opposite direction; U1 is the lateral displacement, part-1-1 is part number of the model in Abaqus and N:1 to18 represent the node numbers

6.4 Summary and Analysis of Results

Table 13 summarizes the result of the lateral response of the 5 MW baseline wind turbine under dynamic ice, wave and wind load (applied separately) investigated in this thesis using the environmental conditions present in Tahkoluoto (Gulf of bothnia) and the cohesive foundation model. Table 14 summarizes the results of the lateral structural response under dynamic ice, wind and wave loads (applied separately) whilst considering the cohesionless foundation model. The results in Table 14 are explained in detail in Appendix 3. The structural response in Table 14 are obtained using the smallest foundation stiffness calculated using the cohesionless model in chapter 5.

Table 13: Summary of the lateral structural response under individual loads obtained using the cohesive foundation model

Load Types	Maximum Displacement at Seabed (mm)	Maximum Displacement at Tower Top (mm)	Maximum Displacement of the support structure (mm)
Ice	2	136	28
Wave	0.2	12	3
Wind	4	2072	223

Table 14: Summary of the lateral structural response under individual loads obtained using the cohesionless foundation model

Load Types	Maximum Displacement at Seabed (mm)	Maximum Displacement at Tower Top (mm)	Maximum Displacement of the support structure (mm)
Ice	13	247	65
Wave	1	29	7
Wind	20	2580	379

Table 15 summarizes the result of the lateral response of the baseline turbine under combined ice, wind and wave loads presented in section 6.3. Table 16 summarizes the structural response of the 5-MW baseline wind turbine under combined loads according to design load case 32 and E3 using the cohesionless foundation model. Appendix 3 provides details on the structural response using the cohesionless foundation model.

Table 15: Summary of lateral structural response under combined loads obtained using cohesive foundation model

Design Load Case (DLC)	Models	Maximum Lateral Displacement at Mudline (mm)	Maximum Lateral Displacement at Tower Top (mm)	Maximum Lateral Displacement of Support Structure (mm)
DLC 3.2: Start-up	-**Wind:** Extreme Operating Gust (EOG) -**Wave:** Morrison	5.5	3074	332
DLC E3: Power production Design Situation (Co-directional loads)	-**Wind:** Normal Turbulence Model (NTM) -**Ice:** Korzhavin	4.4	313	71
DLC E3: Power production Design Situation (opposite-direction loads)	-**Wind:** Normal Turbulence Model (NTM) -**Ice:** Korzhavin	4.5	223	58

Table 16: Summary of lateral structural response under combined loads using cohesionless foundation model

Design Load Case (DLC)	Models	Maximum Lateral Displacement at Mudline (mm)	Maximum Lateral Displacement at Tower Top (mm)	Maximum Lateral Displacement of Support Structure (mm)
DLC 3.2: Start-up	-**Wind:** Extreme Operating Gust (EOG) -**Wave:** Morrison	29	3844	568
DLC E3: Power production Design Situation (Co-directional loads)	-**Wind:** Normal Turbulence Model -**Ice:** Korzhavin	30	700	164
DLC E3: Power production Design Situation (opposite-direction loads)	-**Wind:** Normal Turbulence Model (NTM) -**Ice:** Korzhavin	31	610	147

It can be concluded from both results in Table 13 and Table 14 that the turbine response under dynamic ice load and extreme gust wind load is considerably higher compared to when the structure is under wave load. The wind load seems to have a dominant effect on the structural response in this case study. Extreme operating gust wind load which is generally for a short period of time leads to quite high structural response. According to the results provided in Table 15 and Table 16, the structural response under combined extreme operating gust wind load and wave load is extremely high especially at the tower top. These results show the dependency of the structural response on the load. In addition, these results show that the maximum lateral displacement of the turbine is at the tower top.

In this study the lateral response of the wind turbine when combined loads are applied, according to the design load cases selected, is greater than its lateral response when wind, wave and ice loads are applied individually. This is a clear illustration of the fact that when two or more loads are applied simultaneously in the same direction, the magnitude of the resultant force is the sum of the magnitudes of applied forces which of course will lead to higher structural response. It can also be observed from Table 13, Table 14, Table 15 and Table 16 that the results of the turbine's response when the loads are combined is different to the result obtained summing together the turbine's responses when wave, wind and ice loads are applied separately. This is due to the change in the load magnitudes in the design load cases which was as a result of the change in the load parameters such as ice thickness, ice crushing strength, wave height and wind speed as illustrated in section 6.3. For example, the result of the design load case 3.2 in this thesis is greater than summing together the results of the structural response when wind and wave loads are applied separately because the maximum wind and wave loads increased due to the increased in wave height and mean wind speed. However in the design load case E3, the maximum ice load increased to about 62% (due to ice thickness and ice crushing strength) while the wind load reduced drastically due to the different wind model and the wind situation considered.

The results achieved using the cohesive soil model are quite different from those obtained using the cohesionless soil model with smaller soil stiffness as can be seen from Table 13, Table 14, Table 15 and Table 16. This is due to the different soil stiffness obtained using both models. Because the smaller soil stiffness of the cohesionless soil model was about four times smaller than the soil stiffness of the cohesive model, the effect of foundation stiffness on the lateral response of an offshore wind turbine could easily be observed. This huge difference in the soil stiffness showed clearly the effect of soil-monopile interaction on the structural response of the baseline turbine as illustrated in Table 13, Table 14, Table 15 and Table 16. This therefore proves that the strength of the connection between monopile and the soil has an effect on the structural response. In other words, the soil-structure interaction must be considered when evaluating the structural response of monopile offshore wind turbines.

6.5 Effect of Load Parameters on the Structural Response

Ice thickness, wind speed and wave height used to evaluate the applied loads used in the finite element modelling were varied during this work as illustrated in section 6.3. The wind,

wave and ice loads that were applied separately to the turbine model were evaluated using similar load parameters that have been used in reference simulation. The parameters proposed by IEC 61400-1 were used to evaluate the combined loads. Figure 59 and Figure 60 are plotted in order to demonstrate clearly the effect of ice thickness, wind speed and wave height on the structural response. Figure 59 is plotted by varying ice thickness and wind speed. The structural response when ice load is applied and when ice and wind loads are applied simultaneously is presented in Figure 59. The results show that ice load and ice-induced response are strongly dependent on ice thickness while wind load and wind-induced response are strongly dependent on the mean wind speed. The structural response as a function wave height when wave load is applied is shown in Figure 60. These results show the dependency of the structural response on load parameters such as ice thickness, wind speed and wave height.

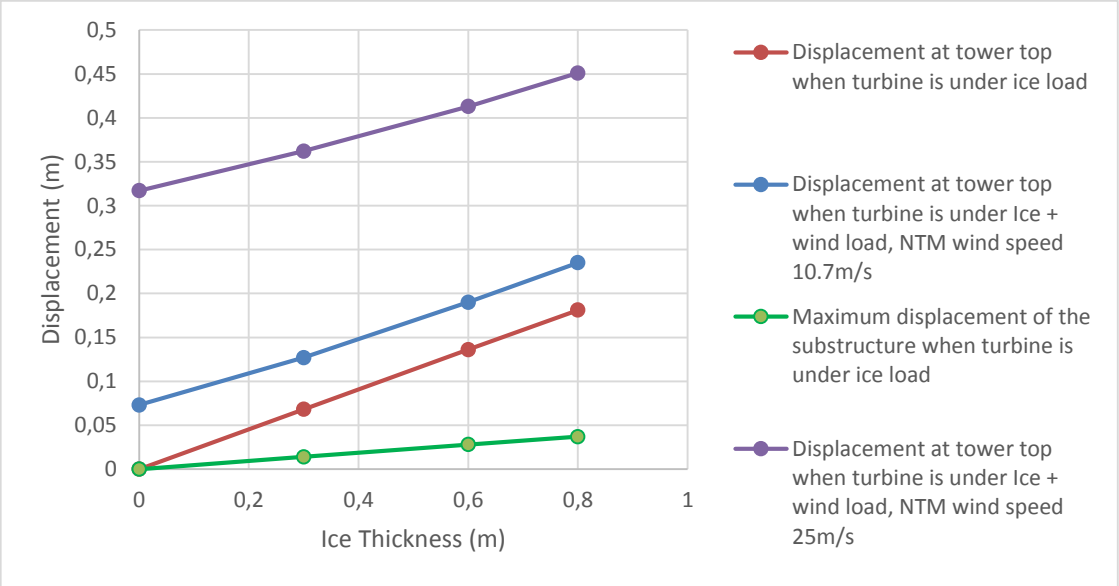

Figure 59: Effect of ice thickness and wind speed on the lateral response of the 5-MW baseline offshore wind turbine

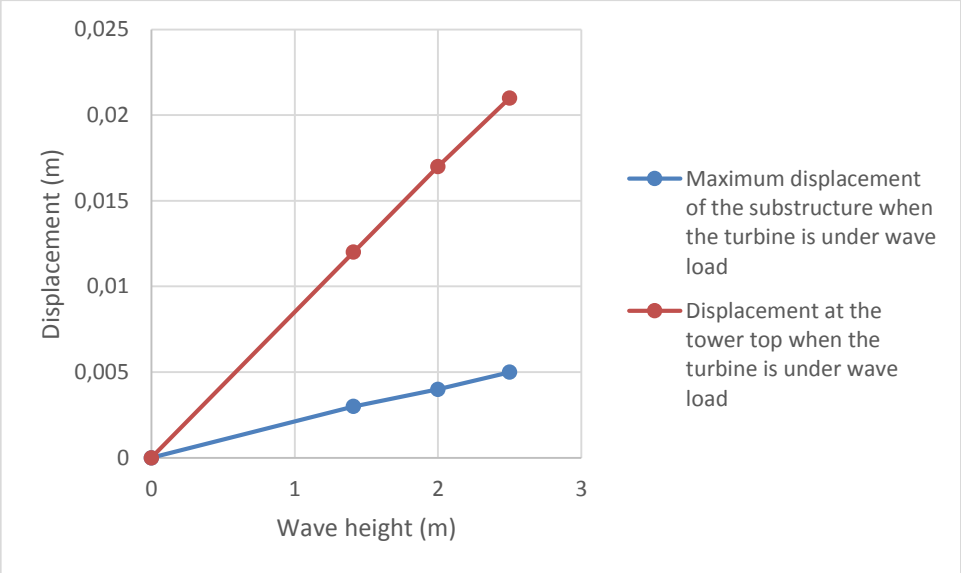

Figure 60: Effect of wave height on the lateral structural response the 5-MW baseline offshore wind turbine

6.6 Validation of Results

The result of the structural response using the coupled spring foundation model is validated in this subsection. The validation is done by comparing the result of the lateral response of the turbine under ice and wave loads (applied separately) to the result obtained for the same turbine under similar loading condition using FAST in a previous simulation done by VTT. FAST (Fatigue, Aerodynamics, Structure and Turbulence) is an engineering software used for simulating the coupled dynamic response of wind turbines. In FAST there are different modules for the soil and the loads but these modules are difficult to combine. So the soil-monopile interaction was not taken into account in the previous simulation done using FAST. Abaqus was used in this thesis so that the soil-structure interaction will be taken into account. In this subsection, only the result of the lateral response of the turbine when ice and wave loads are applied are validated. This is because only these two cases were modelled in the previous simulation. Nevertheless the validation of both cases may give an overview of the turbine's response given the coupled spring foundation model and the load models. [52]

In the previous or reference simulation, the whole turbine system (blades-nacelle assembly, tower, support structure) was modelled with the substructure fixed to the ground. In other words, the monopile was considered fixed at the seabed. The turbine specification used in the reference simulation is same as presented in Table 8. The water depth was also 10 m. The ice load used in the reference simulation to obtain the result presented in Figure 62 is described in section 5.4.2 and presented in Figure 41. The wave load used in the reference simulation to achieve the result presented in Figure 64 is explained in section 5.5.2 and illustrated in Figure 43. The results are analyzed for a time range of 100-150s. Figure 61 shows the lateral tower base displacement under dynamic ice load obtained in this thesis while Figure 62 shows the lateral tower base displacement obtained in the previous simulation. In addition, Figure 63 shows the lateral tower base displacement under wave load obtained in this thesis while Figure 64 shows the lateral tower base displacement obtained in the previous simulation. Tower base displacement refers to the displacement of the end of the tower connected to the support structure. [52]

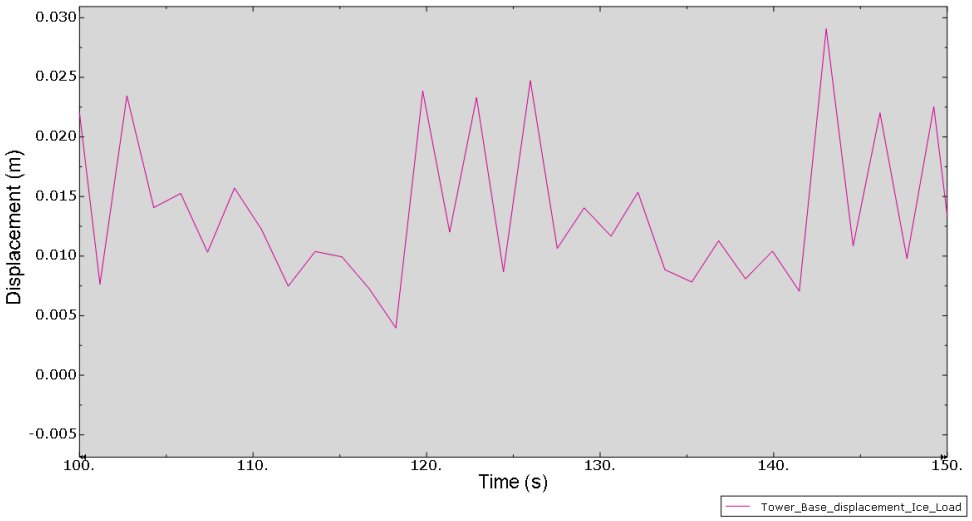

Figure 61: Lateral displacement of tower base of the baseline turbine under dynamic ice load

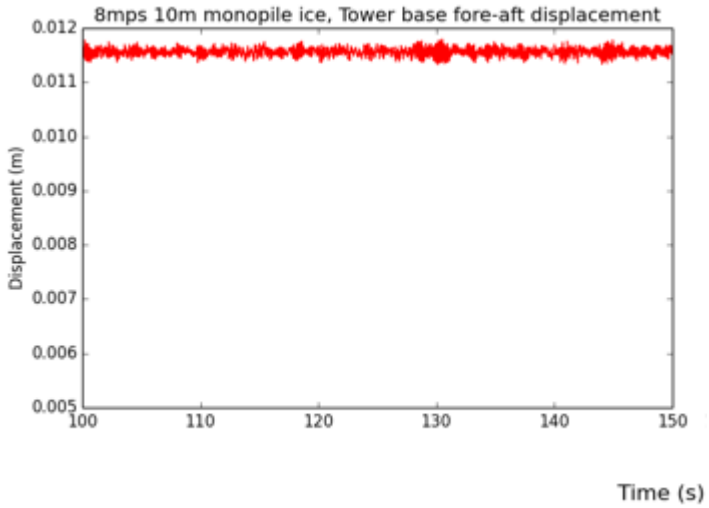

Figure 62: Lateral tower base displacement under ice load obtained from FAST software in a previous simulation; wind speed 8m/s, 10m water depth [43]

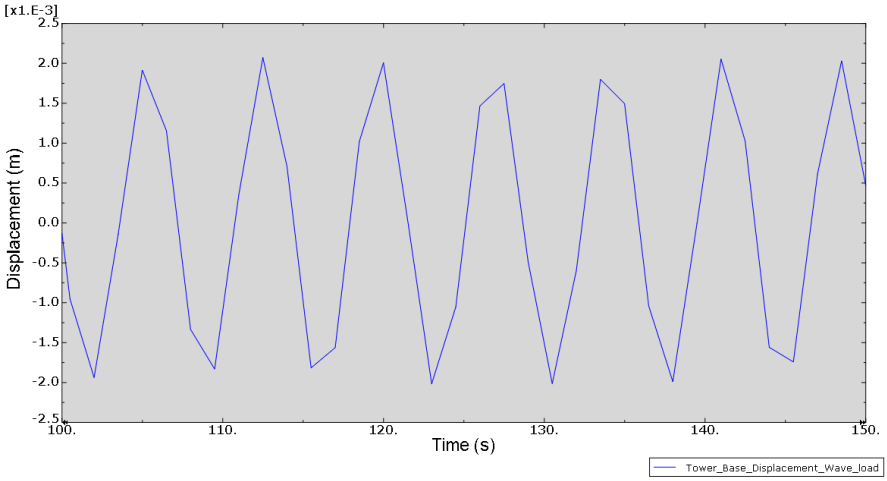

Figure 63: Lateral tower base displacement of the baseline offshore wind turbine under wave load

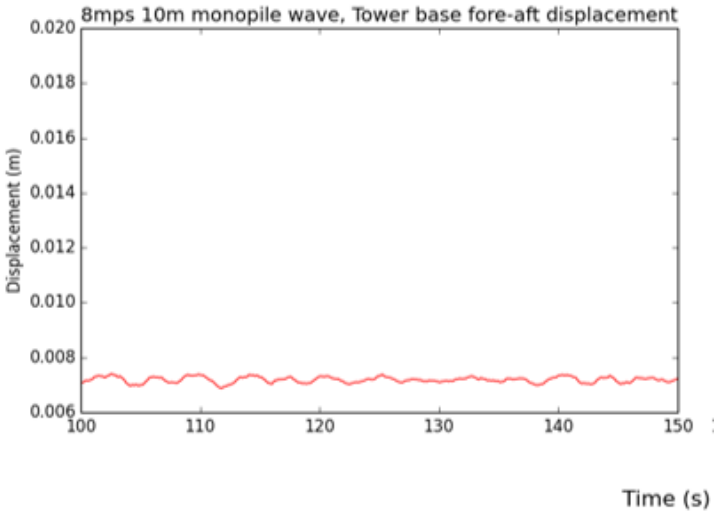

Figure 64: Lateral tower base displacement under wave load obtained from FAST software in a previous simulation wind speed 8m/s, 10m water depth [43]

The maximum tower base displacement under dynamic ice load for the given time range evaluated in this thesis is about 0.029m as shown in Figure 61 while that of the reference simulation is about 0.012m. It should be reminded that the maximum ice load used in this thesis to obtain the result shown in Figure 61 was about 16.6% higher than the maximum ice load used in the reference simulation (section 5.4). The tower base displacement obtained in this thesis is about 2.4 times higher than that which was obtained in the previous simulation. Furthermore, it should be reminded that the maximum wave load used in the reference simulation was about 23.5% higher than that which was used to obtain the result in Figure 63. The maximum lateral tower base displacement obtained in this thesis is about 0.002m as shown in Figure 63 while that which was obtained in the reference simulation is about 0.007m.

In the case of the ice load, the result seems somewhat reasonable as the higher displacement obtained in this thesis may be due to the fact that the soil-monopile interaction was accounted for. In addition, it may be due to the particular foundation model used and the soil stiffness used. As illustrated earlier, the foundation stiffness has a significant effect on the structural response. Furthermore, the higher displacement may be due to how the foundation model used was modelled. It should be recalled that the coupling term of the coupled spring foundation model was modelled using connector element in Abaqus. This may also have an effect on the structural response. In the case of the wave load, one would expect higher response from the thesis result (or closer result to that of the reference simulation) even though the simulation maximum wave load was about 1.2 times higher. This expectation is due to the flexibility of the foundation springs used in the modelling as boundary conditions in order to idealize the soil-monopile interaction which was not considered in the reference simulation (fixed boundary conditions at seabed in the reference simulation). Apart from the foundation model, this result may also be due to difference in wave spectrum used or the wave load models. Overall, the result of the structural response obtained in this thesis is in the same dimension as that of the reference simulation. Therefore, revising the modelling of the coupling term of the coupled spring model or the coupled spring foundation model itself or the load models may lead to more promising result. It should be recalled that only the foundation stiffness at seabed was modelled using the coupled spring foundation model while the in-depth soil and the embedded length of monopile was ignored. However, the coupled spring foundation model could have also been modelled in such way that the in-depth soil foundation stiffness might have also been taken into account.

7 Conclusion

This thesis focused on the modelling of the structural response of monopile offshore wind turbines installed in ice-covered seas taking into account the soil-monopile interaction. The lateral displacement of a 5-MW baseline wind turbine under dynamic ice, wind and wave loads applied separately (single loads per analysis) was evaluated in this work. The single loads were estimated using Tahkoluoto's (Gulf of Bothnia) environmental conditions. The result of the simulation (with single loads) was validated using the results from a previous simulation (reference simulation) run on the same turbine with similar loading conditions. In addition, the lateral structural response under two different kind of loads applied simultaneously according to the design load cases 3.2 and E3 proposed by IEC 61400-1 was evaluated. The coupled spring foundation model was used to idealize the soil-monopile interaction as a set of springs (used as boundary conditions) in the finite element modelling. To compute the spring stiffness of the coupled spring foundation model, the soil type based on the soil conditions and ground profile must be defined. The soil properties used in this work are those of glacial till. The result of the structural response obtained whilst considering the soil type both as cohesive and cohesionless soil type was compared in order to demonstrate the effect of the soil-structure interaction. The results of this thesis were achieved by making a good thesis plan, understanding offshore wind technology, understanding the soil-structure interaction, reviewing load models, reviewing foundation models and running finite element simulations.

The maximum ice load was estimated in this thesis using the Korzhavin equation for horizontal ice load on cylindrical structure. Wave load was estimated using Morrison's equation while the mean wind speed was estimated using the power law wind speed model. The loads calculated were validated using the results from the reference simulation. The maximum ice and wave loads calculated in this thesis were slightly different from those estimated in the reference simulation. This difference may have been due to the different load models used which incorporated slightly different parameters. For example the Määttänen-Blenkarn model used in the reference simulation took into account ice velocity which was not used in the Korzhavin equation. Extreme operating gust wind load, intermittent ice crushing and single frequency wave load was assumed during the finite element modelling. Wind and ice loads had dominant effect on the structural response in the case study described in this thesis. The maximum lateral displacement of the baseline turbine was at the tower top.

The result shows that load parameters such as ice thickness, wind speed and wave height have an effect on the loads (ice, wind and wave) and on the structural response of an offshore wind turbine. Therefore for ice, wind and wave load design, these parameters should be based on site specific conditions. The results of this thesis also suggest that the adhesion between the support structures of offshore wind turbines and the soil on which they are installed has an effect on their structural response. Therefore, it is crucial to consider the soil-structure interaction when modelling the structural response of offshore wind turbines. In addition, it is important to compute the right foundation model and soil properties in the absence of in-situ measurement as this can significantly affect the results of the simulation or analysis. In the absence of careful and detailed site measured data, the foundation models presented in this thesis in Table 5 may be used to approximate foundation stiffness theoretically.

The result of the natural frequency obtained using cohesive and cohesionless foundation models were quite close to the actual turbine natural frequency. Therefore, the foundation models used in this project to approximate the foundation stiffness in Tahkoluoto (Gulf of Bothnia) were found to provide good approximations in terms of natural frequency. However, the result of the turbine structural response obtained while using the coupled spring foundation is still questionable. The question arise from the inconsistency in the results which may be due to the coupled spring foundation model itself or its coupling term being modelled in Abaqus using connectors or the load models. Nevertheless, idealizing soil-monopile interaction using the coupled spring foundation model seemed promising.

Even though the coupled-spring foundation model gave a good approximation of the foundation stiffness in terms of natural frequency, there are still unanswered questions regarding the stiffness degradation effect with increased number of load cycles. In addition, the pile-soil represented by springs may be too simple representation of the soil-structure interaction mechanism. Furthermore, the simulation time (30 seconds) considered during this project may be too short to arrive at a conclusion as it was noticed that the signal or graph of the structural response changed when the simulation was run for longer period of time. Therefore, further studies and experiments should be carried out on the soil-structure interaction of more complex soils with larger number of load cycles and longer analysis duration.

8 Reference

[1]. J.F. Manwell, J.G. McGowan and A.L. Rogers (2009). *Wind Energy Explained: Theory, Design and Application*. 2nd ed. United Kingdom: John Wiley and Sons Ltd. p1-47.

[2]. Wind Energy Development Programmatic EIS. (2000). *Wind Energy Basics.* Available: http://windeis.anl.gov/guide/basics/. Last accessed 29th Dec 2015.

[3]. G. Moe, J. M. Niedzwecki, H. Long, R. Lubbad and S.-P. Breton. (2007). Fluid Structure Interaction and Moving Boundary Problem IV. *Technology for Offshore Wind Turbines*. 14 (4), p95-96.

[4]. Xiaojing Sun, Diangui Huang and Guoqing Wu. (2012). Energy. *The Current State of Offshore Wind Energy Technology Development.* 41 (1), p298-312.

[5]. John K. Kaldellis and D Zafirakis. (2011). Renewable Energy. *The Wind (R)evolution: A short review of a long history*. 36 (1), p1887-1901.

[6]. Paul A. Lynn. (2012). *Introduction. In: Paul A. Lynn Onshore and Offshore Wind Energy: An Introduction.* 1st ed. United Kingdom: John Wiley & Sons. P9-16.

[7]. Juchuan Dai, Denshun Liu, Li Wen and Xin Long. (2015). Renewable Energy. *Research on Power Coefficient of Wind Turbines Based on SCADA Data*. 86 (1), p206-215.

[8]. J.K. Kaldellis, D. Apostolou, M. Kapsali and E. Kondili. (2016). Renewable Energy. Environmental and Social Footprint of Offshore Wind Energy. *Comparison with Onshore Counterpart.* 92 (1), p543-556.

[9]. Fabian Vorpahl, Holger Schwarze, Tim Fischer, Marc Seidel and Jason Jonkman. (2012). Offshore wind turbine. *Environment, Loads, Simulation and Design*. 2 (1), 548-570.

[10]. J.H. Koh and E.Y.K. Ng. (2015). Renewable and Sustainable Energy Reviews. *Downwind Offshore Wind Turbines: Opportunities, Trends and Technical Challenges*. 54 (1), p797-808.

[11]. Dennis Y. C. Leung and Yuan Yang. (2012). Renewable and Sustainable Energy Reviews. *Wind Energy Development and Its Environmental Impact: A Review*. 16 (1), P1031-1039.

[12]. Erich Hau (2006). *Wind Turbines*. 2nd ed. Germany: Springer. P1-774.

[13]. Peter Tavner. (2012). Renewable Energy Series. *Offshore Wind Turbines Reliability, Availability and Maintenance.* 13 (1), P1-257.

[14]. Donald P. Coduto (2001). *Foundation Design: Principles and Practices*. 2nd ed. New Jersey: Prentice Hall. P1-841.

[15]. Andrew J. Bond, Bernd Schuppener, Giuseppe Scarpelli and Trevor L.L. Orr. (2013). JRC Scientific and Policy Reports. *Eurocode 7: Geotechnical Design Worked Examples*. 1 (1), P1-158.

[16]. B. W. Byrne and G. T. Houlsby. (2003). Philosophical Transactions of the Royal Society. *Foundations for Offshore Wind Turbines*. 361 (1), P2909-2930.

[17]. M. B. Zaaijer. (2006). Applied Ocean Research. *Foundation Modelling to Assess Dynamic Behaviour of Offshore Wind Turbines*. 28 (1), p45-57.

[18]. Swagata Bisoi and Sumanta Haldar. (2014). Soil Dynamics and Earthquake Engineering. *Dynamic Analysis of Offshore Wind Turbine in Clay Considering Soil-Monopile-Tower Interaction*. 63 (1), p19-35.

[19]. Jan Vander Temple (2006). Design of Support Structure for Offshore Wind Turbines. *Netherlands: DUWIND, Jan Vander Temple and Offshore Engineering*. p1-223.

[20]. Mehmet Yilmaz and ZhenZhong Wu. (2015). *CEE Coastal Engineering Class Project, University of Wisconsin-Madison.* Available: http://lakemichiganoffshoreturbine.weebly.com/method--analysis.html. Last accessed 20th Aug 2016.

[21]. Toyoaki Nogami, ASCE, Jun Otani, Kazuo Konagai and Hsiao-Lian Chen. (1992). Nonlinear Soil-Pile Interaction Model for Dynamic Lateral Motion. *Journal of Geotecnical Engineering*. 118 (1), p89-107.

[22]. American Petroleum Institute. (2003). Recommended Practice for Planning, Designing and Constructing Fixed Offshore Platforms-Working Stress Design. *API Recommended Practices 2A-WSD*. 21 (1), p1-242.

[23]. Sungmoon Jung, Sung-Ryul Kim, Atul Patil and Le Chi Hung. (2015). Effect of Monopile Foundation Modeling on the Structural Response of a 5-MW Offshore Wind Turbine Tower. *Ocean Engineering*. 109 (1), p479-488.

[24]. Alice Rosmi, Sandrine Aubrun, Jakob Mann and Michael Muskulus (2015). EWEA 2015 Scientific Proceedings. *Brussels: European Wind Energy Association (EWEA)*. p8-100.

[25]. Laszlo Arani, S. Barttasharya, John H. G. Macdonald and S. John Hogan. (2016). Soil Dynamics and Earthquake Engineering. *Closed Form Solution of Eigen Frequency of Monopile Supported Offshore Wind Turbines in Deeper Waters Incorporating Stiffness of Substructure and SSI*. 83 (2), p18-32.

[26]. Peter K. Stansby, Louise C. Devaney and Tim J. Stallard. (2013). Breaking Wave Loads on Monopiles for Offshore Wind turbines and Estimation of Extreme Overturning Moment. *IET Renewable Power Generation*. 7 (5), p514-520.

[27]. J. Van Der Temple, N. F. B. Diepeveen, W. E.DE Vries and D. Cerda Salzmann. (2011). Offshore Environmental Loads and Wind Turbine Design. *Impact of Wind, Wave, Currents and Ice*. 15 (1), p463-478.

[28]. M.A. Benitz, M.A. Lackner and D.P. Schmidt. (2015). Hydrodynamics of Offshore Structures with Specific Focus on Wind Energy Applicaions. *Renewable and Sustainable Energy Reviews*. 44 (1), p692-716.

[29]. International Standard. (2009). Part 3: Design Requirement for Offshore Wind Turbines. In: *IEC Wind Turbines*. Switzerland: IEC61400-3. p35-125.

[30]. Wei Shi, Xiang Tan, Zhen Gao and Torgeir Moan. (2015). Numerical Study of Ice-induced Loads and Responses of a Monopile-type Offshore Wind Turbine in Parked and Operating Conditions. *Cold Regions Science and Technology*. 123 (1), p121-139.

[31]. Wojciech Popko, Jaakko Heinonen, Sebastian Hetmanczyk and Fabian Vorpahl. (2015). State-of-the-art Comparison of Standards in Terms of Dominant Sea Ice Loads for Offshore Wind Turbines Support Structures in Baltic Sea. *Offshore Wind Turbines*. 1 (1), p1-8.

[32]. ISO. (2010). Petroleum and natural gas industry - Arctic Offshore Structures. In: ISO *International Standard*. Geneva: ISO. p10-262.

[33]. S. Rodrigues, C. Restrepo, E. Kontos, R. Teixeira into and P. Bauer. (2015). Trends of Offshore wind projects. *Renewable and Sustainable Energy Reviews*. 49 (1), p1114-1135.

[34]. Paul Breeze. (2015). Offshore Wind. In: Paul Breeze *Wind Power Generation*. UK: Academic Press. p75-84.

[35]. Bureau of Ocean Energy Management. (2016). *Offshore wind energy.* Available: http://www.boem.gov/Offshore-Wind-Energy/. Last accessed 16th Aug 2016.

[36]. Wikipedia. (2016). Gulf of Bothnia. Available: https://en.wikipedia.org/wiki/Gulf_of_Bothnia. Last accessed 20th Aug 2016.

[37]. National Geospatial-Intelligence Agency. (2014). Gulf of Finland and Gulf of Bothnia. Sailing Direction (ENROUTE). 195 (13), P1-199.

[38]. Wikipedia. (2013). *Tahkoluoto.* Available: https://fi.wikipedia.org/wiki/Tahkoluoto. Last accessed 20th Aug 2016.

[39]. Perez-Collazo, D. Greaves and G. Iglesias. (2014). A review of combined wave and offshore energy. *Renewable and Sustainable Energy Reviews*. 42 (1), p141-153.

[40]. Rasi-Koskinen Hanna. (2014). Vaakasuuntaiset Alustaluvut Paaluperusteisissa Silloissa. *Teknillinen Tiedenkunta*. 1 (1), p10-127.

[41]. Pauli Velhonoja and Pentti Salo. (2001). Tieden Pohjarakenteiden Suunnittelperusteet. *Tiehallinto*. 1 (1), p9-116.

[42]. RAMBOLL. (2014). Tahkoluodon Merituulipuiston Osayleiskaava. *Kaavaehdotuksen Selostus*. 1 (1), P7.

[43]. Simo Rissanen and Jaakko Heinonen. (2016). Simulations of Drifting Sea Ice Loads on Offshore Wind Turbine. *Winterwind 2016*. 1 (1), p1-19.

[44]. IEC. (2005). Wind Turbines - Part 1: Design Requirements. In: IEC *International Standard*. 3rd ed. Geneva: IEC61400-1. p8-79.

[45]. Joseph E. Bowles (1988). *Foundation Analysis And Design*. 4th ed. United State of America: McGraw-Hill Inc. p99-100.

[46]. Mehmet Bilgili, Abdulkadir Yasar and Erdogan Simsek. (2010). Offshore Wind power development in Europe and its comparison with onshore counterpart. *Renewable and Sustainable Energy Reviews*. 15 (1), p905-915.

[47]. Shrabony Adhikary, Yogendra Singh and D.K. Paul. (2008). Modelling of Soil-Foundation-Structure-System. *Department of Eathquake Engineering,IIT Roorkee*. 1 (1), p1-13.

[48]. M. Bayat, L.V. Andersen and L.B. Ibsen. (2016). p-y-y curves for dynamic analysis of offshore ind turbine monopile foundations. *Soil Dynamics and Earthquake Engineering*. 90 (1), p38-51.

[49]. J. Jonkman, S. Butterfield, W. Musial and G. Scott. (2009). Definition of a 5-MW Reference Wind Turbine for Offshore System Development. *National Renewable Energy Laboratory*. 1 (1), p1-2.

[50]. Hyötytuuli. (2016). *Offshore Wind Power.* Available: http://hyotytuuli.fi/en/offshore-wind-power/. Last accessed 11th Oct 2015.

[51]. Sarvesh Chandra. (2014). Indian Institute of Technology Kampur. *Modelling of Soil Behaviour*. 1 (1), p4-6.

[52]. Jaakko Heinonen and Simo Rissanen. (2015). FAST Simulations of Drifting Sea Ice Loads on Offshore Wind Turbine Support Structures. *EWEA*. 1 (1), p1.

Appendix

Appendix 1: Wind Load on Wind Turbine Blades

The blades are subjected to lift (F_L) and drag (F_D) forces due to relative wind velocity (Vrel) as shown in Figure 65. The aerodynamic load per blade element in the x-direction as described in Figure 65 is given by Equation 26. [19]

$$F_x = F_L \cos \emptyset + F_D \sin \emptyset = \frac{1}{2} C_L(\alpha) \rho_{air} V_{rel}^2 c_a \Delta r \cos \emptyset + \frac{1}{2} C_D(\alpha) \rho_{air} V_{rel}^2 c_a \Delta r \sin \emptyset \quad (26)$$

Where F_L is the aerodynamic lift in N; F_D is the aerodynamic drag in N; $C_L(\alpha)$ is the aerodynamic lift coefficient; $C_D(\alpha)$ is the aerodynamic drag coefficient ρ_{air} is the mass density of air in Kg/m^3; C_a is the airfoil chord length; Δr is the radial length of the blade element; α is the angle of attack in degree; $\emptyset$ is the angle of inflow in degree; θ is the pitch angle in degree; V_{rel} is the relative wind speed at a blade section in m/s Equation (27).

$$V_{rel} = \sqrt{V_{disk}^2 + V_{rot}^2} \quad (27a)$$

$$V_{disk} = V_0(1 - a) \quad (27b)$$

$$V_{rot} = \Omega . r \quad (26c)$$

Where V_{disk} is the wind velocity at the airfoil in m/s; V_{rot} is the linear rotation speed at a blade section in m/s; Ω is the angular rotation speed in rad/s; r is the distance of the blade element to the axis of rotation in m.

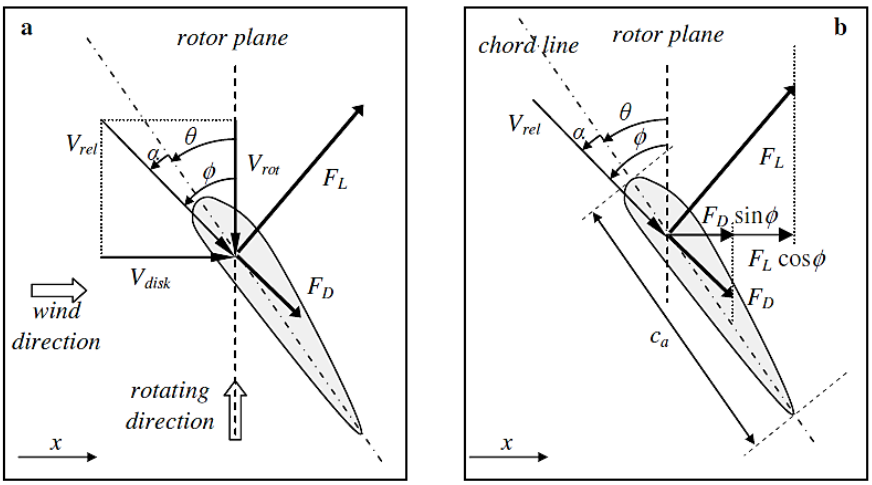

Figure 65: a) Lift and drag load on the blade element b) Resulting loads in the x-direction [19]

Appendix 2: Sensitivity Test of Logarithmic and Power Law Wind Speed Models

Both logarithmic and power law wind speed models are commonly used for offshore wind turbines. It is therefore very important to understand how both models behave, where they meet and how they significantly deviate from each other in order to select that which works best for a given case study.

Case 1: Rough Sea

The reference speed selected for this case was selected based on the fact that normally cut-in speed for wind turbine is 4 m/s and cut-out speed is 25m/s. In addition, the power output is usually maximum at a wind speed of 15 m/s and remain constant till a value (24m/s) closed to the cut-out speed as early illustrated in Figure 7. Equation (15a) and (15b) are plotted in Figure 66 using the following parameters: The surface roughness $z_0 = 0.0005$ m; The power law coefficient $\alpha_{shear} = 0.12$; The reference speed $V_{w,r} = 15$ m/s; The reference height $z_r =$ hub height = 80 m; The turbine hub height z = 0 - 80 m.

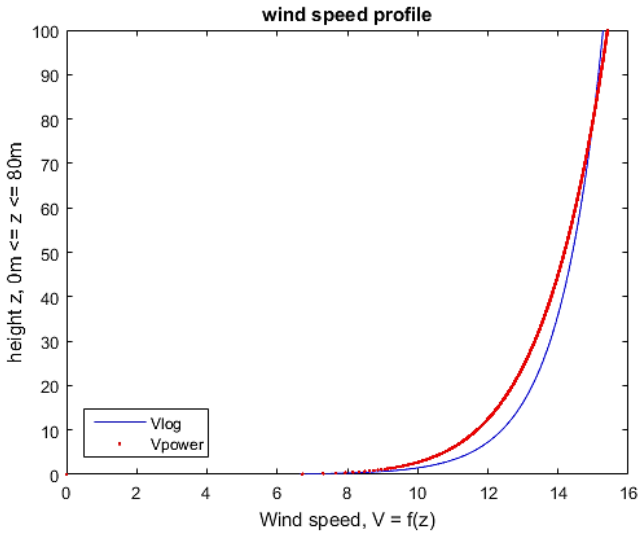

Figure 66: Comparison between the logarithmic and power of law wind models; Vlog is the graph of the logarithmic profile; Vpower is the graph of the power law profile

As it can be observed from the figure above, both load models in this case study are slightly different at lower turbine heights and become closer to each other with higher altitude. Both models are equal at the reference height which in this case is equal to the hub's height. *Vlog* is the graph of the logarithmic profile while *Vpower* represents the graph of the power law model.

Case 2: Rough Sea with Changed Reference Height

It is important to choose the reference height to be as close to the turbine tower height as possible. To understand how important it is to choose the correct reference height and why the turbine hub height is generally chosen as reference height, the same study carried out in case study 1 was evaluated in case study 2 with a choice of reference height different and lower than the turbine hub height. As it can be observed from the figure below, both models converge up to the reference point where they meet and after which they diverge significantly

from each other with increase height. The parameters used are: $Z_0 = 0.0005$ m, $\alpha_{shear} = 0.12$, $V_{w,r} = 15$ m/s, $z_r = 50$ m, Z = 0 - 200 m and turbine hub height is 200 m.

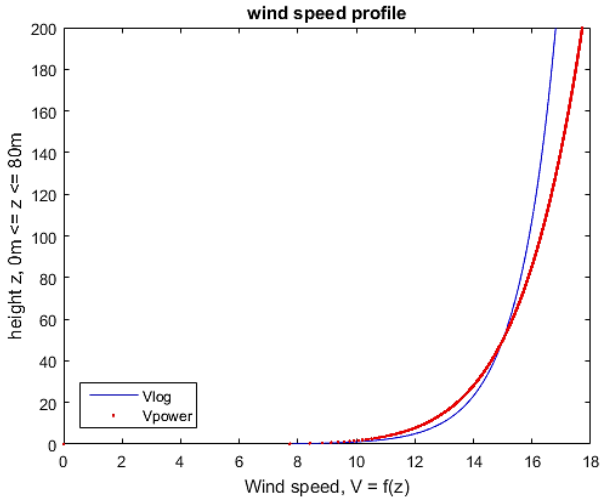

Figure 67: Comparison between the logarithmic and power law wind models; Vlog is the graph of the logarithmic profile; Vpower is the graph of the power law profile

If the reference point is chosen too high as compared to the turbine tower's height, both load models are different from each other throughout the turbine's height as shown in the figure below. The parameters used are: $z_0 = 0.0005$ m, $\alpha_{shear} = 0.12$, $V_{w,r} = 15$ m/s, $z_r = 200$ m, z = 0-100 m and turbine hub height is 100 m.

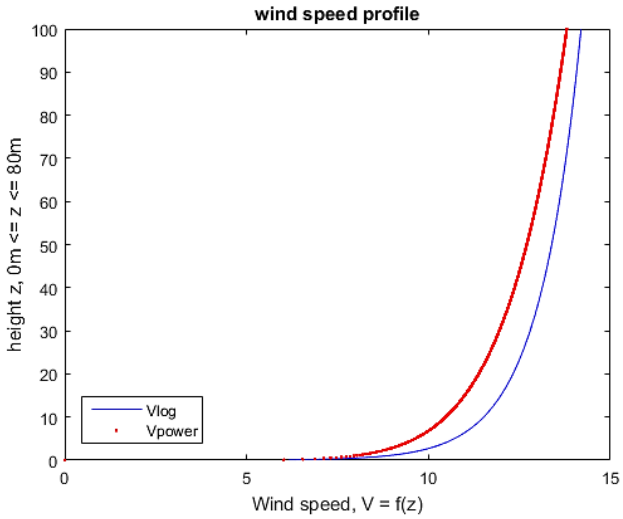

Figure 68: Comparison between the logarithmic and power law wind models; Vlog is the graph of the logarithmic profile; Vpower is the graph of the power law profile

Case 3: Calm Open Sea

The roughness length and the power law factor of calm open sea are different from those of rough sea (Table 6). The parameters used for calm open sea case are: $z_0 = 0.0002$ m, $\alpha_{shear} = 0.12$, $V_{w,r} = 15$m/s, $z_r = 150$ m, z = 0 - 200 m.

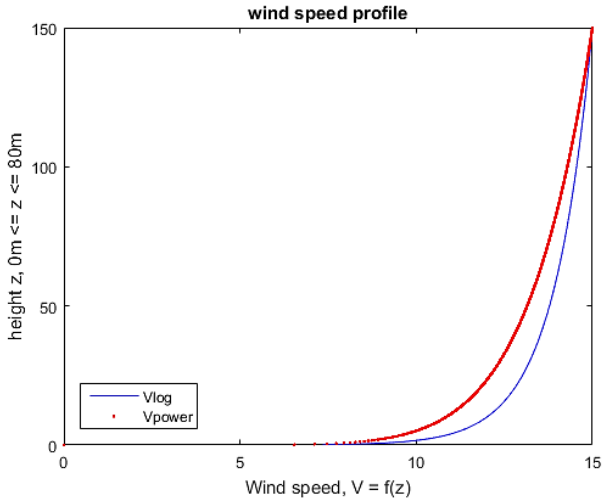

Figure 69: Comparison between the logarithmic and power law wind models

Case 4: Suburbs, Wooded Country Side

In this case, the roughness length is quite high and has the same value as the power law factor. The parameters used in this case are: $z_0 = 0.3$ m, $\alpha_{shear} = 0.3$, $V_{w,r} = 15$ m/s, $z_r = 150$ m, z = 0-150 m.

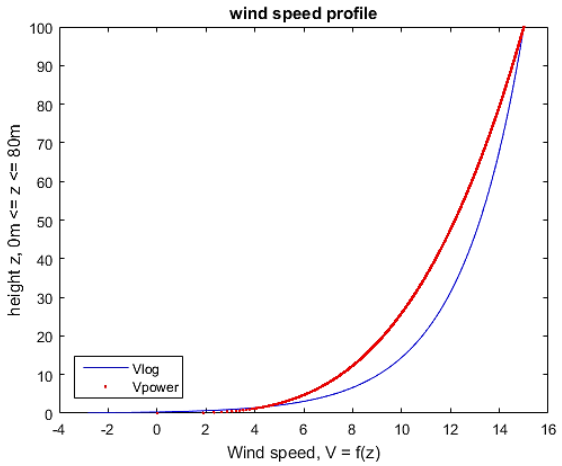

Figure 70: Comparison between the logarithmic and power law wind models; Vlog is the graph of the logarithmic profile; Vpower is the graph of the power law profile

In conclusion, it can be seen from these different case studies that even if the roughness length (z_0) and the power law factor (α_{shear}) are changed, both wind speed model will always converge towards each other up till the reference point. Therefore, it can be said that any of these models will provide good result throughout the turbine's tower if the turbine's hub height is chosen as the reference height. However, if the reference height is chosen too far away (too low or too high) from the turbine's hub height, the result from both models throughout the turbines height may be significantly different.

Appendix 3: Structural Response using Cohesionless Foundation Model

The lateral structural response under dynamic ice, wave and wind loads, taking into account the smallest cohesionless soil stiffness calculated in section 5.3.2, is presented below.

1. Wave Loading

The result of the lateral response of the turbine under wave load whilst considering cohesionless soil model is presented in Figure 71, 72 and 73. In Figure 71, the lateral response of all the nodes at 31.5 seconds is shown. The red colour (at the bottom) represents the support structure and the blue represents the tower top. The maximum lateral displacement is at the tower top as can be observed in Figure 71. The lateral displacement at the mudline is shown in Figure 72. The maximum displacement of monopile at the seabed under wave loading is about 1 mm. The maximum lateral displacement of the tower top is about 29 mm as shown in Figure 73.

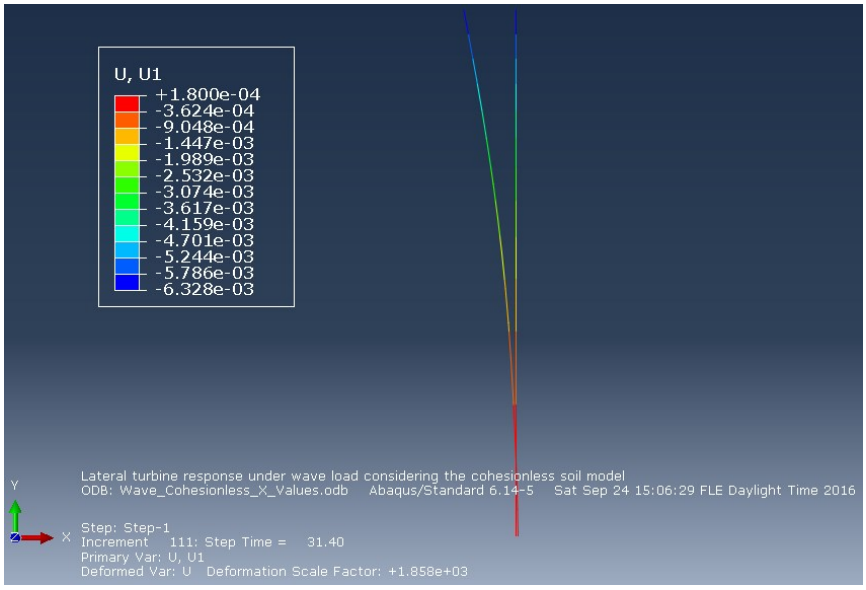

Figure 71: Structural response under wave loading; U1 is the lateral displacement of the baseline offshore wind turbine

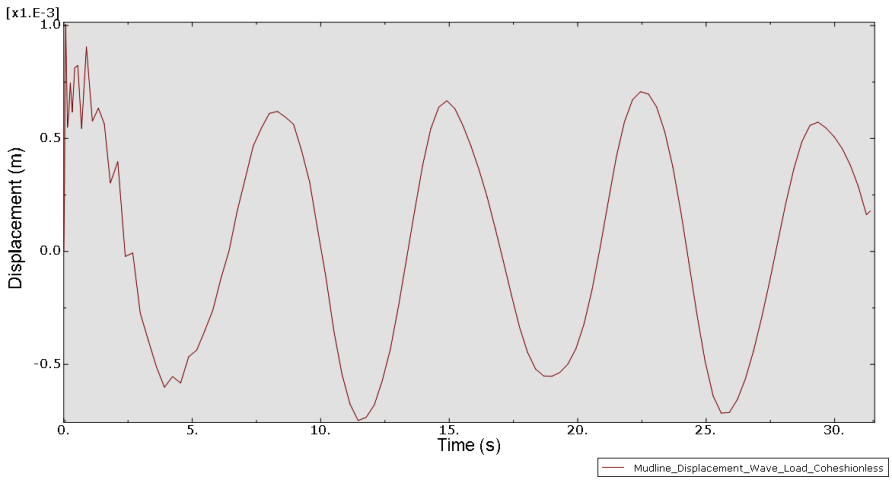

Figure 72: Lateral response at Mudline of the baseline offshore wind turbine under wave loading

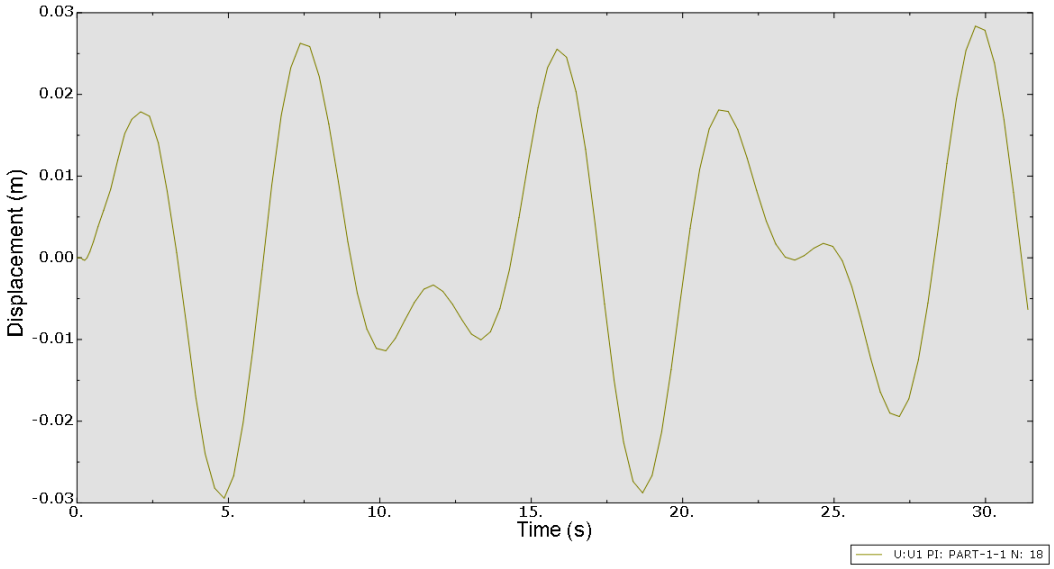

Figure 73: Lateral response at the tower top of the baseline offshore wind turbine under wave loading

2. Ice Loading

The result of the lateral response of the turbine under dynamic ice load whilst considering the cohesionless soil model is presented in Figure 74, 75 and 76. The lateral displacement of all the nodes at 30 seconds is shown in Figure 74. The blue colour (at the bottom) represents the support structure and the red represents the tower top. The lateral displacement at the mudline is shown in Figure 75. The maximum displacement of the substructure at the seabed under ice loading is about 13 mm. The maximum lateral turbine displacement the tower top is about 247 mm as shown in Figure 76. The maximum monopile displacement is about 65 mm.

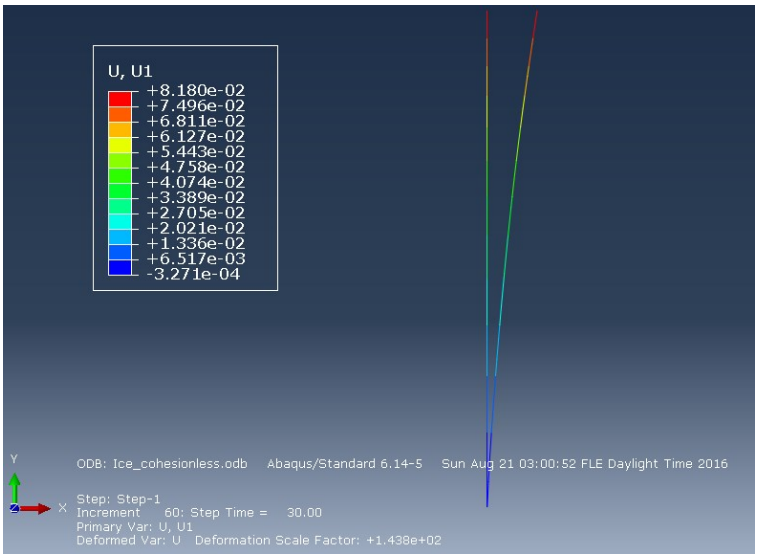

Figure 74: Structural response under dynamic ice loading

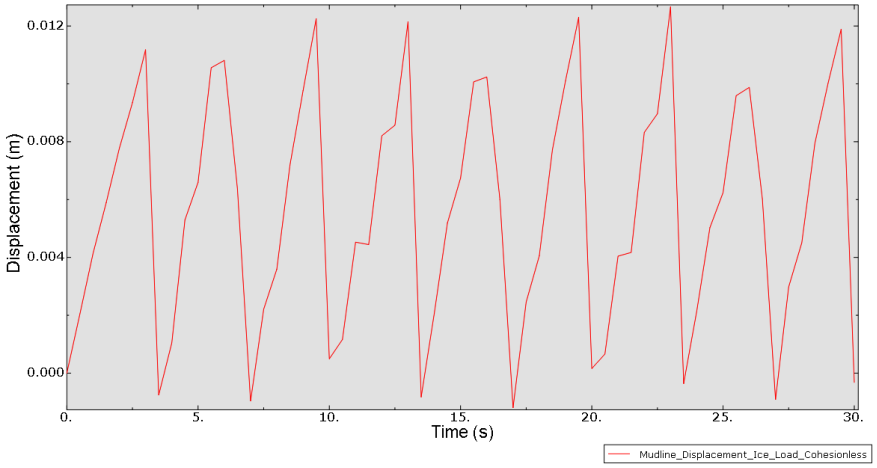

Figure 75: Lateral response of monopile at seabed of the baseline offshore wind turbine under dynamic ice loading

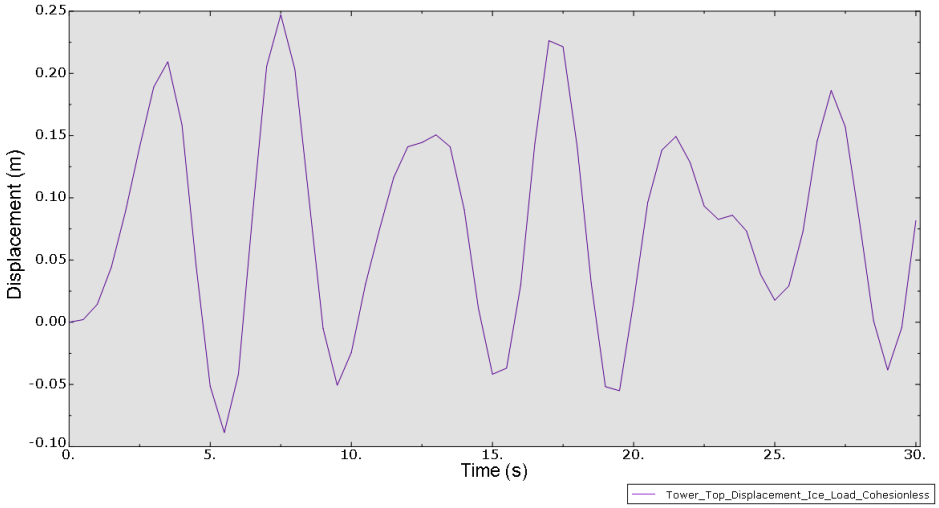

Figure 76: Lateral response of the baseline offshore wind turbine at the tower top under dynamic ice loading

3. Wind Loading

The result of the lateral response of the turbine under extreme operating gust wind load whilst considering the cohesionless soil model is presented in Figure 77, 78 and 79. The lateral displacement of all the nodes at 30 seconds is shown in Figure 77. The blue colour (at the bottom) represents the support structure and the red represents the tower top. The lateral displacement at the mudline is shown in Figure 78. The maximum displacement of the substructure at the seabed under extreme operating gust wind load is about 20 mm. The maximum lateral turbine displacement at the tower top is about 2580 mm as shown in Figure 79. The maximum displacement of the support structure is about 379 mm.

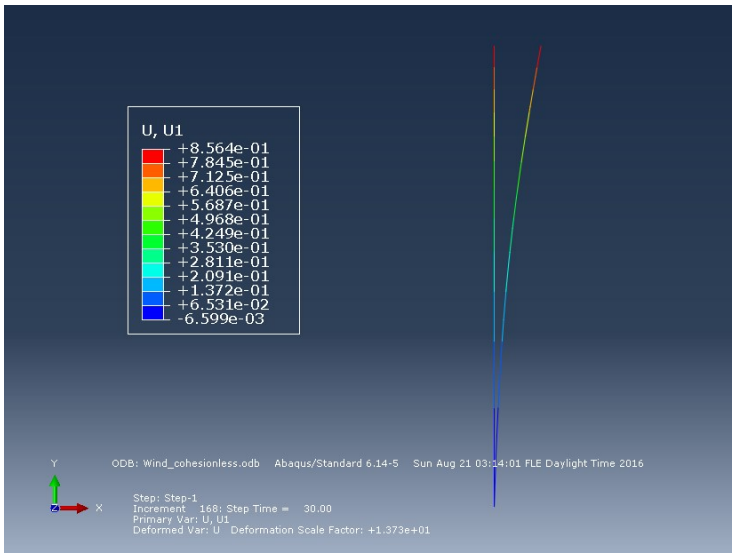

Figure 77: Structural response under extreme operating gust wind load; U1 is the lateral displacement of the baseline offshore wind turbine

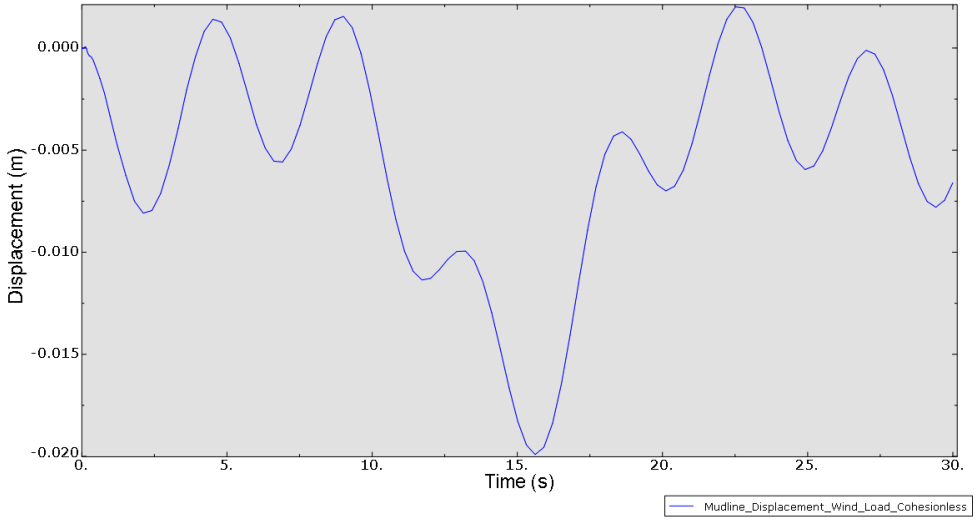

Figure 78: Lateral response of the baseline offshore wind turbine at seabed under extreme operating gust wind load

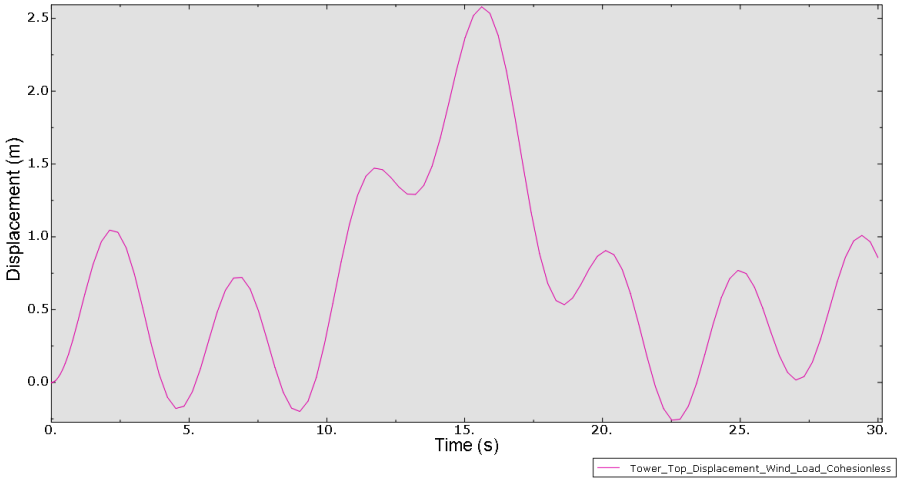

Figure 79: Lateral response at the tower top of the baseline offshore wind turbine under extreme operating gust wind load

4. Start-up: Design Load Case 32

Figure 80 shows the nodal displacements of the 5-MW baseline wind turbine under combine extreme gust wind load and wave load whilst considering the cohesionless soil model. In the legend in Figure 56, U:U1 refers to the displacement in the x-direction (lateral displacement), Part-1-1 refers to the turbine and N refers to the nodes. N:1-1 or node 1 is refers to the nodal point at the seabed. N:1-1 to N:8-1 are nodes in the support structure while N:8-1 to N:18-1 are nodes in the tower. Node 18 is used for the tower top. The maximum turbine lateral response at the seabed for a period of about 30s under combine extreme gust wind load and wave load is about 29 mm. The maximum lateral displacement at the tower top is about 3844 mm while the maximum displacement at the support structure is about 568 mm.

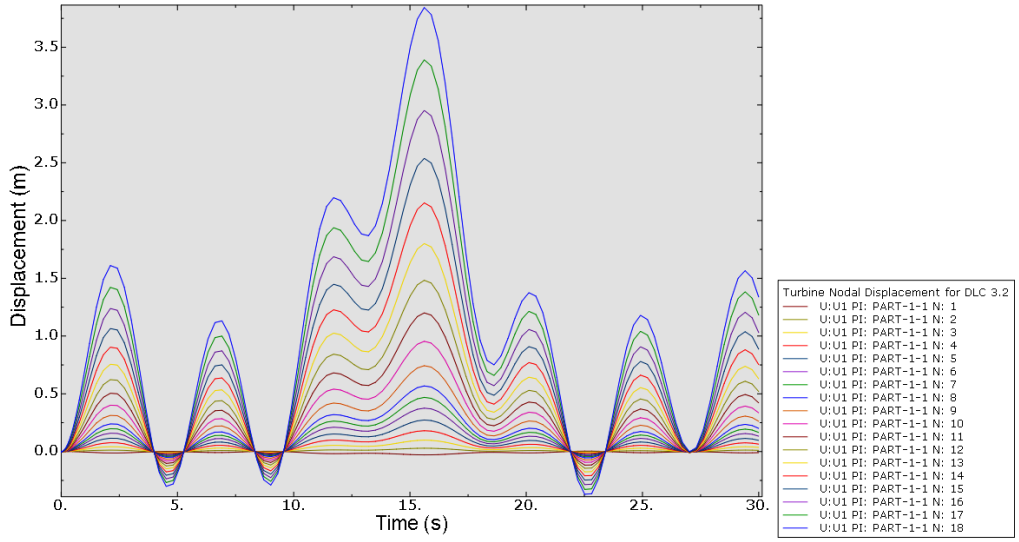

Figure 80: Nodal lateral displacement for design load case 32; U1 is the lateral displacement, part-1-1 is part number of the model in Abaqus and N:1 to18 represent the node numbers

5. Power Production: Design Load Case E3

The structural response under combine ice and wind load according to the design load case E3 by IEC61400-3 is presented here. The soil-structure interaction is taking into account in this analysis by considering the cohesionless soil model.

When the loads are co-directional, the maximum turbine lateral response at the seabed for a period of 30 seconds under combine dynamic ice load and normal turbulence wind load is about 30 mm. The maximum lateral displacement at the turbine top is about 700 mm while the maximum displacement at the support structure is about 164 mm. Figure 81 shows the lateral nodal displacement of the 5-MW baseline wind turbine under combine dynamic ice load and normal turbulence wind load with the loads applied to the same direction. The definition of the node numbers in Figure 81 is the same as already explained in the design load case 32.

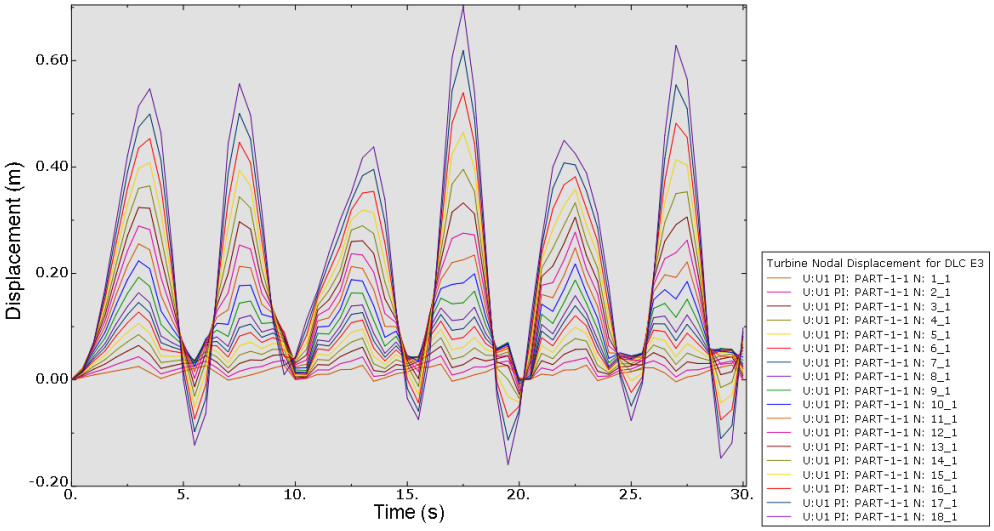

Figure 81: Nodal lateral displacement for design load case E3 when the loads are co-directional; U1 is the lateral displacement, part-1-1 is part number of the model in Abaqus and N:1 to18 represent the node numbers

When the loads are applied to opposite-direction, the maximum turbine lateral response at the seabed for a period of 30 seconds under combine dynamic ice load and normal turbulence wind load is about 31 mm. The maximum lateral displacement at the turbine top is about 610 mm while the maximum displacement at the support structure is about 147 mm. Figure 82 shows the lateral nodal displacements of the turbine under combine dynamic ice load and normal turbulence wind load when the loads are applied to opposite directions.

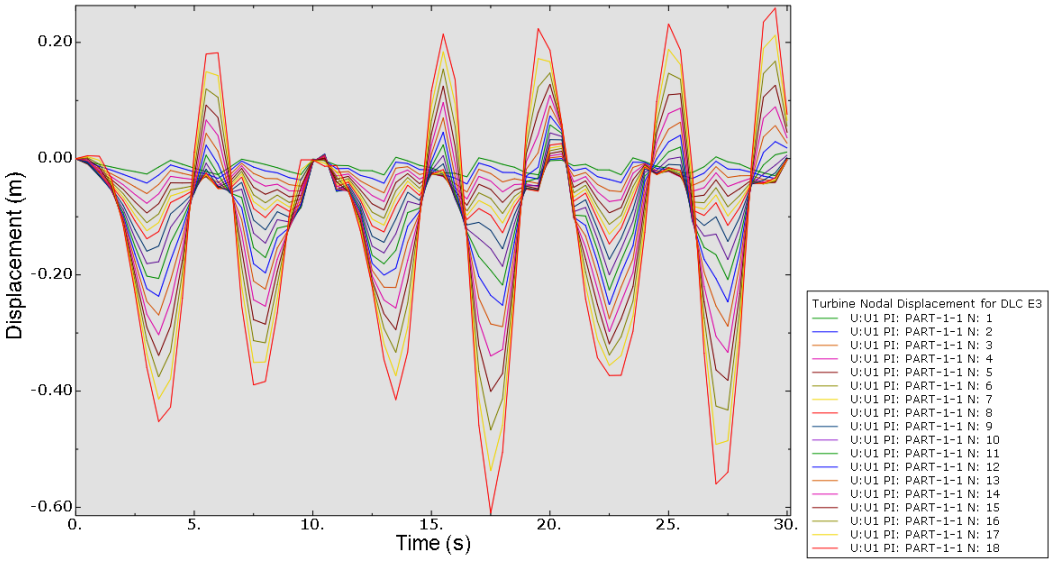

Figure 82: Nodal lateral displacement for design load case E3 when the loads are in opposite direction; U1 is the lateral displacement, part-1-1 is part number of the model in Abaqus and N:1 to18 represent the node numbers

Appendix 4: Sensitivity of Cohesive and Cohesionless Soil Models

To evaluate how sensitive the selected foundation models are with respect to the soil parameters, a sensitivity test will be run on the formulae for the modulus of subgrade reaction for cohesive and cohesionless soils. The modulus of subgrade reaction is the only parameter in the models (used for finding the foundation stiffness) taking into account the soil properties.

A. Cohesive Soil Model

Equation 6 is used for theoretically computing the modulus of subgrade reaction of cohesive soils. There are two main soil parameters in this equation: the elastic modulus and Poisson's ration of the soil. The sensitivity of the model to both soil parameters will be evaluated.

1. Soil's Modulus of Subgrade Reaction (k_h) as a Function of E_s

The relationship between the modulus of subgrade reaction and the modulus of elasticity of the soil is evaluated. They both have a linearly increasing relationship. As can be seen from the figure below, an increase in the elastic modulus significantly increases the subgrade reaction which will in turn affect the soil stiffness, thus the equation below is quite sensitive to the soil elastic modulus. In other words, it is imperative to choose the right soil elastic modulus parameter to find the optimum soil stiffness numerically.

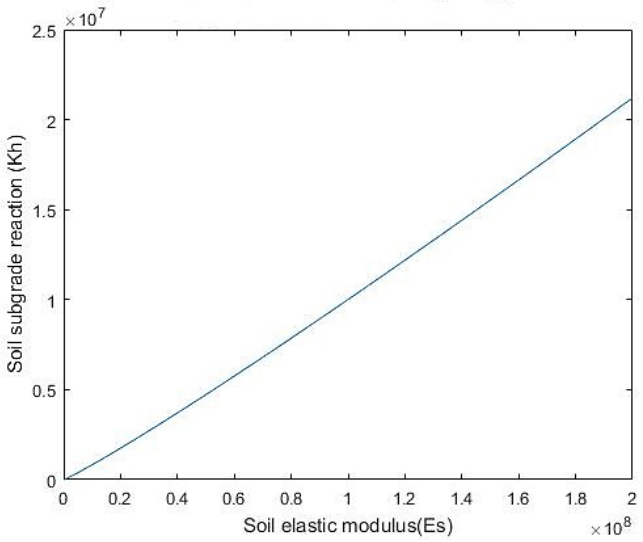

Figure 83: The subgrade reaction of the soil as a function of the elastic modulus of the soil

2. Soil's Modulus of Subgrade Reaction as a Function of v_s

The figure below illustrates the relationship between the subgrade reaction and the Poisson ratio of the soil. It can be seen that they both have an exponential relationship. The change in Poisson ratio doesn't drastically affect the soil subgrade reaction therefore, the cohesive soil model is not very sensitive to the Poisson ratio of the soil.

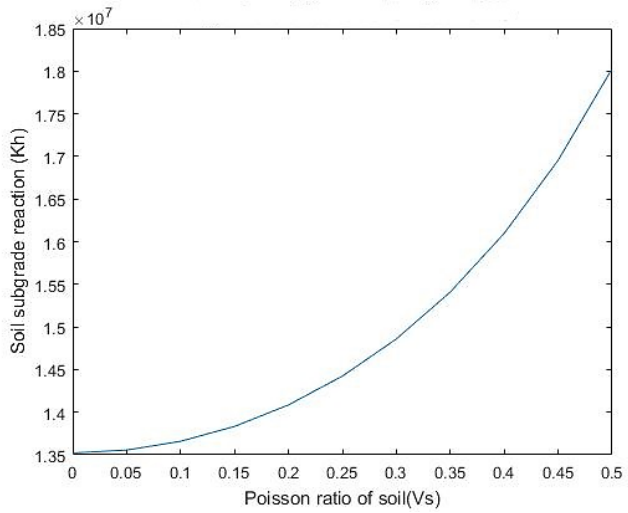

Figure 84: The modulus of subgrade reaction of the soil as a function of the Poisson ration of the soil

B. Cohesionless Soil Model

Equation 7 is used for numerically computing the modulus of subgrade reaction of cohesionless soils. There is only one soil parameter in this equation which is the coefficient of subgrade reaction (η_h). Since there is only one soil parameter in the equation for finding the subgrade reaction of cohesionless soil and this parameter significantly affect the subgrade reaction, it is important to choose the right value for the soil coefficient of subgrade reaction (η_h).

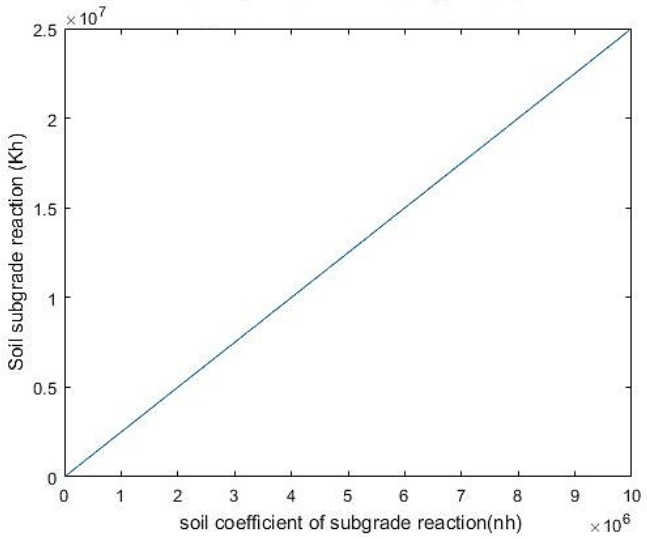

Figure 85: Modulus of subgrade reaction of the soil as a function of the coefficient of subgrade reaction